GDAŃSK UNIVERSITY OF TECHNOLOGY

The author of the doctoral dissertation: Paweł Kroplewski
Scientific discipline: Automation, Electronics, Electrical Engineering and Space Technologies

DOCTORAL DISSERTATION

Title of doctoral dissertation: Control structures of Doubly-Fed Induction Generator connected to Current Source Converter

Title of doctoral dissertation (in Polish): Struktury sterowania maszyną dwustronnie zasilaną pracującą jako generator podłączoną do przekształtnika prądu

Supervisor *signature*	Second supervisor *signature*
prof. Marcin Morawiec	<Title, degree, first name and surname>
Auxiliary supervisor *signature*	Cosupervisor *signature*
<Title, degree, first name and surname>	<Title, degree, first name and surname>

Gdańsk, year 2024

POLITECHNIKA GDAŃSKA

STATEMENT

The author of the doctoral dissertation: Paweł Kroplewski

I, the undersigned, declare that I am aware that in accordance with the provisions of Art. 27 (1) and (2) of the Act of 4th February 1994 on Copyright and Related Rights (Journal of Laws of 2021, item 1062), the university may use my doctoral dissertation entitled:
Control structures of Doubly-Fed Induction Generator connected to Current Source Converter
for scientific or didactic purposes.[1]

Gdańsk,..... .....

signature of the PhD student

Aware of criminal liability for violations of the Act of 4th February 1994 on Copyright and Related Rights and disciplinary actions set out in the Law on Higher Education and Science(Journal of Laws 2021, item 478), as well as civil liability, I declare, that the submitted doctoral dissertation is my own work.

I declare, that the submitted doctoral dissertation is my own work performed under and in cooperation with the supervision of prof. Marcin Morawiec.

This submitted doctoral dissertation has never before been the basis of an official procedure associated with the awarding of a PhD degree.

All the information contained in the above thesis which is derived from written and electronic sources is documented in a list of relevant literature in accordance with Art. 34 of the Copyright and Related Rights Act.

I confirm that this doctoral dissertation is identical to the attached electronic version.

Gdańsk,..... .....

signature of the PhD student

I, the undersigned, agree to include an electronic version of the above doctoral dissertation in the open, institutional, digital repository of Gdańsk University of Technology.

Gdańsk,..... .....

signature of the PhD student

[1] Art 27. 1. Educational institutions and entities referred to in art. 7 sec. 1 points 1, 2 and 4–8 of the Act of 20 July 2018 – Law on Higher Education and Science, may use the disseminated works in the original and in translation for the purposes of illustrating the content provided for didactic purposes or in order to conduct research activities, and to reproduce for this purpose disseminated minor works or fragments of larger works.

2. If the works are made available to the public in such a way that everyone can have access to them at the place and time selected by them, as referred to in para. 1, is allowed only for a limited group of people learning, teaching or conducting research, identified by the entities listed in paragraph 1.

GDAŃSK UNIVERSITY OF TECHNOLOGY

DESCRIPTION OF DOCTORAL DISSERTATION

The Author of the doctoral dissertation: Paweł Kroplewski

Title of doctoral dissertation: Control structures of Doubly-Fed Induction Generator connected to Current Source Converter

Title of doctoral dissertation in Polish: Struktury sterowania maszyną dwustronnie zasilaną pracującą jako generator podłączoną do przekształtnika prądu

Language of doctoral dissertation: English

Supervisor: Marcin Morawiec

Date of doctoral defense: <day, month, year>

Keywords of doctoral dissertation in Polish: struktury sterowania, falownik prądu, przekształtnik prądu, maszyna dwustronnie zasilana

Keywords of doctoral dissertation in English: control systems, current source inverter, current source converter, doubly-fed induction generator

Summary of doctoral dissertation in Polish: Sterowanie maszyną dwustronnie zasilaną pracującą jako generator można osiągnąć za pomocą różnych metod. Obecnie wiele publikacji pokazuje zastosowanie przekształtnika napięcia w połączeniu z maszyną dwustronnie zasilaną. Ostatnio opublikowane artykuły rzadko dotyczą charakterystyk operacyjnych i aspektów technicznych układów z maszyną dwustronnie zasilaną połączoną z przekształtnikiem prądu. Rozprawa doktorska przedstawia nowe metody sterowania maszyną dwustronnie zasilaną połączoną z przekształtnikiem prądu. Zaproponowane zostały cztery nieliniowe, multiskalarne metody sterowania przepływem mocy generatora indukcyjnego. Głównym wkładem są nowe sprzężenia zwrotne pozwalające na linearyzację nieliniowego obiektu i odsprzężenia w torach regulacji mocy czynnej i biernej. Ponadto nowe algorytmy sterowania pozwalają na niezależną regulację mocy czynnej i biernej stojana. Przedstawiono cały cykl badawczy, który obejmuje testy symulacyjne oraz badania eksperymentalne zaimplementowanych metod sterowania. Przeanalizowane zostały ich odpowiedzi na zmiany mocy czynnej i biernej, przejście przez prędkość synchroniczną jak również zapady napięcia sieciowego.

Summary of doctoral dissertation in English: The control of Doubly-Fed Induction Generator can be achieved through various techniques. At present, many works published in the literature show the application of Voltage Source Converter in conjunction with Doubly-Fed Induction Generator. Recently published articles rarely involve the operational characteristics and technical aspects of the Doubly-Fed Induction Generator - Current Source Converter systems. The dissertation presents a new development of control methods for Doubly-Fed Induction Generator connected to Current Source Converter. Four novel non-linear multiscalar control methods for power flow for Doubly-Fed Induction Generator connected to Current Source Converter are proposed by the author. The main contributions are new feedback that allow linearization of the nonlinear object and decoupling in active and reactive power control paths. Furthermore, new control algorithms allow to independently regulate the stator active and reactive powers. The entire development cycle is presented, which includes simulations as well as experimental tests of the implemented control methods for the complete generator system. Their responses to changes in active and reactive power, transition through synchronous speed as well as grid voltage dips were analyzed.

Acknowledgments

Firstly, I would like to express my deepest appreciation to my Ph.D. supervisor Prof. Marcin Morawiec for his involvement, patience and motivation during my doctoral studies. His advice and knowledge helped me a lot during my research and writing of this thesis.

Besides my supervisor, I like to express my gratitude to Prof. Jarosław Guziński, Assoc. Prof. Arkadiusz Lewicki, D.Sc., Krzysztof Blecharz, Ph.D, Filip Wilczyński, Ph.D, Charles Odeh, Ph.D, Mariusz Rutkowski, M.Sc. and Mr. Robert Dobieglewski for the discussions and excellent teamwork during my Ph.D. study years.

Last, but definitely not least, I am deeply grateful to my grandmother Urszula, mother Mariola and sister Magdalena, for their support.

List of acronyms

AC	Alternating Current
ADC	Analog-to-Digital Converter
CSC	Current Source Converter
CSI	Current Source Inverter
DFIG	Doubly-Fed Induction Generator
DFIM	Doubly-Fed Induction Machine
DSP	Digital Signal Processor
DTC	Direct Torque Control
FFT	Fast Fourier Transform
FLC	Fuzzy Logic Control
FOC	Field Oriented Control
FPGA	Field Programmable Gate Array
GaN	Gallium Nitride
IG	Induction Generator
IGBT	Insulated Gate Bipolar Transistor
PD	Proportional Derivative
PI	Proportional Integral
PID	Proportional Integral Derivative
PLL	Phase Locked Loop
PMSG	Permanent Magnet Synchronous Generator
PWM	Pulse Width Modulation
RB-IGBT	Reverse-Blocking Insulated Gate Bipolar Transistor
SCR	Silicon Controlled Rectifier
SEIG	Self-Excited Induction Generator
SG	Synchronous Generator

SiC	Silicon Carbide
SVPWM	Space Vector Pulse Width Modulation
VOC	Vector Oriented Control
VSC	Voltage Source Converter
WECS	Wind Energy Conversion System

List of symbols

J	moment of inertia
L_m	mutual inductance
L_s, L_r	stator, rotor inductance
R_s, R_r	stator, rotor resistance
Ψ_{rd}, Ψ_{rq}	d, q axis components of rotor flux
Ψ_{sd}, Ψ_{sq}	d, q axis components of stator flux
Ψ_{sx}, Ψ_{sy}	x, y axis components of stator flux
ω_a	angular speed of the coordinate system
ω_r	rotor angular speed
$\vec{\Psi_s}$, $\vec{\Psi_r}$	stator, rotor flux vectors
$\vec{i_s}$, $\vec{i_r}$	stator, rotor current vectors
$\vec{u_s}$, $\vec{u_r}$	stator, rotor voltage vectors
i_{rd}, i_{rq}	d, q axis components of rotor current
i_{rx}, i_{ry}	x, y axis components of rotor current
i_{sd}, i_{sq}	d, q axis components of stator current
i_{sx}, i_{sy}	x, y axis components of stator current
m_0	load torque on the machine shaft
u_{rd}, u_{rq}	d, q axis components of rotor voltage
u_{rx}, u_{ry}	x, y axis components of rotor voltage
u_{sd}, u_{sq}	d, q axis components of stator voltage
u_{sx}, u_{sy}	x, y axis components of stator voltage
e_d	DC-link voltage

Table of contents

Chapter 1

Introduction

Trends towards power generation highlight the shift from large-scale fossil fuel (such as coal and oil) power generation to solar, hydro and wind renewable energy systems. The sharp decline in traditional energy sources has led to higher fuel prices. These assumptions pave the way for expanded use of renewable energy.

Wind Energy Conversion System (WECS) utilizes electrical machines to convert the mechanical energy of the wind into electrical energy. There are a few types of electrical machines commonly used in WECSs: Induction Generators (IGs), Synchronous Generators (SGs) or Self-Excited Induction Generators (SEIGs).

Induction Generators are widely used due to their simplicity and reliability. They allow the production variable reactive power that helps in voltage control of the electrical grid. The machine consists of a stator and a rotor; the stator generates a rotating magnetic field that induces a current in the rotor bars. There are two types of induction generator designs used: a cage rotor design, where the rotor bars are short-circuited, [1–7]; and wound rotor design, [8–12].

Over the past few decades, the Self-Excited Induction Generators have garnered significant research attention due to their simplified operational principle in generating electricity in off-grid, stand-alone scenarios. This generator type can utilize various traditional or renewable energy sources including oil, biofuel and wind. However, the generator has limitations, notably poor voltage and frequency regulations when it experiences undue perturbations in speed and load. The output frequency and generated terminal voltage depend on factors such as excitation capacitance, three-phase induction machine parameters, electrical passive load, and speed, [13–19].

Wound rotor induction machines, also known as Doubly-Fed Induction Machines (DFIMs), are commonly used in WECSs. In a DFIM, there are two sets of windings. One set is connected to the Alternating Current (AC) power grid – most commonly stator, and the other set is connected to a power electronic converter – most commonly rotor. This configuration allows for better control of the generator speed and output voltage.

Doubly-Fed Induction Generators (DFIGs) based systems have been extensively studied and developed since the 1980s; and have become a popular choice for wind power generation due to their high efficiency, low cost, and ease of control. The main reasons for using DFIGs in WECS are:reduced noise, low stress on mechanical structures, independent control of active and reactive powers. Figure 1.1 shows classification of machines used in WECSs.

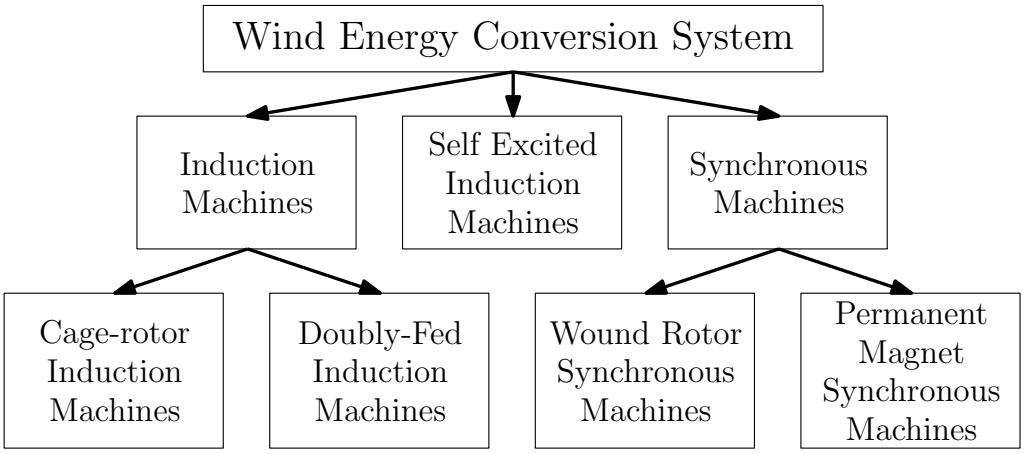

Figure 1.1: Classification of machines used in WECSs

Due to the rapid development and low cost of power electronic converters, they have been widely used in wind power conversion systems since the early 1990s. The rated power of the inverter connected to the rotor circuit is only 30-40% of the rated wind turbine power. For maximum efficiency, the control unit must select the optimum operating point, [20, 21]. Considering the above, it was decided to undertake an analysis of the properties of the Doubly-Fed Induction Generator with Current Source Converter (CSC) connected to the rotor circuit. The topic is vaguely known in the literature of the subject.

Historically, early wind turbine designs used static power converter constructions with a CSC built with Silicon Controlled Rectifiers (SCRs) and thyristors. Such generator systems were widely used in the 1970s and 1980s, [22–25]. These designs

controlled the angle of advance, which is the angle between the stator magnetic field and the rotor position. The control of this angle was limited, which led to reduced efficiency and increased stress on the mechanical components. Furthermore, converters had complicated auxiliary power supply circuits for the thyristors and long switching times.

A significant amount of research conducted on power electronics topologies and their applications in WECSs led to the replacement of this solution by Voltage Source Converters (VSCs) power circuits, where the power switch is based on Silicon Carbide (SiC), [26–29]; and Gallium Nitride (GaN), [30–32] transistors. The introduction of these components made it possible to switch power semiconductors quickly and with lower power losses. However, recently CSC-based drive systems are also gaining popularity because of their unique advantages over VSC systems. Among them, monolithic Insulated Gate Bipolar Transistors (IGBTs) with a series-connected diode, mainly called Reverse-Blocking Insulated Gate Bipolar Transistors (RB-IGBTs) that simplified power systems. The characteristics and potentials of the new power electronics CSC in various applications are described in [33–39].

The control of DFIG can be achieved through various techniques. At present, many works published in the literature show the application of VSC in conjunction with DFIG. Following control methods are applied: Vector Oriented Control (VOC) with stator flux orientation, [40–45] and stator voltage orientation, [46, 47]; Direct Torque Control (DTC), [48–51]; Non-linear Control, [52–55]; Fuzzy Logic Control (FLC) Non-linear Control, [56, 57]. Other control methods are based on multiscalar models, [58–61]. DFIG can also operate as stand-alone system, [62–64]. Specific control methods based on angle synchronization using the Phase Locked Loop (PLL) also can be found in the literature, [65–67]. In case of Permanent Magnet Synchronous Generators (PMSGs) using VOC, various articles have also also listed various control methods, [68–71]. Figure 1.2 shows the classification of the most commonly used control methods for grid operation of WECSs.

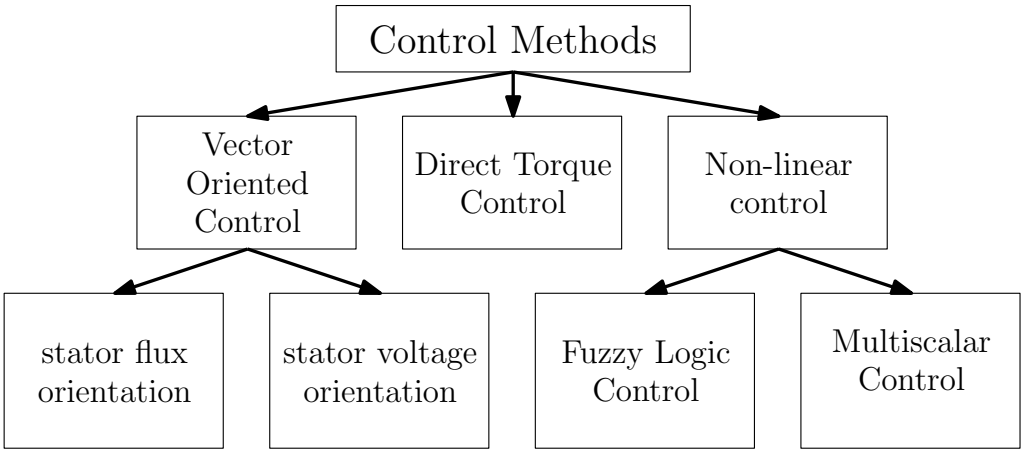

Figure 1.2: Classification of control methods for WECSs grid operation

Recently published articles rarely involve the operational characteristics and technical aspects of the DFIG-CSC system, [72–76]. Most of them dwelt only on theoretical research.Compared to VSC generator systems, CSC-based generator systems have few positive features:

- the length of the cable between the converter and generator has the least impact on the operation of the power supply system;
- the rotor short circuit is treated as a natural working state of the inverter - in the event of a short circuit, the high value of DC choke inductance can protect the system;
- it is not necessary to use a low inductance bus-bar connection between the switching modules of the converter to limit the overvoltage on the transistor during fast switching;
- they can handle oversized motors.

These features greatly simplify the design of the converter. The main disadvantage of CSC-based drive systems is that they are sensitive to open circuit condition. The occurrence of open circuit will induce high voltage and can damage transistor modules. In addition, the inductors in the energy storage circuit can be quite large and expensive. Additionally, CSC produce torque pulsations at very low speed, but that can be compensated by using appropriate control methods.

1.1 Formulation and justification of the research problem

Due to the features of Doubly-Fed Induction Generator and Current Source Converter mentioned above, it was decided to undertake an analysis of the properties of DFIG, in which the stator is connected to the grid and the rotor to a Current Source Converter. This makes it possible to control the values of active and reactive power returned to the grid. Such system allows for bidirectional energy flow.

From the point of view of control theory, a Doubly-Fed Induction Generator is a strongly nonlinear object. In DFIG vector model, there are couplings between the dynamics of individual state variables. The parameters of the generator depend on the temperature and the operating point. The choice of appropriate control variables affects the static and dynamic properties of the generator system.

At present, Field Oriented Control methods are mainly used. FOC is simple to implement in generator systems with CSC, since the active power is proportional to one component of the stator current vector, while the reactive power is shaped by the other component. However, solutions presented in recent scientific papers propose application of the different control methods only for Voltage Source Converter. Some of the examples of the methods can be divided into: Vector Oriented Control with stator flux orientation and with stator voltage orientation, Direct Torque Control, non-linear control. In this dissertation, Field Oriented Control (FOC) derived from the approach shown in respective articles will be investigated. This will allow to set the reference point for the proposed algorithms.

Multiscalar control for DFIG with VSC was first proposed in [77]. Multiscalar control of DFIG with CSC was proposed in [78]. In [75] the control concept was further developed and a full experimental analysis was carried out to confirm the theoretical assumptions. There are only few research works that undertake the analysis of multiscalar control methods, [73–76, 78], for a DFIG with CSC connected to rotor circuit. From this, two main methods can be determined: voltage control and current control.

The control strategy in which one of the control variable is the output current of the inverter can be called current control of Doubly-Fed Induction Generator connected to Current Source Converter. Such method was introduced in [73]. The

main disadvantage of this type of control is that the current value of the DC circuit is constant. As a result, the power losses in the Current Source Inverter are high. In order to solve this problem, DC-link current needs to be generated on the basis of the actual values of the active and reactive power of the stator. However, with this approach, it is necessary to use an additional current regulator in DC-link to determine the e_d voltage value.

Novel non-linear control methods for power flow in Doubly-Fed Induction Generator connected to Current Source Converter will be investigated. Control strategies proposed by the author can be called voltage control because the control variables are the input voltage of the DC-link (e_d) and the angular speed of the generator current vector (ω_i). The main contributions are new feedback linearizations for stator active and reactive powers in the control system structures. Furthermore, new control algorithms allow for independent regulation of the stator active and reactive powers.

In order to apply the voltage approach to DFIG control system in which the control variables are the e_d voltage and the pulsation of the inverter's current output vector ω_i (depending on the adapted reference system) and to determine the exact decoupling functions of the active power control subsystem from the reactive power subsystem, it was decided to use an approach known in the literature as control with transformation to multiscalar variables.

It is possible to linearize the system with a Doubly-Fed Induction Machine using feedback linearization. In case of the Doubly-Fed Induction Generator with Current Source Converter, it is necessary to consider eight state variables of vector model transformation to multiscalar model, [75]. Multiscalar control provides independent control of active and reactive powers. In all of the control structures presented in this dissertation, the following assumptions were made:

- the method of synchronization of the Current Source Converter with the grid is not considered;
- transistors are treated as ideal and lossless elements;
- the inverter is treated as an ideal current commutator of direct current.

The research aims to carry out original theoretical and experimental studies on the control algorithms for Doubly-Fed Induction Generator supplied by Current Source Converter. The proposed control algorithms based on the multiscalar transformation will ensure that all controlled variables will be fully decoupled and

robust to unforeseen circumstances; this is not feasible with Field Oriented Control. Investigation on the FOC will be completed for making a comparative analysis of all proposed control algorithms.

Independent generation of output control vectors for Current Source Inverter (CSI):

- allow to increase the robustness (interpreted as resistance to sudden changes in power, uncertainty of parameters as well as voltage collapse) of the system during transient and steady states of a Doubly-Fed Induction Generator;
- grant the independence from the provided circuit parameters.

The four proposed methods will be compared in simulations and at experimental setup with commonly used FOC. The comparative analysis between those control strategies will be shown.

The goal of the research is to develop robust control methods that can ensure stable and efficient operation of the DFIG system, which is critical in Wind Energy Conversion Systems. To achieve this, a control methods based on linearization with feedback of a non-linear object such as Doubly-Fed Induction Generator was undertaken. The primary benefits of the proposed methods include addressing stability issues inherent in conventional approaches, enhancing system robustness by mitigating uncertainties in circuit parameters and minimizing oscillations during both dynamic and steady operational phases. The dissertation will cover theoretical concepts related to DFIG systems, including the mathematical model of the generator and utilized control algorithms. Simulation tests will be carried out to validate the theoretical concepts. Practical experiments will also be conducted in a laboratory setup to verify the effectiveness of the proposed control methods.

The principal objectives of the research are:

- examination of general principles of commonly used control schemes for Current Source Converter (CSC) paired with Doubly-Fed Induction Generator (DFIG) - firstly as simulation implementation of the system and next with verification of theoretical concepts at a prototype laboratory stand;
- examination of proposed control algorithms for the CSC paired with DFIG in simulations and at experimental setup;
- investigations of similarities and differences between commonly used methods and proposed algorithms, to perform a comparative analysis and point out the

best method among them in terms of robustness and dynamics for practical use cases;

- further development of the proposed control algorithms on the experimental bench and proving the theoretical concepts behind them;
- examination of control methods behaviour in case of the faulty state as voltage dips (in the experiments, voltage dips were limited to 70-75% of the nominal grid voltage value).

Referring to the above statements, thesis will be defined as:

The proposed control structures with multiscalar variables of Doubly-Fed Induction Generator combined with Current Source Converter in the rotor circuit enable independent and fully decoupled control of active and reactive power and reliability during normal operation as well as in the case of voltage dips.

1.2 Research methodology

The doctoral research foresees the combined use of a Doubly-Fed Induction Generator with a two-level three-phase Current Source Converter. This type of converter is commonly used in industrial applications that require higher efficiency and constant power, such as wind power generation. Current Source Converters are very rarely used in low power applications; most of the research reports are focused on high-power thyristor-based converters (above 1MW). Research aims to conduct original theoretical, simulation and experimental studies to expand the knowledge in the field of CSC control methods used in conjunction with DFIG. The proposed control methods rely on multiscalar variable transformations. These conversion techniques ensure full decoupling of control sub-paths. The developed methods will be benchmarked against industry standard approaches, such as vector-oriented control. Comparative analyses will be conducted based on factors including transient response speed, robustness, handling of machine parameter uncertainties, and response to fault states.

Theoretical research will form an important part of the doctoral dissertation. The mathematical model of the Doubly-Fed Induction Generator connected to the two-level Current Source Inverter will be established by transformation of the natural three-phase reference system (abc) to fixed orthogonal coordinates (α-β). Subsequently, depending on the selected control strategy, the model will be

further transformed to either the rotating orthogonal coordinates d-q system for Field Oriented Control or reference system that rotates with either inverter output current vector or generator current vector. In the latter case, the parameters of the output stage filter will also be considered in the calculations. The obtained model will allow verification of the control method proposed in the simulation.

Simulations were carried out in the PLECS environment. This program is widely used in the field of power electronics and allows not only to test the authenticity of the control schemes but will also provide data on the characteristics of the inputs and outputs of the circuits for the control methods used. The simulation of the control structures used C language functions that have been formulated by the author. The developed software was written as an emulation of a real control board structure with Digital Signal Processor (DSP) and Field Programmable Gate Array (FPGA). This allowed for immediate portability of solutions without additional code rewriting.

The experimental study was conducted using two-stage three-phase CSC. Inverter control board based on Digital Signal Processor (DSP) and Field Programmable Gate Array (FPGA). The DSP is responsible for all calculations related to control and the PC communication layer managed by the operator console. FPGA processes accurate timing signals, such as analog-to-digital conversion and signal generation of the controller based on calculations performed by DSP.

Chapter 2

Wind Energy Conversion Systems

Harnessing wind energy through turbines involves the conversion of available wind power into mechanical power; a process influenced by numerous factors. Factors such as turbine design, its geographical placement and environmental conditions such as wind speed and air density play crucial roles in determining this conversion efficiency, [20]. The fraction of available wind power that can be effectively captured and converted by the turbine blades into mechanical power on the generator shaft. For steady-state conditions mechanical power can be described by following equation:

$$P_{mech} = \frac{1}{2}\rho A_r C_p\left(\lambda, \beta\right)\omega^3 \tag{2.1}$$

where C_p is the power coefficient as function of the pitch angle β and the tip speed ratio λ, ρ is the air density, ω is the wind speed, A_r denotes the area swept by the rotor blades.

Figure 2.1 shows generic power curve of the wind turbine, [79]. Four operating regions can be distinguished:

- Region 1 - wind torque is insufficient to rotate turbine blades;
- Region 2 - wind turbine is able to generate power below nominal value;
- Region 3 - nominal power generation;
- Region 4 - wind turbine is switched off for higher wind speeds to avoid the damage.

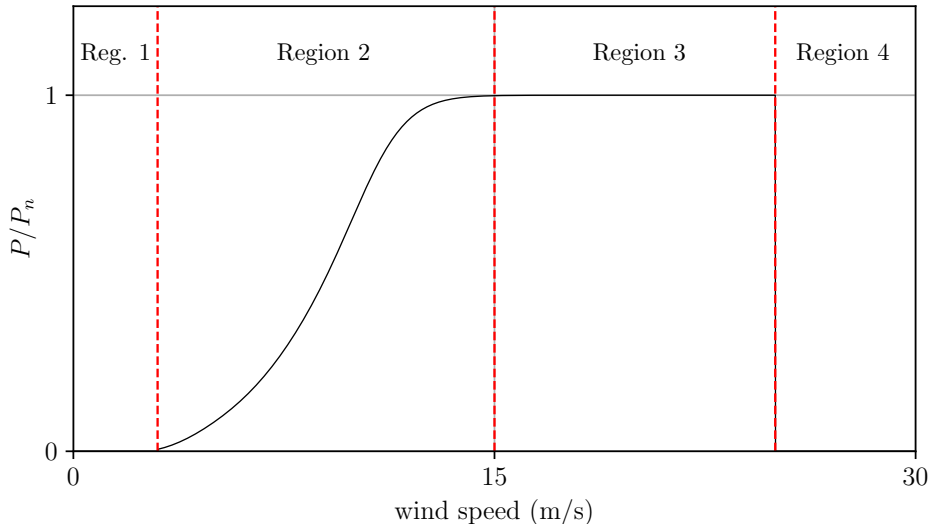

Figure 2.1: Generic wind turbine power curve

2.1 Conversion systems topologies

Wind turbines have the capability to function at either fixed or variable speeds. Given their low rotational speed, synchronization with the power grid frequency is essential, [80]. This can be achieved through two methods:

- mechanically - with the use of the gearbox;
- electrically - with the number of pole pairs that set rotational speed of the generator.

Fixed-speed wind turbine uses the Induction Generator (IG) directly connected to the electrical grid as shown in Figure 2.2. The rotational speed - grid frequency matching can be established through either gearbox ratio or pole pairs. Capacitor bank is used to smoothen the generator output voltage.

Incorporating a converter units, as depicted in Figure 2.3 and Figure 2.4, enables power generation across a broad spectrum of wind speeds. Major disadvantage of this approach is the necessity to design a converter capable of handling the full power output from the wind turbine. These systems can utilize various generator types including Induction Generator (IG), Permanent Magnet Synchronous Generator (PMSG) and Synchronous Generator (SG).

Figure 2.5 shows variable-speed wind turbine with Doubly-Fed Induction

Machine (DFIM). Stator of the DFIM is connected directly to the power grid, while converter is connected to the rotor windings via slip rings. This configuration offers the advantage of reducing the size, losses, and cost of the converter unit since it only needs to manage a portion of the rated power, typically up to 30%.

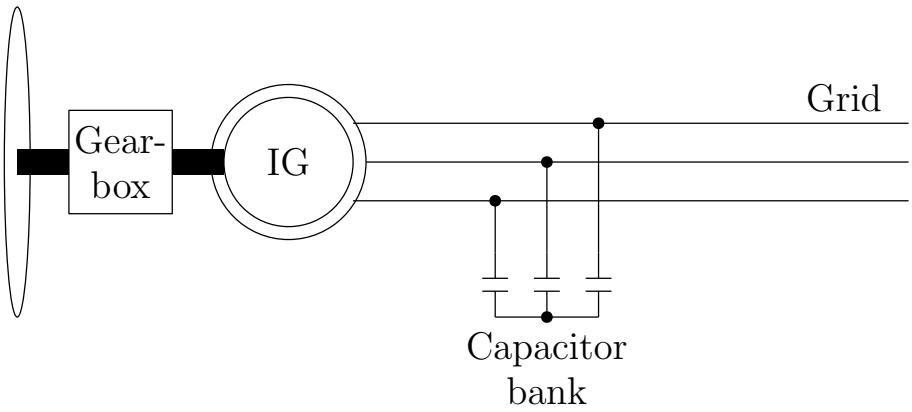

Figure 2.2: Fixed-speed wind turbine with a Induction Generator (IG)

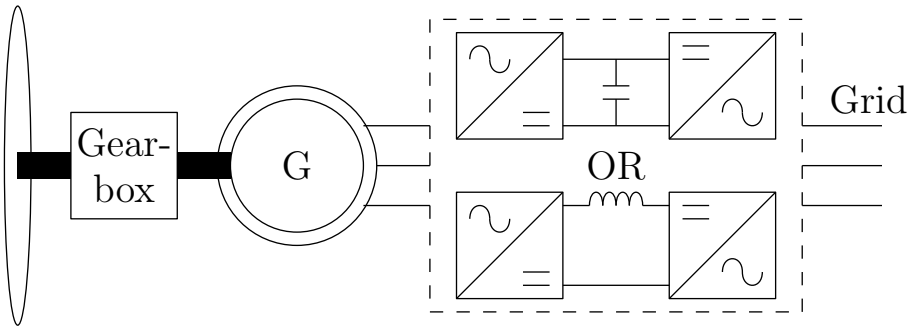

Figure 2.3: Variable-speed wind turbine with a synchronous/induction generator

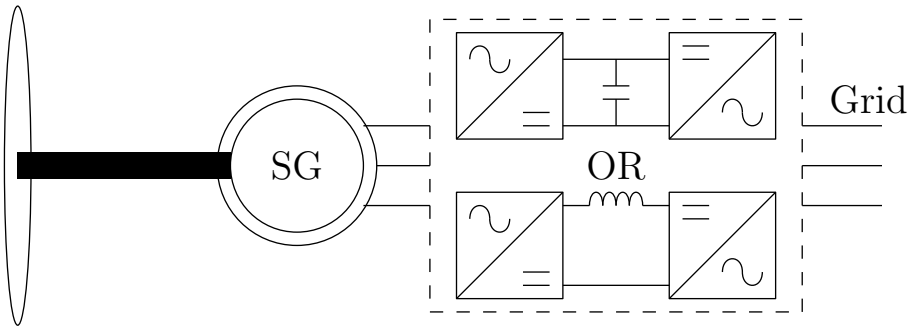

Figure 2.4: Variable-speed gear-less wind turbine with a Synchronous Generator (SG)

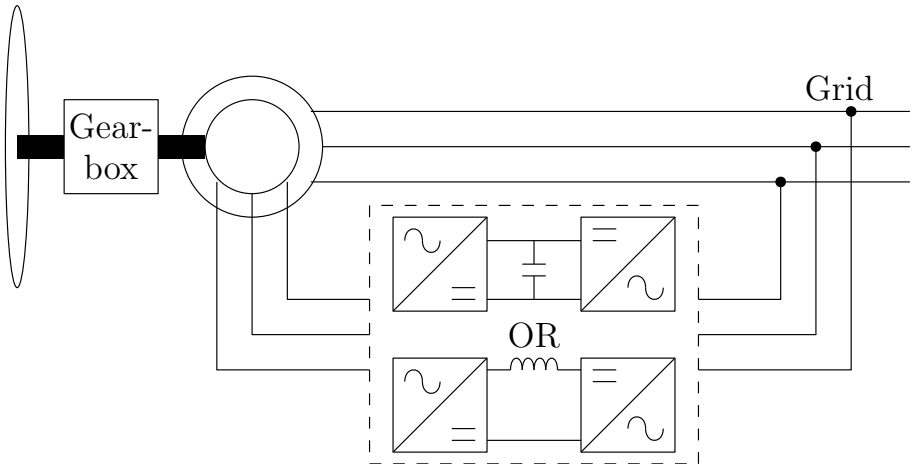

Figure 2.5: Variable-speed wind turbine with a Doubly-Fed Induction Generator (DFIG)

The dissertation focuses on the analysis of the system with DFIG shown in Figure 2.5. Wind turbine and gearbox will be modeled by induction machine, driven by commercial converter, connected to the Doubly-Fed Induction Generator (DFIG) shaft via clutch.

2.2 Doubly-Fed Induction Generator mathematical model

The mathematical model of the asynchronous machine used for the synthesis of control systems is obtained on the basis of the following assumptions, [81]:

- phase windings are symmetrical;
- magnetic circuits are symmetrical;
- distribution of phase windings around the stator and rotor is continuous;
- stator and rotor surfaces are smooth;
- air gap is uniform;
- distribution of the magnetic field in the air gap is sinusoidal;
- distribution of the magnetic field in the gap does not change when the ferromagnets are saturated;
- magnetization characteristics of the main circuit is explicit;
- phenomenon of current displacement is omitted;
- energy losses in magnetic circuits are omitted;

- capacitances between windings and phases are omitted;
- there is no deformation of the magnetic field at the edges of the magnetic circuit and in the ventilation slots of the sheet packages.

These assumptions allow the creation of an equivalent circuit presented in Figure 2.6 as well as a mathematical model described using general vector differential equations, [82]:

$$\vec{u_s} = \vec{R_s}\vec{i_s} + \frac{d\vec{\Psi}_s}{d\tau} + j\omega_a\vec{\Psi}_s \tag{2.2}$$

$$\vec{u_r} = \vec{R_r}\vec{i_r} + \frac{d\vec{\Psi}_r}{d\tau} + j\left(\omega_a - \omega_r\right)\vec{\Psi}_r \tag{2.3}$$

$$J\frac{d\omega_r}{d\tau} = Im\left|\vec{\Psi}_s^*\vec{i_s}\right| - m_0 \tag{2.4}$$

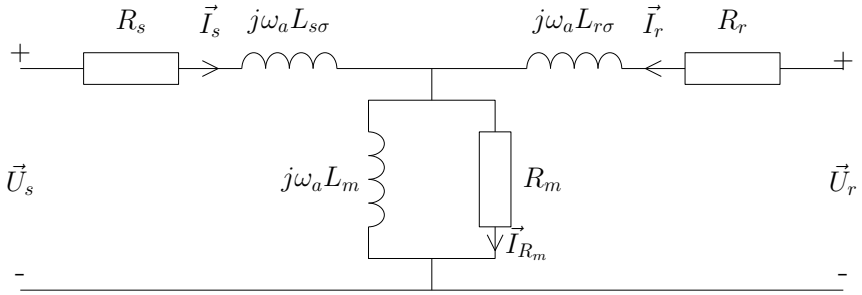

Figure 2.6: Equivalent circuit of DFIG

The most common approach to DFIG control has been adapted from three-phase squirrel-cage machines. It can be based on rotor or stator flux vector orientation, [43,44]. In the Park frame, the DFIG voltage and flux equations for stator and rotor are derived directly from the asynchronous mechanical equations shown below:

$$u_{sd} = R_s i_{sd} + \frac{d\Psi_{sd}}{d\tau} - \omega_a\Psi_{sq} \tag{2.5}$$

$$u_{sq} = R_s i_{sq} + \frac{d\Psi_{sq}}{d\tau} + \omega_a\Psi_{sd} \tag{2.6}$$

$$u_{rd} = R_r i_{rd} + \frac{d\Psi_{rd}}{d\tau} - \left(\omega_a - \omega_r\right)\Psi_{rq} \tag{2.7}$$

$$u_{rd} = R_r i_{rq} + \frac{d\Psi_{rq}}{d\tau} - \left(\omega_a - \omega_r\right)\Psi_{rd} \tag{2.8}$$

$$\frac{d\omega_r}{d\tau} = \frac{L_m}{JL_s}\left(\Psi_{sd} i_{sq} - \Psi_{sq} i_{sd}\right) - \frac{1}{J} m_0 \tag{2.9}$$

$$\Psi_{sd} = L_s i_{sd} + L_m i_{rd} \tag{2.10}$$

$$\Psi_{sq} = L_s i_{sq} + L_m i_{rq} \tag{2.11}$$

$$\Psi_{rd} = L_r i_{rd} + L_m i_{sd} \tag{2.12}$$

$$\Psi_{rq} = L_r i_{rq} + L_m i_{sq} \tag{2.13}$$

where R_s and R_r denote the stator and rotor resistances, L_s, L_r, L_m represent the stator, rotor and mutual inductances $\vec{\Psi}_s$, $\vec{u_s}$, $\vec{i_s}$ indicate stator flux, voltage and current vectors and $\vec{\Psi}_r$, $\vec{u_r}$, $\vec{i_r}$ are rotor flux, voltage and current vectors, ω_r denotes rotor angular speed, ω_a denotes angular speed of the coordinate system.

Assuming that the d-q coordinate system is linked to the stator flux vector as shown in Figure 2.7 (where α_S, β_S denote axes of the stationary stator reference system and α_R, β_R denote axes of the stationary rotor reference system), $\Psi_{sq} = 0$ and $\Psi_{sd} = \vec{\Psi}_s$:

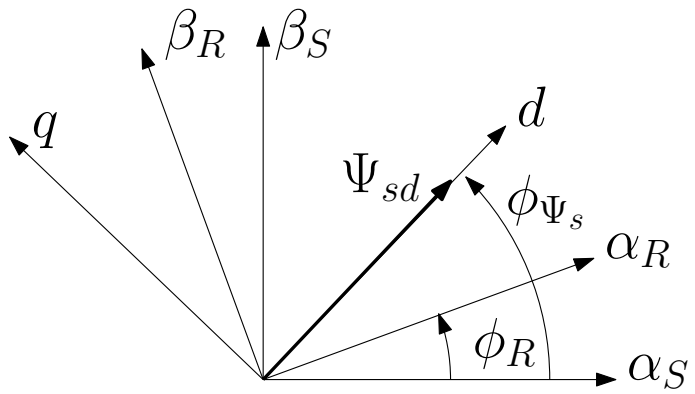

Figure 2.7: Coordinate system orientation for Field Oriented Control

The dynamics of the Doubly-Fed Induction Generator in the form of a vector is expressed in any possible frame of reference, which rotates with ω_a, [59]. The author chose the x-y reference frame, where the x-axis connected with inverter output current vector $\vec{i_r}$:

$$\frac{d\Psi_{sx}}{d\tau} = -\frac{R_s}{L_s}\Psi_{sx} + \frac{R_s L_m}{L_s} i_{rx} + \omega_a \Psi_{sy} + u_{sx} \tag{2.14}$$

$$\frac{d\Psi_{sy}}{d\tau} = -\frac{R_s}{L_s}\Psi_{sy} + \frac{R_s L_m}{L_s} i_{ry} - \omega_a \Psi_{sx} + u_{sy} \tag{2.15}$$

$$\begin{aligned}\frac{di_{rx}}{d\tau} =& -\frac{L_s^2 R_r + L_m^2 R_s}{L_s w_\delta} i_{rx} + \frac{R_s L_m}{L_s w_\delta}\Psi_{sx} + (\omega_a - \omega_r)\, i_{ry} + \\ & - \frac{L_m}{w_\delta}\omega_r \Psi_{sy} + \frac{L_s}{w_\delta} u_{rx} - \frac{L_m}{w_\delta} u_{sx}\end{aligned} \tag{2.16}$$

$$\begin{aligned}\frac{di_{ry}}{d\tau} =& -\frac{L_s^2 R_r + L_m^2 R_s}{L_s w_\delta} i_{ry} + \frac{R_s L_m}{L_s w_\delta}\Psi_{sy} - (\omega_a - \omega_r)\, i_{rx} + \\ & + \frac{L_m}{w_\delta}\omega_r \Psi_{sx} + \frac{L_s}{w_\delta} u_{ry} - \frac{L_m}{w_\delta} u_{sy}\end{aligned} \tag{2.17}$$

$$\frac{d\omega_r}{d\tau} = \frac{L_m}{J L_s}\left(\Psi_{sx} i_{ry} - \Psi_{sy} i_{rx}\right) - \frac{1}{J} m_0 \tag{2.18}$$

and:

$$w_\delta = L_s L_r - L_m^2 \tag{2.19}$$

where R_s and R_r are the stator and rotor resistances, L_s, L_r, L_m are the stator, rotor and mutual inductance, $\vec{\Psi}_s$, $\vec{u_s}$ indicate stator flux and voltage vectors and $\vec{i_r}$, $\vec{u_r}$ represent rotor current and voltage vectors, ω_r denotes rotor angular speed, ω_a denotes the angular speed of rotation of the coordinate system. Figure 2.8 shows the vector orientation of the reference frame, where α_S, β_S denote axes of the stationary stator reference system and α_R, β_R denote axes of the stationary rotor reference system.

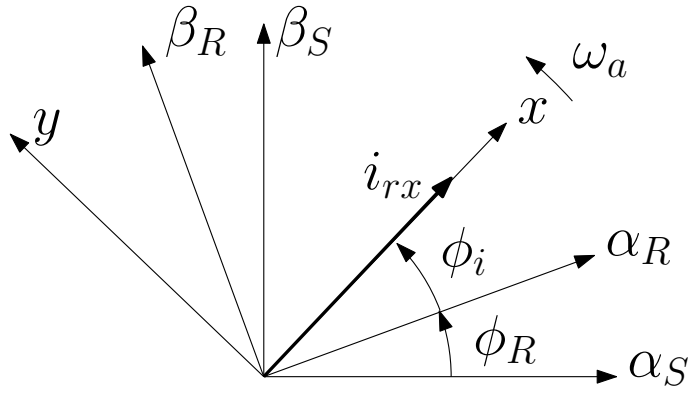

Figure 2.8: Coordinate system orientation for Multiscalar Control System

The mathematical model (2.5) – (2.13) will be used to synthesize the Field Oriented Control system; while (2.14) – (2.18) to synthesize the control systems proposed by the author of the thesis in Sections 3.2 – 3.4.

Chapter 3

Control methods

This chapter presents the structures of commonly used Field Oriented Control method for Doubly-Fed Induction Generator, proposed by the author four multiscalar control methods, as well as stability of linearized control systems using multiscalar transformations. FOC was chosen as the reference method due to its frequent use in industrial solutions. Choosing this method will allow to compare the transient-state and steady-state behaviour of the control methods proposed by the author with industrial standards. This chapter is divided into six sections:

- Field Oriented Control - described in Section 3.1;
- Multiscalar control structure 1 - described in Section 3.2;
- Multiscalar control structure 2 - described in Section 3.3;
- Multiscalar control structure 3 - described in Section 3.4;
- Multiscalar control structure 4 - described in Section 3.5;
- Stability of linearized control systems using multiscalar transformations - described in Section 3.6.

3.1 Field Oriented Control

In Doubly-Fed Induction Generator system, the rotor side Current Source Converter controls the value of the electromagnetic torque of the machine based on stator active and reactive powers. Converter in the rotor side generates current vectors to rotor windings that corresponds to the desired powers. Equations (2.10) and (2.11) shown also in [40] can be written as:

$$\Psi_{sd} = L_s i_{sd} + L_m i_{rd} \tag{3.1}$$

$$\Psi_{sq} = L_s i_{sq} + L_m i_{rq} = 0 \tag{3.2}$$

From these equations, the stator current components can be formed as:

$$i_{sd} = \frac{1}{L_s}\left(\Psi_s - L_m i_{rd}\right) \tag{3.3}$$

$$i_{sq} = -\frac{L_m}{L_s} i_{rq} \tag{3.4}$$

The stator active and reactive powers are written in d-q coordinates:

$$p_s = u_{sd} i_{sd} + u_{sq} i_{sq} \tag{3.5}$$

$$q_s = u_{sq} i_{sd} - u_{sd} i_{sq} \tag{3.6}$$

Additionally, considering only steady state, it can be assumed that: $u_{sd} \approx 0$ and $u_{sq} = u_s \approx \frac{\Psi_s}{\omega_s}$. After that equations (3.5) and (3.6) can be rewritten as:

$$p_s = -\frac{\Psi_s L_m}{\omega_s L_s} i_{rq} \tag{3.7}$$

$$q_s = \frac{\Psi_s^2}{\omega_s L_s} - \frac{\Psi_s L_m}{\omega_s L_s} i_{rd} \tag{3.8}$$

Assuming that the grid frequency is invariant and equal to the nominal value during the impulse period, the pulsation can be defined as $\omega_s = 1\,(p.u.)$ and above equations can be simplified to:

$$p_s = -\frac{\Psi_s L_m}{L_s} i_{rq} \tag{3.9}$$

$$q_s = \frac{\Psi_s^2}{L_s} - \frac{\Psi_s L_m}{L_s} i_{rd} \tag{3.10}$$

Finally, by utilizing equations (3.9) and (3.10), it is possible to derive equations for the components of the rotor current:

$$i_{rq} = -\frac{L_s p_s}{\Psi_s L_m} \tag{3.11}$$

$$i_{rd} = \frac{\Psi_s}{L_m} - \frac{L_s}{\Psi_s L_m} q_s \tag{3.12}$$

Then, additional decoupling variables were introduced to improve the quality of regulation (better tracking of setpoints and minimalization of errors). Those variables are derived from active and reactive power equations. Considering that in steady state $\Psi_s \approx 1$ the final set of control variables for the modulator block is as follows:

$$u_1 = -\frac{1}{L_m} - \frac{L_s}{L_m} m_2 \tag{3.13}$$

$$u_2 = -\frac{L_s}{L_m} m_1 \tag{3.14}$$

Variables m_1 and m_2 can be defined as outputs of Proportional Integral (PI) controllers:

$$m_1 = k_p \left(P_{ref} - p_s\right) + k_i \int \left(P_{ref} - p_s\right) dt \tag{3.15}$$

$$m_2 = k_p \left(Q_{ref} - q_s\right) + k_i \int \left(Q_{ref} - q_s\right) dt \tag{3.16}$$

where k_p and k_i denote controllers gains, P_{ref}, Q_{ref} are reference values of active and reactive powers. Figure 3.1 shows the control structure.

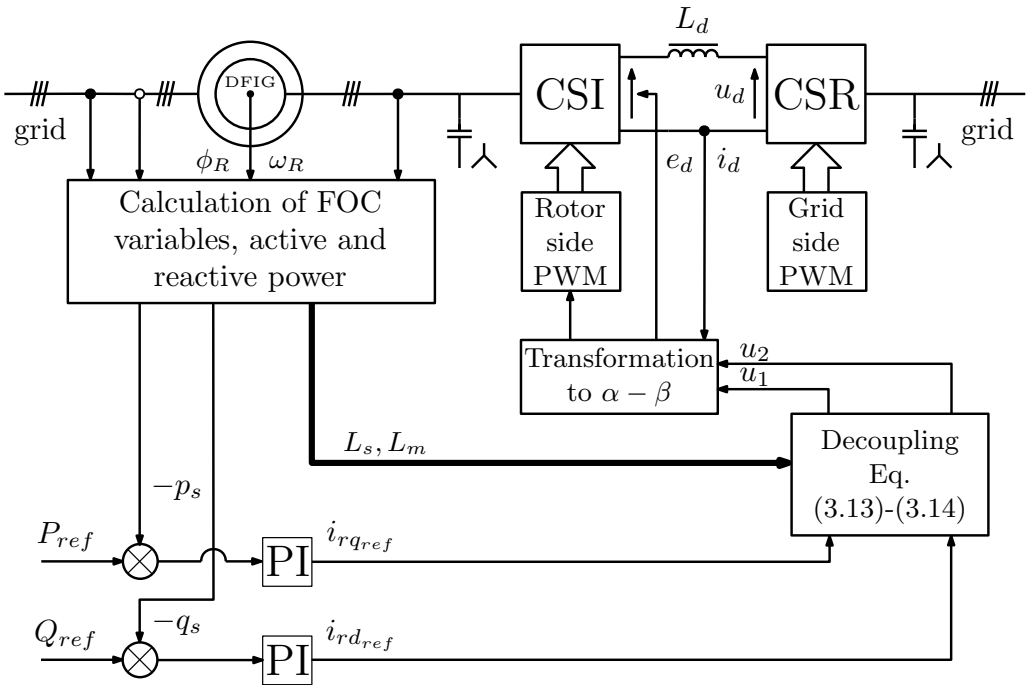

Figure 3.1: Field Oriented Control structure of the Doubly Fed Induction Generator

3.2 Multiscalar control structure 1

The rotor speed and square of stator flux vector components are not directly controlled in the Doubly-Fed Induction Generator (DFIG). Control system aims to stabilize the active and reactive powers. Therefore, the generic input-output transformation is not suitable for power control of DFIG with the CSC. The rank of the examined system is $r = 8$, [75]. The transformation should be extended to the CSC equations. The rotor side Current Source Converter is considered as the ideal commutator working with a constant modulation index $M_i = 1$.

Providing that the control variables are the DC-link input voltage e_d and angular speed of output current ω_{ir}, it is possible to maintain the reference values of powers. This approach, presented previously in [74] grants controllability of DC-link current and gives better use of grid power. In case of this method x-y coordinate system is tied to x component of the rotor current: $i_{rx} = M_i i_d$ and $i_{ry} = 0$. Assuming a very small output capacitance it can be assumed that $u_{rx} = M_i e_d$. In line with this premise, the dc-link and capacitor C_m differential equations are as follow:

$$\frac{di_d}{d\tau} = \frac{1}{L_d}\left(e_d - R_d i_d - e_q\right) \tag{3.17}$$

$$\frac{du_{cx}}{d\tau} = \frac{1}{C_m}\left(i_{fx} - i_{rx}\right) + \omega_{ir} u_{cy} \tag{3.18}$$

$$\frac{du_{cy}}{d\tau} = \frac{1}{C_m}\left(i_{fy} - i_{ry}\right) - \omega_{ir} u_{cx} \tag{3.19}$$

and:

$$u_{rx} = R_c\left(i_{fx} - i_{rx}\right) + u_{cx} \tag{3.20}$$

$$u_{ry} = R_c\left(i_{fy} - i_{ry}\right) + u_{cy} \tag{3.21}$$

$$e_q = \frac{\left(u_{rx} i_{fx} + u_{ry} i_{fy}\right)}{i_d} \tag{3.22}$$

The stator active and reactive power can be defined as:

$$p_s = u_{sx} i_{sx} + u_{sy} i_{sy} \tag{3.23}$$

$$q_s = u_{sy} i_{sx} - u_{sx} i_{sy} \tag{3.24}$$

The assumption made for the steady state that $\Psi_{sx} \approx -\frac{u_{sy}}{\omega_s}$, $\Psi_{sy} \approx \frac{u_{sx}}{\omega_s}$ and $\omega_s \approx 1$, where ω_s is the angular speed of grid voltage vector and is assumed constant during tests, makes that the active (3.23) and reactive (3.24) power can be redefined as:

$$z_2 = \Psi_{sy} i_{sx} - \Psi_{sx} i_{sy} \tag{3.25}$$

$$z_4 = -\Psi_{sx} i_{sx} - \Psi_{sy} i_{sy} \tag{3.26}$$

After taking into account the equation (3.17), the final set of mathematical relationships, based on which the control will be determined, can be presented as follows:

$$\frac{d\Psi_{sx}}{d\tau} = -\frac{R_s}{L_s}\Psi_{sx} + \frac{L_m R_s}{L_s} i_{rx} + \Psi_{sy}\left(\omega_{ir} + \omega_r\right) + u_{sx} \tag{3.27}$$

$$\frac{d\Psi_{sy}}{d\tau} = -\frac{R_s}{L_s}\Psi_{sy} - \Psi_{sx}\left(\omega_{ir} + \omega_r\right) + u_{sy} \tag{3.28}$$

$$\frac{di_{rx}}{d\tau} = -\frac{\left(L_m^2 R_s + L_s^2 R_r\right)}{L_s w_\delta} i_{rx} - \frac{L_m}{w_\delta}\Psi_{sy}\omega_r - \frac{L_m}{w_\delta} u_{sx} + \frac{L_m R_s}{L_s w_\delta}\Psi_{sx} + \frac{L_s}{w_\delta} u_{rx} \tag{3.29}$$

$$\begin{aligned}\frac{di_{sx}}{d\tau} =& -\left(\frac{R_s}{L_s^2}+\frac{L_m^2R_s}{L_s^2w_\delta}\right)\Psi_{sx}+\left(\frac{L_m^3R_s}{L_s^2w_\delta}+\frac{L_mR_r}{w_\delta}+\frac{L_mR_s}{L_s^2}\right)i_{rx}+\\ &+\left(\frac{1}{L_s}+\frac{L_m^2}{L_sw_\delta}\right)\Psi_{sy}\omega_r+\left(\frac{L_m^2}{L_sw_\delta}+\frac{1}{L_s}\right)u_{sx}+\frac{1}{L_s}\Psi_{sy}\omega_{ir}-\frac{L_m}{w_\delta}u_{rx}\end{aligned} \tag{3.30}$$

$$\frac{di_{sy}}{d\tau} = -\frac{R_s}{L_s^2}\Psi_{sy}-\frac{1}{L_s}\Psi_{sx}\omega_r+\frac{1}{L_s}u_{sy}-\frac{1}{L_s}\Psi_{sx}\omega_{ir} \tag{3.31}$$

$$\frac{d\omega_r}{d\tau} = -\frac{L_m}{JL_s}\Psi_{sy}i_{rx}-\frac{1}{J}m_0 \tag{3.32}$$

The proposed transformations of the generator state variables to multiscalar form:

$$z_{11} = \omega_r \tag{3.33}$$

$$z_2 = \Psi_{sy}i_{sx}-\Psi_{sx}i_{sy} \tag{3.34}$$

$$z_{21} = \Psi_{sx}^2+\Psi_{sy}^2 \tag{3.35}$$

$$z_4 = -\Psi_{sx}i_{sx}-\Psi_{sy}i_{sy} \tag{3.36}$$

$$z_{31} = u_{cx}\Psi_{sy}-u_{cy}\Psi_{sx} \tag{3.37}$$

$$z_{32} = u_{cx}\Psi_{sx}+u_{cy}\Psi_{sy} \tag{3.38}$$

$$z_{41} = i_{fx} \tag{3.39}$$

$$z_{42} = i_{fy} \approx 0 \tag{3.40}$$

Considering the proposed multiscalar transformation (3.33) – (3.40), the dynamics of the system can be described by following set of the differential equations:

$$\frac{dz_{11}}{d\tau} = -\frac{L_m}{JL_s}\left(\Psi_{sy}i_{rx}\right)-\frac{1}{J}m_0 \tag{3.41}$$

$$\begin{aligned}\frac{dz_2}{d\tau} =& -\frac{R_s}{L_s}z_2+\left(\frac{z_{21}}{L_s}-z_4+\frac{L_m^2}{L_sw_\delta}\Psi_{sy}^2\right)z_{11}+\frac{1}{L_s}\left(\Psi_{sy}u_{sx}-\Psi_{sx}u_{sy}\right)+\\ &+\left(\frac{L_m^3R_s}{L_s^2w_\delta}+\frac{L_mR_r}{w_\delta}+\frac{L_mR_s}{L_s^2}\right)\Psi_{sy}i_{rx}-\frac{L_mR_s}{L_s}i_{sy}i_{rx}+\\ &+\frac{L_m^2}{L_sw_\delta}\Psi_{sy}u_{sx}-\frac{L_m^2R_s}{L_s^2w_\delta}\Psi_{sx}\Psi_{sy}+q_s+u_1\end{aligned} \tag{3.42}$$

$$\frac{dz_{21}}{d\tau} = -2\left(\frac{R_s}{L_s}z_{21} - \frac{L_m R_s}{L_s}\Psi_{sx}i_{rx} - \Psi_{sx}u_{sx} - \Psi_{sy}u_{sy}\right) \tag{3.43}$$

$$\begin{aligned}\frac{dz_4}{d\tau} =& -\frac{R_s}{L_s}z_4 - \left(\frac{L_m^2}{L_s w_\delta}\Psi_{sy}\Psi_{sx} + z_2\right)z_{11} + \frac{R_s}{L_s^2}z_{21} - p_s + \\ &- \left(\frac{L_m^3 R_s}{L_s^2 w_\delta} + \frac{L_m R_r}{w_\delta} + \frac{L_m R_s}{L_s^2}\right)\Psi_{sx}i_{rx} + \frac{L_m^2 R_s}{L_s^2 w_\delta}\Psi_{sx}^2 + \\ &- \frac{L_m R_s}{L_s}i_{rx}i_{sx} - \frac{1}{L_s}\left(\Psi_{sx}u_{sx} + \Psi_{sy}u_{sy}\right) - \frac{L_m^2}{L_s w_\delta}\Psi_{sx}u_{sx} + u_2\end{aligned} \tag{3.44}$$

$$\begin{aligned}\frac{dz_{31}}{d\tau} =& -\frac{R_s}{L_s}z_{31} - z_{11}z_{32} - \frac{L_m R_s}{L_s}i_{rx}u_{cy} + u_{cx}u_{sy} - u_{cy}u_{sx} + \\ &+ \frac{1}{C_m}\left(\Psi_{sy}i_{fx} - \Psi_{sx}i_{fy}\right) + \frac{1}{C_m}\left(\Psi_{sx}i_{ry} - \Psi_{sy}i_{rx}\right)\end{aligned} \tag{3.45}$$

$$\begin{aligned}\frac{dz_{32}}{d\tau} =& -\frac{R_s}{L_s}z_{32} - z_{11}z_{31} + \frac{L_m R_s}{L_s}i_{rx}u_{cx} + u_{cx}u_{sx} + u_{cy}u_{sy} + \\ &+ \frac{1}{C_m}\left(\Psi_{sx}i_{fx} + \Psi_{sy}i_{fy}\right) - \frac{1}{C_m}\left(\Psi_{sx}i_{rx} + \Psi_{sy}i_{ry}\right)\end{aligned} \tag{3.46}$$

$$\frac{dz_{41}}{d\tau} = \frac{1}{L_d}\left(e_d - R_d z_{41} - u_{rx}\right) \tag{3.47}$$

$$\frac{dz_{42}}{d\tau} = 0 \tag{3.48}$$

where:

$$u_1 = \left(z_4 + \frac{z_{21}}{L_s}\right)\omega_{ir} - \frac{L_m}{w_\delta}\Psi_{sy}e_d \tag{3.49}$$

$$u_2 = -z_2\omega_{ir} + \frac{L_m}{w_\delta}\Psi_{sx}e_d \tag{3.50}$$

As can be seen control variables occur only in equations (3.42) and (3.44). Equations (3.45) and (3.46) describe dynamics of the output filter. Applying Static State Feedback Law to differential equations (3.42) and (3.44) the following form of equations can be obtained:

$$\frac{dz_2}{d\tau} = \frac{1}{T}\left(-z_2 + m_1\right) \qquad \frac{dz_4}{d\tau} = \frac{1}{T}\left(-z_4 + m_2\right)$$

where:

$$\begin{aligned} m_1 =& T\left[u_1 + \left(\frac{z_{21}}{L_s} - z_4 + \frac{L_m^2}{L_s w_\delta}\Psi_{sy}^2\right) z_{11} + \frac{1}{L_s}\left(\Psi_{sy}u_{sx} - \Psi_{sx}u_{sy}\right) + \right. \\ &+ \left(\frac{L_m^3 R_s}{L_s^2 w_\delta} + \frac{L_m R_r}{w_\delta} + \frac{L_m R_s}{L_s^2}\right)\Psi_{sy} i_{rx} - \frac{L_m R_s}{L_s} i_{sy} i_{rx} + \\ &\left. + \frac{L_m^2}{L_s w_\delta}\Psi_{sy} u_{sx} - \frac{L_m^2 R_s}{L_s^2 w_\delta}\Psi_{sx}\Psi_{sy} + q_s\right] \end{aligned} \tag{3.51}$$

$$\begin{aligned} m_2 =& T\left[u_2 - \left(\frac{L_m^2}{L_s w_\delta}\Psi_{sy}\Psi_{sx} + z_2\right) z_{11} + \frac{R_s}{L_s^2} z_{21} - p_s + \right. \\ &- \left(\frac{L_m^3 R_s}{L_s^2 w_\delta} + \frac{L_m R_r}{w_\delta} + \frac{L_m R_s}{L_s^2}\right)\Psi_{sx} i_{rx} + \frac{L_m^2 R_s}{L_s^2 w_\delta}\Psi_{sx}^2 + \\ &\left. - \frac{L_m R_s}{L_s} i_{rx} i_{sx} - \frac{1}{L_s}\left(\Psi_{sx}u_{sx} + \Psi_{sy}u_{sy}\right) - \frac{L_m^2}{L_s w_\delta}\Psi_{sx} u_{sx}\right] \end{aligned} \tag{3.52}$$

Obtained variables m_1 and m_2 are new controls and take form showed in (3.51) and (3.52), respectively. Variables u_1 and u_2 present in (3.42) and (3.44) are used to compensate the coupling between new state variables in the presented system:

$$\begin{aligned} u_1 =& \frac{1}{T} m_1 - \left(\frac{z_{21}}{L_s} - z_4 + \frac{L_m^2}{L_s w_\delta}\Psi_{sy}^2\right) z_{11} - \frac{1}{L_s}\left(\Psi_{sy}u_{sx} - \Psi_{sx}u_{sy}\right) + \\ &- \left(\frac{L_m^3 R_s}{L_s^2 w_\delta} + \frac{L_m R_r}{w_\delta} + \frac{L_m R_s}{L_s^2}\right)\Psi_{sy} i_{rx} + \frac{L_m R_s}{L_s} i_{sy} i_{rx} + \\ &- \frac{L_m^2}{L_s w_\delta}\Psi_{sy} u_{sx} + \frac{L_m^2 R_s}{L_s^2 w_\delta}\Psi_{sx}\Psi_{sy} - q_s \end{aligned} \tag{3.53}$$

$$\begin{aligned} u_2 =& \frac{1}{T} m_2 + \left(\frac{L_m^2}{L_s w_\delta}\Psi_{sy}\Psi_{sx} + z_2\right) z_{11} - \frac{R_s}{L_s^2} z_{21} + p_s + \\ &+ \left(\frac{L_m^3 R_s}{L_s^2 w_\delta} + \frac{L_m R_r}{w_\delta} + \frac{L_m R_s}{L_s^2}\right)\Psi_{sx} i_{rx} - \frac{L_m^2 R_s}{L_s^2 w_\delta}\Psi_{sx}^2 + \\ &+ \frac{L_m R_s}{L_s} i_{rx} i_{sx} + \frac{1}{L_s}\left(\Psi_{sx}u_{sx} + \Psi_{sy}u_{sy}\right) + \frac{L_m^2}{L_s w_\delta}\Psi_{sx} u_{sx} \end{aligned} \tag{3.54}$$

From equations (3.49) and (3.50) final set of control variables can be calculated:

$$e_d = \frac{L_s w_\delta u_1 z_2 + L_s w_\delta u_2 z_4 + w_\delta u_2 z_{21}}{L_m L_s \Psi_{sx} z_4 - L_m L_s \Psi_{sy} z_2 + L_m \Psi_{sx} z_{21}} \tag{3.55}$$

$$\omega_{ir} = \frac{L_s \Psi_{sx} u_1 + L_s \Psi_{sy} u_1}{L_s \Psi_{sx} z_4 - L_s \Psi_{sy} z_2 + \Psi_{sx} z_{21}} \tag{3.56}$$

Diagram of the nonlinear control system for Doubly Fed Induction Generator supplied by Current Source Converter is shown in Figure 3.2.

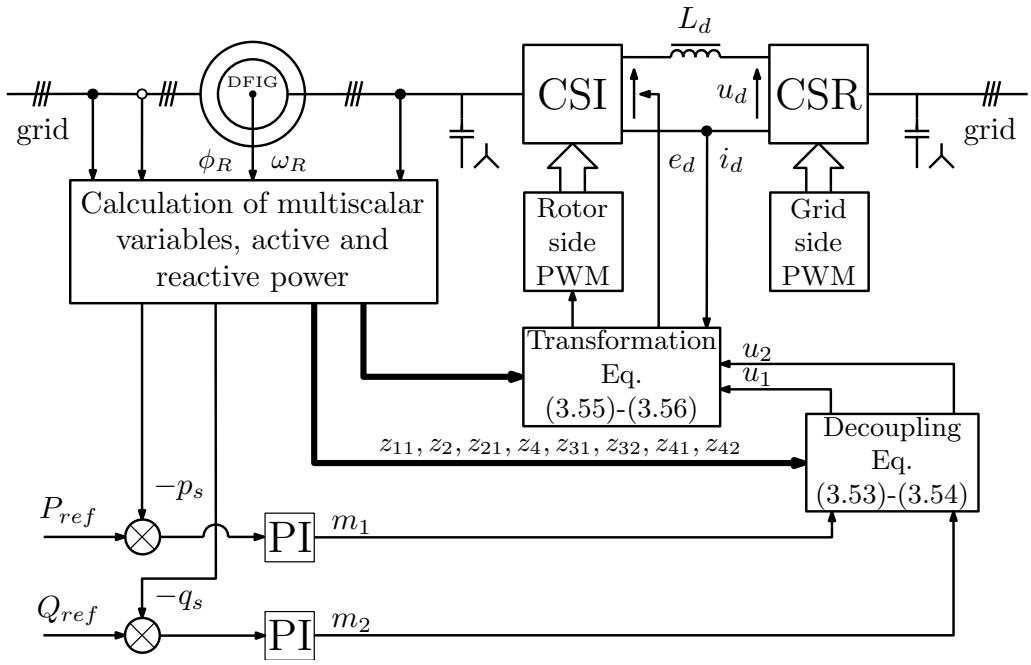

Figure 3.2: Multiscalar control structure 1 of the Doubly Fed Induction Generator

It is necessary to fulfil the condition that the denominators of equations (3.55) and (3.56) are not equal to 0, which may be difficult to achieve for certain conditions. By calculating the derivatives of (3.25) and (3.26) another form of differential equations is obtained, on the basis of which variables u_1 and u_2 can be defined using the Static State Feedback Law (3.53) – (3.54), and control variables e_d and ω_{ir} defined by equations (3.55) and (3.56). The control variables e_d and w_{ir} together with the Static State Feedback Law specified equations (3.51) and (3.52) allow for decoupling the control subsystems (active power from reactive power), which will be confirmed in simulation tests.

3.3 Multiscalar control structure 2

The difference in this approach is that the output filter capacitance is taken into consideration in the control structure. It will lead to further reduction of the oscillations in system and to correct the system responses during changes. Those assumptions allow to define $i_{fx} = M_i i_d$ and $i_{fy} = 0$. Where i_{fx}, i_{fy} are the inverter output current vectors and modulation index $M_i = 1$.

Making the above assumptions, equations (3.17) – (3.19) can be redefined as:

$$\frac{di_d}{d\tau} = \frac{1}{L_d}\left(e_d - R_d i_d - u_{rx}\right) \tag{3.57}$$

$$\frac{du_{cx}}{d\tau} = \frac{1}{C_m}\left(i_{fx} - i_{rx}\right) + \omega_{ir} u_{cy} \tag{3.58}$$

$$\frac{du_{cy}}{d\tau} = -\frac{1}{C_m} i_{ry} - \omega_{ir} u_{cx} \tag{3.59}$$

Under the condition that the amplitudes of i_d and u_c are invariant during the pulsing period, it is assumed that:

$$i_{fx} = |I_d| \cos(\phi_{ir}) \tag{3.60}$$

$$u_{cx} = |U_c| \cos(\phi_{ir}) \tag{3.61}$$

$$u_{cx} = |U_c| \sin(\phi_{ir}) \tag{3.62}$$

By differentiating the above equations, it is possible to determine the values of the derivatives during the pulse period:

$$\frac{di_{fx}}{d\tau} = -\omega_{ir} |I_d| \sin(\phi_{ir}) = -\omega_{ir} i_{fy} = 0 \tag{3.63}$$

$$\frac{du_{cx}}{d\tau} = -\omega_{ir} |U_c| \sin(\phi_{ir}) = -\omega_{ir} u_{cy} \tag{3.64}$$

$$\frac{du_{cy}}{d\tau} = \omega_{ir} |U_c| \cos(\phi_{ir}) = \omega_{ir} u_{cx} \tag{3.65}$$

By applying the relationships (3.63) – (3.65) to equations (3.57) – (3.59), the following set of variables can be obtained:

$$u_{rx} = e_d - R_d i_d \tag{3.66}$$

$$i_{rx} = i_d + 2\omega_{ir} u_{cy} C_m \tag{3.67}$$

$$i_{ry} = -2\omega_{ir} u_{cx} C_m \tag{3.68}$$

All of previously mentioned assumptions allow to develop mathematical relationships from which the control will be determined:

$$\frac{d\Psi_{sx}}{d\tau} = -\frac{R_s}{L_s}\Psi_{sx} + \frac{R_s L_m}{L_s} i_d + 2\frac{R_s L_m}{L_s}\omega_{ir} u_{cy} C_m + \omega_{ir}\Psi_{sy} + \omega_r \Psi_{sy} + u_{sx} \tag{3.69}$$

$$\frac{d\Psi_{sy}}{d\tau} = -\frac{R_s}{L_s}\Psi_{sy} - 2\frac{R_s L_m}{L_s}\omega_{ir} u_{cx} C_m - \omega_{ir}\Psi_{sx} - \omega_r \Psi_{sx} + u_{sy} \tag{3.70}$$

$$\begin{aligned}\frac{di_{rx}}{d\tau} =& -\left(\frac{L_s R_d}{w_\delta} + \frac{(L_m^2 R_s + L_s^2 R_r)}{L_s w_\delta}\right) i_d - \frac{L_m}{w_\delta} u_{sx} + \frac{L_m R_s}{L_s w_\delta}\Psi_{sx} - \frac{L_m}{w_\delta}\Psi_{sy}\omega_r + \\ & - 2C_m \omega_{ir}^2 u_{cx} - 2\frac{C_m (L_m^2 R_s + L_s^2 R_r)}{L_s w_\delta}\omega_{ir} u_{cy} + \frac{L_s}{w_\delta} e_d\end{aligned} \tag{3.71}$$

$$\begin{aligned}\frac{di_{ry}}{d\tau} =& \frac{L_m R_s}{L_s w_\delta}\Psi_{sy} + \frac{L_s}{w_\delta} u_{ry} + \frac{L_m}{w_\delta}\Psi_{sx}\omega_r - \frac{L_m}{w_\delta} u_{sy} + \\ & - 2C_m \omega_{ir}^2 u_{cy} + 2\frac{C_m (L_m^2 R_s + L_s^2 R_r)}{L_s w_\delta}\omega_{ir} u_{cx} - \omega_{ir} i_d\end{aligned} \tag{3.72}$$

$$\begin{aligned}\frac{di_{sx}}{d\tau} =& \left(\frac{L_m R_d}{w_\delta} + \frac{L_m^3 R_s}{L_s^2 w_\delta} + \frac{L_m R_r}{w_\delta} + \frac{L_m R_s}{L_s^2}\right) i_d + \left(\frac{L_m^2}{L_s w_\delta} + \frac{1}{L_s}\right)\Psi_{sy}\omega_r + \\ & + \left(2\frac{C_m L_m^3 R_s}{L_s^2 w_\delta} u_{cy} + 2\frac{C_m L_m R_r}{w_\delta} u_{cy} + 2\frac{C_m L_m}{L_s}\omega_{ir} u_{cx} + \frac{1}{L_s}\Psi_{sy} + \right. \\ & \left. + 2\frac{C_m L_m R_s}{L_s^2} u_{cy}\right)\omega_{ir} + \left(\frac{L_m^2}{L_s w_\delta} + \frac{1}{L_s}\right) u_{sx} - \left(\frac{L_m^2 R_s}{L_s^2 w_\delta} + \frac{R_s}{L_s^2}\right)\Psi_{sx} + \\ & - \frac{L_m}{w_\delta} e_d\end{aligned} \tag{3.73}$$

$$\begin{aligned}\frac{di_{sy}}{d\tau} =& \left(-2\frac{C_m L_m^3 R_s}{L_s^2 w_\delta} u_{cx} - 2\frac{C_m L_m R_r}{w_\delta} u_{cx} + 2\frac{C_m L_m}{L_s}\omega_{ir} u_{cy} + \right. \\ & \left. - 2\frac{C_m L_m R_s}{L_s^2} u_{cx} - \frac{1}{L_s}\Psi_{sx} + \frac{L_m}{L_s} i_d\right)\omega_{ir} - \left(\frac{L_m^2 R_s}{L_s^2 w_\delta} + \frac{R_s}{L_s^2}\right)\Psi_{sy} + \\ & - \left(\frac{L_m^2}{L_s w_\delta}\Psi_{sx} + \frac{1}{L_s}\Psi_{sx}\right)\omega_r + \left(\frac{1}{L_s} + \frac{L_m^2}{L_s w_\delta}\right) u_{sy} - \frac{L_m}{w_\delta} u_{ry}\end{aligned} \tag{3.74}$$

$$\frac{d\omega_r}{d\tau} = \frac{L_m}{J L_s}\left(\Psi_{sx} i_{ry} - \Psi_{sy} i_{rx}\right) - \frac{1}{J} m_0 \tag{3.75}$$

The proposed transformations of the generator state variables to multiscalar form:

$$z_{11} = \omega_r \tag{3.76}$$

$$z_2 = \Psi_{sy} i_{sx} - \Psi_{sx} i_{sy} \tag{3.77}$$

$$z_{21} = \Psi_{sx}^2 + \Psi_{sy}^2 \tag{3.78}$$

$$z_4 = -\Psi_{sx} i_{sx} - \Psi_{sy} i_{sy} \tag{3.79}$$

$$z_{31} = u_{cx}\Psi_{sy} - u_{cy}\Psi_{sx} \tag{3.80}$$

$$z_{32} = u_{cx}\Psi_{sx} + u_{cy}\Psi_{sy} \tag{3.81}$$

$$z_{41} = i_{fx} \approx i_d \tag{3.82}$$

$$z_{42} = i_{fy} \approx 0 \tag{3.83}$$

Considering the proposed multiscalar transformation (3.76) – (3.83), the dynamics of the system can be described by following set of the differential equations:

$$\frac{dz_{11}}{d\tau} = \frac{L_m}{JL_s}\left(\Psi_{sx} i_{ry} - \Psi_{sy} i_{rx}\right) - \frac{1}{J} m_0 \tag{3.84}$$

$$\begin{aligned}\frac{dz_2}{d\tau} =& -\frac{R_s}{L_s} z_2 + \left(\frac{z_{21}}{L_s} + z_4 + \frac{L_m^2}{L_s w_\delta} z_{21}\right) z_{11} + \frac{1}{L_s}\left(\Psi_{sy} u_{sx} - \Psi_{sx} u_{sy}\right) + q_s + \\ &+ \left(\frac{L_m R_s}{L_s^2}\Psi_{sy} - \frac{L_m R_s}{L_s} i_{sy} + \frac{L_m R_r}{w_\delta}\Psi_{sy} + \frac{L_m R_d}{w_\delta}\Psi_{sy} + \frac{L_m^3 R_s}{L_s^2 w_\delta}\Psi_{sy}\right) i_d + \\ &+ \frac{L_m^2}{L_s w_\delta}\left(\Psi_{sy} u_{sx} - \Psi_{sx} u_{sy}\right) + \frac{L_m}{w_\delta}\Psi_{sx} u_{ry} + u_1\end{aligned} \tag{3.85}$$

$$\begin{aligned}\frac{dz_{21}}{d\tau} =& -2\frac{R_s}{L_s} z_{21} + 4\frac{C_m L_m R_s}{L_s}\Psi_{sx}\omega_{ir} u_{cy} - 4\frac{C_m L_m R_s}{L_s}\Psi_{sy}\omega_{ir} u_{cx} + \\ &+ 2\frac{L_m R_s}{L_s}\Psi_{sx} i_d + 2\Psi_{sx} u_{sx} + 2\Psi_{sy} u_{sy}\end{aligned} \tag{3.86}$$

$$\begin{aligned}\frac{dz_4}{d\tau} =& -\frac{R_s}{L_s}z_4 - z_2 z_{11} - p_s - \frac{1}{L_s}\left(\Psi_{sx}u_{sx} + \Psi_{sy}u_{sy}\right) + \left(\frac{R_s}{L_s^2} + \frac{L_m^2 R_s}{L_s^2 w_\delta}\right) z_{21} + \\ &- \left(\frac{L_m^3 R_s}{L_s^2 w_\delta}\Psi_{sx} + \frac{L_m R_d}{w_\delta}\Psi_{sx} + \frac{L_m R_r}{w_\delta}\Psi_{sx} + \frac{L_m R_s}{L_s}i_{sx} + \frac{L_m R_s}{L_s^2}\Psi_{sx}\right) i_d + \\ &- \frac{L_m^2}{L_s w_\delta}z_{32} + \frac{L_m}{w_\delta}\Psi_{sy}u_{ry} + u_2\end{aligned} \tag{3.87}$$

$$\begin{aligned}\frac{dz_{31}}{d\tau} =& -\frac{R_s}{L_s}z_{31} - z_{11}z_{32} - 2\frac{C_m L_m R_s}{L_s}\omega_{ir}\left(u_{cx}^2 + u_{cy}^2\right) - \frac{L_m R_s}{L_s}i_d u_{cy} + \\ &+ u_{cx}u_{sy} - u_{cy}u_{sx} + \frac{1}{C_m}\left(\Psi_{sx}i_{ry} - \Psi_{sy}i_{rx} + \Psi_{sy}i_{fx}\right)\end{aligned} \tag{3.88}$$

$$\begin{aligned}\frac{dz_{32}}{d\tau} =& -\frac{R_s}{L_s}z_{32} - z_{11}z_{31} + \frac{L_m R_s}{L_s}i_d u_{cx} + u_{cx}u_{sx} + u_{cy}u_{sy} + \\ &+ \frac{1}{C_m}\left(\Psi_{sx}i_{fx} - \Psi_{sx}i_{rx} - \Psi_{sy}i_{ry}\right)\end{aligned} \tag{3.89}$$

$$\frac{dz_{41}}{d\tau} = \frac{1}{L_d}\left(e_d - R_d z_{41} - u_{rx}\right) \tag{3.90}$$

$$\frac{dz_{42}}{d\tau} = 0 \tag{3.91}$$

where:

$$\begin{aligned}u_1 =& \left[2\left(\frac{C_m L_m^3 R_s}{L_s^2 w_\delta} + \frac{C_m L_m R_r}{w_\delta} + \frac{C_m L_m R_s}{L_s^2}\right) z_{32} + 2\frac{C_m L_m}{L_s}\omega_{ir}z_{31} + \right. \\ &\left. -2\frac{C_m L_m R_s}{L_s}\left(i_{sx}u_{cx} + i_{sy}u_{cy}\right) + \frac{z_{21}}{L_s} + z_4 - \frac{L_m}{L_s}\Psi_{sx}i_d\right]\omega_{ir} - \frac{L_m}{w_\delta}\Psi_{sy}e_d\end{aligned} \tag{3.92}$$

$$\begin{aligned}u_2 =& \left[2\left(\frac{C_m L_m^3 R_s}{L_s^2 w_\delta} + \frac{C_m L_m R_r}{w_\delta} + \frac{C_m L_m R_s}{L_s^2}\right) z_{31} + 2\frac{C_m L_m R_r}{w_\delta}\Psi_{sy}u_{cx} \right. \\ &\left. -2\frac{C_m L_m R_s}{L_s}\left(i_{sx}u_{cy} - i_{sy}u_{cx}\right) - 2\frac{C_m L_m}{L_s}z_{32}\omega_{ir} - \frac{L_m}{L_s}i_d\Psi_{sy} - z_2\right]\omega_{ir} + \\ &+ \frac{L_m}{w_\delta}\Psi_{sx}e_d\end{aligned} \tag{3.93}$$

As can be seen, control variables occur only in equations (3.85) and (3.87). Equations (3.88) and (3.89) describe dynamics of the output filter. Equations (3.90) and (3.91) describe dynamics of the DC-link. Applying Static State Feedback Law to differential equations (3.85) and (3.87) the following form of equations can be obtained:

$$\frac{dz_2}{d\tau} = \frac{1}{T}\left(-z_2 + m_1\right) \qquad \frac{dz_4}{d\tau} = \frac{1}{T}\left(-z_4 + m_2\right)$$

where:

$$\begin{aligned} m_1 =& T\left[u_1 + \left(\frac{z_{21}}{L_s} + z_4 + \frac{L_m^2}{L_s w_\delta} z_{21}\right) z_{11} + \frac{1}{L_s}\left(\Psi_{sy} u_{sx} - \Psi_{sx} u_{sy}\right) + q_s + \right. \\ &+ \left(\frac{L_m R_s}{L_s^2}\Psi_{sy} - \frac{L_m R_s}{L_s} i_{sy} + \frac{L_m R_r}{w_\delta}\Psi_{sy} + \frac{L_m R_d}{w_\delta}\Psi_{sy} + \frac{L_m^3 R_s}{L_s^2 w_\delta}\Psi_{sy}\right) i_d + \\ &\left. + \frac{L_m^2}{L_s w_\delta}\left(\Psi_{sy} u_{sx} - \Psi_{sx} u_{sy}\right) + \frac{L_m}{w_\delta}\Psi_{sx} u_{ry}\right] \end{aligned} \tag{3.94}$$

$$\begin{aligned} m_2 =& T\left[u_2 - z_2 z_{11} - p_s - \frac{1}{L_s}\left(\Psi_{sx} u_{sx} + \Psi_{sy} u_{sy}\right) + \left(\frac{R_s}{L_s^2} + \frac{L_m^2 R_s}{L_s^2 w_\delta}\right) z_{21} + \right. \\ &- \left(\frac{L_m^3 R_s}{L_s^2 w_\delta}\Psi_{sx} + \frac{L_m R_d}{w_\delta}\Psi_{sx} + \frac{L_m R_r}{w_\delta}\Psi_{sx} + \frac{L_m R_s}{L_s} i_{sx} + \frac{L_m R_s}{L_s^2}\Psi_{sx}\right) i_d + \\ &\left. - \frac{L_m^2}{L_s w_\delta} z_{32} + \frac{L_m}{w_\delta}\Psi_{sy} u_{ry}\right] \end{aligned} \tag{3.95}$$

Obtained variables m_1 and m_2 are new controls and take form showed in (3.94) and (3.95), respectively. Variables u_1 and u_2 present in (3.85) and (3.87) are used to compensate the coupling between new state variables in the presented system:

$$\begin{aligned} u_1 =& \frac{1}{T} m_1 - \left(\frac{z_{21}}{L_s} + z_4 + \frac{L_m^2}{L_s w_\delta} z_{21}\right) z_{11} - \frac{1}{L_s}\left(\Psi_{sy} u_{sx} - \Psi_{sx} u_{sy}\right) - q_s + \\ &- \left(\frac{L_m R_s}{L_s^2}\Psi_{sy} - \frac{L_m R_s}{L_s} i_{sy} + \frac{L_m R_r}{w_\delta}\Psi_{sy} + \frac{L_m R_d}{w_\delta}\Psi_{sy} + \frac{L_m^3 R_s}{L_s^2 w_\delta}\Psi_{sy}\right) i_d + \\ &- \frac{L_m^2}{L_s w_\delta}\left(\Psi_{sy} u_{sx} - \Psi_{sx} u_{sy}\right) - \frac{L_m}{w_\delta}\Psi_{sx} u_{ry} \end{aligned} \tag{3.96}$$

$$\begin{aligned} u_2 =& \frac{1}{T} m_2 + z_2 z_{11} + p_s + \frac{1}{L_s}\left(\Psi_{sx} u_{sx} + \Psi_{sy} u_{sy}\right) - \left(\frac{R_s}{L_s^2} + \frac{L_m^2 R_s}{L_s^2 w_\delta}\right) z_{21} + \\ &+ \left(\frac{L_m^3 R_s}{L_s^2 w_\delta}\Psi_{sx} + \frac{L_m R_d}{w_\delta}\Psi_{sx} + \frac{L_m R_r}{w_\delta}\Psi_{sx} + \frac{L_m R_s}{L_s} i_{sx} + \frac{L_m R_s}{L_s^2}\Psi_{sx}\right) i_d + \\ &+ \frac{L_m^2}{L_s w_\delta} z_{32} - \frac{L_m}{w_\delta}\Psi_{sy} u_{ry} \end{aligned} \tag{3.97}$$

From equations (3.92) and (3.93) final set of control variables can be calculated:

$$e_d = \frac{B_{\omega 1} w_\delta u_2 - B_{\omega 2} w_\delta u_1}{B_{\omega 1} L_m \Psi_{sx} + B_{\omega 2} L_m \Psi_{sy}} \tag{3.98}$$

$$\omega_{ir} = \frac{\Psi_{sx} u_1 + \Psi_{sy} u_2}{B_{\omega 1}\Psi_{sx} + B_{\omega 2}\Psi_{sy}} \tag{3.99}$$

where:

$$B_{\omega 1} = \left[2 \left(\frac{C_m L_m^3 R_s}{L_s^2 w_\delta} + \frac{C_m L_m R_r}{w_\delta} + \frac{C_m L_m R_s}{L_s^2} \right) z_{32} + 2 \frac{C_m L_m}{L_s} \omega_{ir} z_{31} + \right. \\ \left. -2 \frac{C_m L_m R_s}{L_s} \left(i_{sx} u_{cx} + i_{sy} u_{cy} \right) + \frac{z_{21}}{L_s} + z_4 - \frac{L_m}{L_s} \Psi_{sx} i_d \right] \tag{3.100}$$

$$B_{\omega 2} = \left[2 \left(\frac{C_m L_m^3 R_s}{L_s^2 w_\delta} + \frac{C_m L_m R_r}{w_\delta} + \frac{C_m L_m R_s}{L_s^2} \right) z_{31} + 2 \frac{C_m L_m R_r}{w_\delta} \Psi_{sy} u_{cx} \right. \\ \left. -2 \frac{C_m L_m R_s}{L_s} \left(i_{sx} u_{cy} - i_{sy} u_{cx} \right) - 2 \frac{C_m L_m}{L_s} z_{32} \omega_{ir} - \frac{L_m}{L_s} i_d \Psi_{sy} - z_2 \right] \tag{3.101}$$

It is necessary to fulfil the condition that the denominators of equations 3.98 and 3.99 are not equal to 0, which may be difficult to achieve for certain conditions. Due to the high processor computing power required to calculate the final control variables, this method was only analysed the theoretical and simulation studies presented in the Sections 4.1-4.4.

Calculation of the derivatives of (3.85) and (3.87) will lead to yet another set of differential equations. On their basis variables u_1 and u_2 can be defined using the Static State Feedback Law, and also the control variables e_d and ω_{ir} defined by equations (3.98) and (3.99). The control variables e_d and w_{ir} paired with the Static State Feedback Law specified equations (3.94) and (3.95) will allow for decoupling of the control subsystems (active power from reactive power) and further reduction of the low frequency oscillations of the controlled variables. That statement will be tested and confirmed in simulation tests.

Diagram of the control system for Doubly Fed Induction Generator supplied by Current Source Converter is shown in Figure 3.3.

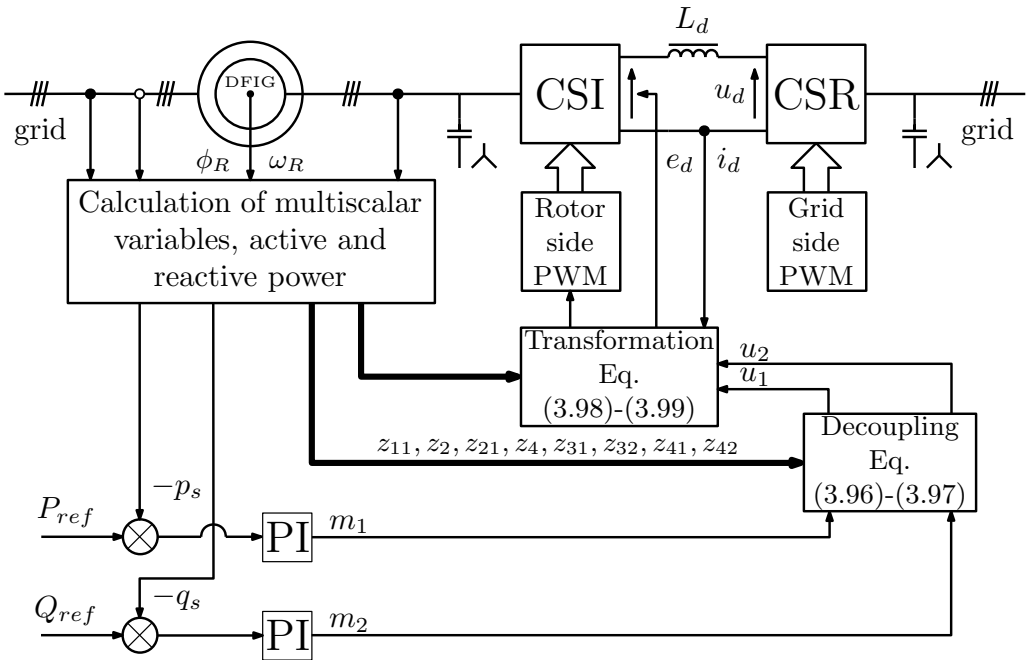

Figure 3.3: Multiscalar control structure 2 of the Doubly Fed Induction Generator

3.4 Multiscalar control structure 3

The control structure proposed in this chapter is significantly simplified compared to those presented in Sections 3.2 - 3.3 due to the form of control variables and calculation time. However, it is necessary to use a cascaded structure of PI controllers (2 PI controllers each in the control subpaths) to ensure an adequate control process.

Assuming that the control variables are the DC-link input voltage e_d and angular speed of output current ω_{ir}, it is possible to maintain the reference values of powers. This approach grants controllability of DC-link current and gives better use of grid power.

The rotor speed and square of stator flux vector components are not directly controlled in the Doubly-Fed Induction Generator (DFIG). Control system aims to stabilize the active and reactive powers. Therefore, the generic input-output transformation is not suitable for power control of DFIG with the CSC. The rank of the examined system is $r = 8$, [75]. The transformation should be extended to the CSC equations. As assumed in Section 2.2 the rotor side Current Source Converter is considered as the ideal commutator working with a constant modulation index $M_i = 1$. In case of this method x-y coordinate system is tied to x component of the

rotor current: $i_{rx} = M_i i_d$ and $i_{ry} = 0$. Assuming a very small output capacitance it can be assumed that $u_{rx} = M_i e_d$

Under this assumption new set of relationships from which the control will be derived can be constructed:

$$\frac{d\Psi_{sx}}{d\tau} = -\frac{R_s}{L_s}\Psi_{sx} + \frac{L_m R_s}{L_s} i_{rx} + \Psi_{sy}\omega_{ir} + u_{sx} \tag{3.102}$$

$$\frac{d\Psi_{sy}}{d\tau} = -\frac{R_s}{L_s}\Psi_{sy} - \Psi_{sx}\omega_{ir} + u_{sy} \tag{3.103}$$

$$\begin{aligned}\frac{di_{rx}}{d\tau} = &-\frac{(L_m^2 R_s + L_s^2 R_r)}{L_s w_\delta} i_{rx} - \frac{L_m}{w_\delta}\Psi_{sy}\omega_r - \frac{L_m}{w_\delta} u_{sx} + \frac{L_m R_s}{L_s w_\delta}\Psi_{sx} + \\ &+ \frac{L_s}{w_\delta} u_{rx}\end{aligned} \tag{3.104}$$

$$\frac{d\omega_r}{d\tau} = -\frac{L_m}{J L_s}\Psi_{sy} i_{rx} - \frac{1}{J} m_0 \tag{3.105}$$

The proposed transformations of the generator state variables to multiscalar form:

$$z_{11} = \omega_r \tag{3.106}$$

$$z_{12} = -\Psi_{sy} i_{rx} \tag{3.107}$$

$$z_{21} = \Psi_{sx}^2 + \Psi_{sy}^2 \tag{3.108}$$

$$z_{22} = \Psi_{sx} i_{rx} \tag{3.109}$$

$$z_{31} = u_{cx}\Psi_{sy} - u_{cy}\Psi_{sx} \tag{3.110}$$

$$z_{32} = u_{cx}\Psi_{sx} + u_{cy}\Psi_{sy} \tag{3.111}$$

$$z_{41} = i_{fx} \approx i_{rx} \tag{3.112}$$

$$z_{42} = i_{fy} \approx 0 \tag{3.113}$$

Considering equations (3.107) and (3.109) for the steady state, the active and reactive powers have the following form, [60]:

$$p_s = -\frac{L_m}{L_s} z_{12} \tag{3.114}$$

$$q_s = \frac{1}{L_s} - \frac{L_m}{L_s} z_{22} \tag{3.115}$$

Considering the proposed multiscalar transformation (3.106) – (3.113), the dynamics of the system can be described by following set of the differential equations:

$$\frac{dz_{11}}{d\tau} = \frac{L_m}{JL_s} z_{12} - \frac{1}{J} m_0 \tag{3.116}$$

$$\begin{aligned}\frac{dz_{12}}{d\tau} =& -\left(\frac{R_s}{L_s} + \frac{L_m^2 R_s}{L_s w_\delta} + \frac{L_s R_r}{w_\delta}\right) z_{12} + \frac{L_m}{w_\delta}\Psi_{sy} u_{sx} + \frac{L_m}{w_\delta}\Psi_{sy}^2 z_{11} + \\ & - \frac{L_m R_s}{L_s w_\delta}\Psi_{sx}\Psi_{sy} - i_{rx} u_{sy} + u_1\end{aligned} \tag{3.117}$$

$$\frac{dz_{21}}{d\tau} = -2\left(\frac{R_s}{L_s} z_{21} - \frac{L_m R_s}{L_s}\Psi_{sx} i_{rx} - (\Psi_{sx} u_{sx} + \Psi_{sy} u_{sy})\right) \tag{3.118}$$

$$\begin{aligned}\frac{dz_{22}}{d\tau} =& -\left(\frac{R_s}{L_s} + \frac{L_m^2 R_s}{L_s w_\delta} + \frac{L_s R_r}{w_\delta}\right) z_{22} - \frac{L_m}{w_\delta}\Psi_{sx} u_{sx} - \frac{L_m}{w_\delta}\Psi_{sx}\Psi_{sy} z_{11} + \\ & + \frac{L_m R_s}{L_s w_\delta}\Psi_{sx}^2 + \frac{L_m R_s}{L_s} i_{rx}^2 + i_{rx} u_{sx} + u_2\end{aligned} \tag{3.119}$$

$$\begin{aligned}\frac{dz_{31}}{d\tau} =& -\frac{R_s}{L_s} z_{31} - \frac{L_m R_s}{L_s} i_{rx} u_{cy} + u_{cx} u_{sy} - u_{cy} u_{sx} + \\ & + \frac{1}{C_m}\left(\Psi_{sx} i_{ry} - \Psi_{sy} i_{rx} + \Psi_{sy} i_{fx} - \Psi_{sx} i_{fy}\right)\end{aligned} \tag{3.120}$$

$$\begin{aligned}\frac{dz_{32}}{d\tau} =& -\frac{R_s}{L_s} z_{32} + \frac{L_m R_s}{L_s} i_{rx} u_{cx} + u_{cx} u_{sx} + u_{cy} u_{sy} \\ & + \frac{1}{C_m}\left(\Psi_{sx} i_{fx} + \Psi_{sy} i_{fy} - \Psi_{sx} i_{rx} - i_{ry}\right)\end{aligned} \tag{3.121}$$

$$\frac{dz_{41}}{d\tau} = \frac{1}{L_d}\left(e_d - R_d z_{41} - u_{rx}\right) \tag{3.122}$$

$$\frac{dz_{42}}{d\tau} = 0 \tag{3.123}$$

where:

$$u_1 = z_{22}\omega_{ir} - \frac{L_s}{w_\delta}\Psi_{sy} u_{rx} \tag{3.124}$$

$$u_2 = -z_{12}\omega_{ir} + \frac{L_s}{w_\delta}\Psi_{sx} u_{rx} \tag{3.125}$$

As can be seen only equations (3.117) and (3.119) have variables that in

this method are responsible for controlling active and reactive power. Equations (3.120) and (3.121) describe dynamics of the output filter. Equations (3.122) and (3.123) describe dynamics of the DC-link. Applying Static State Feedback Law to differential equations (3.117) and (3.119) the following form of equations can be obtained:

$$\frac{dz_{12}}{d\tau} = \frac{1}{T}\left(-z_{12} + m_1\right) \qquad \frac{dz_{22}}{d\tau} = \frac{1}{T}\left(-z_{22} + m_2\right)$$

where:

$$m_1 = T\left[u_1 + \frac{L_m}{w_\delta}\Psi_{sy}u_{sx} + \frac{L_m}{w_\delta}\Psi_{sy}^2 z_{11} - \frac{L_m R_s}{L_s w_\delta}\Psi_{sx}\Psi_{sy} - i_{rx}u_{sy}\right] \tag{3.126}$$

$$m_2 = T\left[u_2 - \frac{L_m}{w_\delta}\Psi_{sx}u_{sx} - \frac{L_m}{w_\delta}\Psi_{sx}\Psi_{sy}z_{11} + \frac{L_m R_s}{L_s w_\delta}\Psi_{sx}^2 + \frac{L_m R_s}{L_s}i_{rx}^2 + i_{rx}u_{sx}\right] \tag{3.127}$$

Obtained variables m_1 and m_2 are new controls and take form depicted in (3.126) and (3.127), respectively. Variables u_1 and u_2 present in (3.117) and (3.119) are used to compensate the coupling between new state variables in the presented system:

$$u_1 = \frac{1}{T}m_1 - \frac{L_m}{w_\delta}\Psi_{sy}u_{sx} - \frac{L_m}{w_\delta}\Psi_{sy}^2 z_{11} + \frac{L_m R_s}{L_s w_\delta}\Psi_{sx}\Psi_{sy} + i_{rx}u_{sy} \tag{3.128}$$

$$u_2 = \frac{1}{T}m_2 + \frac{L_m}{w_\delta}\Psi_{sx}u_{sx} + \frac{L_m}{w_\delta}\Psi_{sx}\Psi_{sy}z_{11} - \frac{L_m R_s}{L_s w_\delta}\Psi_{sx}^2 - \frac{L_m R_s}{L_s}i_{rx}^2 - i_{rx}u_{sx} \tag{3.129}$$

From equations (3.124) and (3.125) final set of control variables can be calculated:

$$e_d = \frac{w_\delta u_1 z_{12} + w_\delta u_2 z_{22}}{L_m\Psi_{sx}z_{22} - L_m\Psi_{sy}z_{12}} \tag{3.130}$$

$$\omega_{ir} = \frac{\Psi_{sx}u_1 + \Psi_{sy}u_2}{\Psi_{sx}z_{22} - \Psi_{sy}z_{12}} \tag{3.131}$$

Calculation of the derivatives of (3.117) and (3.119) will lead to yet another set of differential equations. On their basis variables u_1 and u_2 can be defined using the Static State Feedback Law, and also the control variables e_d and ω_{ir} defined by equations (3.130) and (3.131). The control variables e_d and w_{ir} paired with the Static State Feedback Law specified equations (3.126) and (3.127) will allow for decoupling the control subsystems (active power from reactive power) and further reduction of the low frequency oscillations of the controlled variables as well as simplification of

decoupling functions. That statement will be tested and confirmed in simulation and experimental tests.

Diagram of the control system is shown in Figure 3.4.

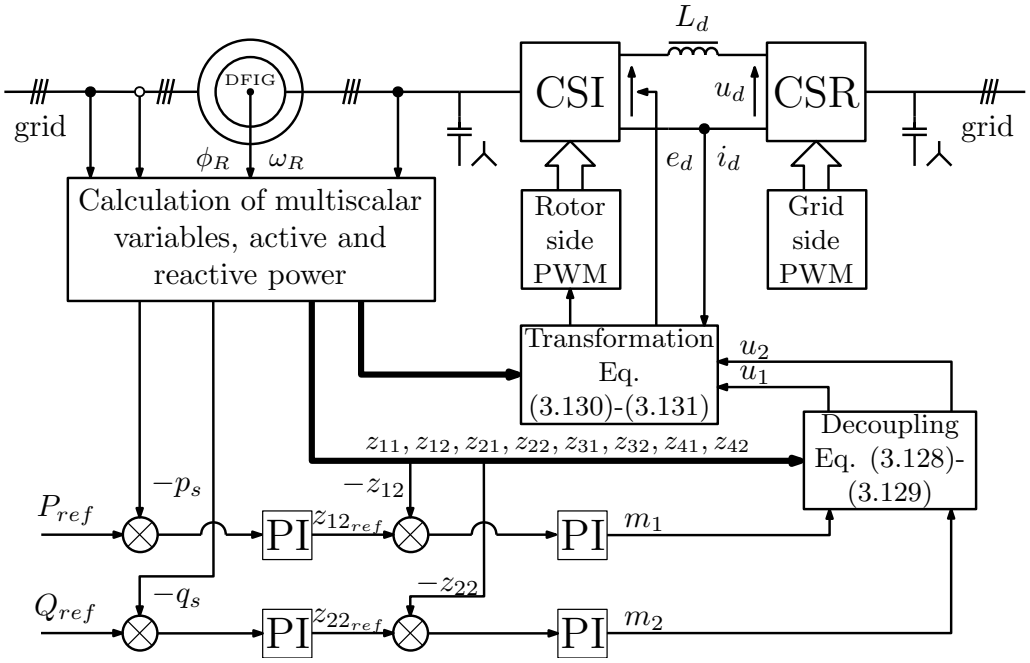

Figure 3.4: Multiscalar control structure 3 of the Doubly Fed Induction Generator

3.5 Multiscalar control structure 4

The structure presented in this chapter is based on the reference system associated with the inverter output current vector. Under the assumption of unitary modulation coefficient, this results in a significant simplification of the relationships determining the control variables, while maintaining similar control characteristics.

The assumption that the control variables are the DC-link input voltage e_d and angular speed of output current ω_{ir} can be also made here. The difference is that in this approach output filter capacitance is taken into consideration in the control structure. Those assumptions allow to define $i_{fx} = M_i i_d$ and $i_{fy} = 0$. Where i_{fx}, i_{fy} are the inverter output current vectors and modulation index $M_i = 1$.

Under this condition the DC-link current equation (3.17) can be also used to

describe the behaviour of x component of inverter output current:

$$\frac{di_{fx}}{d\tau} = \frac{1}{L_d}\left(e_d - R_d i_{fx} - u_{rx}\right) \tag{3.132}$$

Following all of the above assumptions, a new set of relationships from which the control will be derived can be constructed:

$$\frac{d\psi_{sx}}{d\tau} = -\frac{R_s}{L_s}\Psi_{sx} + \frac{R_s L_m}{L_s} i_{rx} + \omega_{if}\Psi_{sy} + u_{sx} \tag{3.133}$$

$$\frac{d\Psi_{sy}}{d\tau} = -\frac{R_s}{L_s}\Psi_{sy} + \frac{R_s L_m}{L_s} i_{ry} - \omega_{if}\Psi_{sx} + u_{sy} \tag{3.134}$$

$$\begin{aligned}\frac{di_{rx}}{d\tau} =& -\frac{L_s^2 R_r + L_m^2 R_s}{L_s w_\delta} i_{rx} + \frac{R_s L_m}{L_s w_\delta}\Psi_{sx} + \left(\omega_{if} - \omega_r\right) i_{ry} + \\ & - \frac{L_m}{w_\delta}\omega_r \Psi_{sy} + \frac{L_s}{w_\delta} u_{rx} - \frac{L_m}{w_\delta} u_{sx}\end{aligned} \tag{3.135}$$

$$\begin{aligned}\frac{di_{ry}}{d\tau} =& -\frac{L_s^2 R_r + L_m^2 R_s}{L_s w_\delta} i_{ry} + \frac{R_s L_m}{L_s w_\delta}\Psi_{sy} - \left(\omega_{if} - \omega_r\right) i_{rx} + \\ & + \frac{L_m}{w_\delta}\omega_r \Psi_{sx} + \frac{L_s}{w_\delta} u_{ry} - \frac{L_m}{w_\delta} u_{sy}\end{aligned} \tag{3.136}$$

$$\frac{d\omega_r}{d\tau} = \frac{L_m}{J L_s}\left(\Psi_{sx} i_{ry} - \Psi_{sy} i_{rx}\right) - \frac{1}{J} m_0 \tag{3.137}$$

The proposed transformations of the generator state variables to multiscalar form:

$$z_{11} = \omega_r \tag{3.138}$$

$$z_{12} = -\Psi_{sy} z_{41} \tag{3.139}$$

$$z_{21} = \Psi_{sx}^2 + \Psi_{sy}^2 \tag{3.140}$$

$$z_{22} = \Psi_{sx} z_{41} \tag{3.141}$$

$$z_{31} = u_{cx}\Psi_{sy} - u_{cy}\Psi_{sx} \tag{3.142}$$

$$z_{32} = u_{cx}\Psi_{sx} + u_{cy}\Psi_{sy} \tag{3.143}$$

$$z_{41} = i_{fx} \approx i_d \tag{3.144}$$

$$z_{42} = i_{fy} \approx 0 \tag{3.145}$$

Considering the proposed multiscalar transformation (3.138) – (3.145), the dynamics of the system can be described by following set of the differential equations:

$$\frac{dz_{11}}{d\tau} = \frac{L_m}{JL_s}\left(\Psi_{sx} i_{ry} - \Psi_{sy} i_{rx}\right) - \frac{1}{J} m_0 \tag{3.146}$$

$$\frac{dz_{12}}{d\tau} = -\left(\frac{R_s}{L_s} + \frac{R_d}{L_d}\right) z_{21} - \left(\frac{L_m R_s}{L_s} i_{ry} + u_{sy}\right) z_{41} + \frac{1}{L_d}\Psi_{sy} u_{rx} + u_1 \tag{3.147}$$

$$\frac{dz_{21}}{d\tau} = -2\left(\frac{R_s}{L_s} z_{21} - \frac{L_m R_s}{L_s}\left(\Psi_{sx} i_{rx} + \Psi_{sy} i_{ry}\right) - \left(\Psi_{sx} u_{sx} + \Psi_{sy} u_{sy}\right)\right) \tag{3.148}$$

$$\frac{dz_{22}}{d\tau} = -\left(\frac{R_s}{L_s} + \frac{R_d}{L_d}\right) z_{22} + \left(\frac{L_m R_s}{L_s} i_{rx} + u_{sx}\right) z_{41} - \frac{1}{L_d}\Psi_{sx} u_{rx} + u_2 \tag{3.149}$$

$$\begin{aligned}\frac{dz_{31}}{d\tau} = &-\frac{R_s}{L_s} z_{31} - \frac{L_m R_s}{L_s}\left(i_{rx} u_{cy} - i_{ry} u_{cx}\right) + u_{cx} u_{sy} - u_{cy} u_{sx} + \\ &+ \frac{1}{C_m}\left(\Psi_{sx} i_{ry} + \Psi_{sy} z_{41} - \Psi_{sy} i_{rx}\right)\end{aligned} \tag{3.150}$$

$$\begin{aligned}\frac{dz_{32}}{d\tau} = &-\frac{R_s}{L_s} z_{32} + \frac{L_m R_s}{L_s}\left(i_{rx} u_{cx} + i_{ry} u_{cy}\right) + u_{cx} u_{sx} + u_{cy} u_{sy} + \\ &+ \frac{1}{C_m}\left(\Psi_{sx} z_{41} - \Psi_{sx} i_{rx} - \Psi_{sy} i_{ry}\right)\end{aligned} \tag{3.151}$$

$$\frac{dz_{41}}{d\tau} = \frac{1}{L_d}\left(e_d - R_d z_{41} - u_{rx}\right) \tag{3.152}$$

$$\frac{dz_{42}}{d\tau} = 0 \tag{3.153}$$

where:

$$u_1 = z_{22}\omega_{if} - \frac{1}{L_d}\Psi_{sy} e_d \tag{3.154}$$

$$u_2 = -z_{12}\omega_{if} + \frac{1}{L_d}\Psi_{sx} e_d \tag{3.155}$$

As can be seen, only equations (3.147) and (3.149) have variables that in this method are responsible for controlling active and reactive power. Equations (3.150) and (3.151) describe dynamics of the output filter. Equations (3.152) and (3.153) describe dynamics of the DC-link. Applying Static State Feedback Law to differential equations (3.147) and (3.149) the following form of equations can be

obtained:

$$\frac{dz_{12}}{d\tau} = \frac{1}{T}\left(-z_{12} + m_1\right) \qquad \frac{dz_{22}}{d\tau} = \frac{1}{T}\left(-z_{22} + m_2\right)$$

where:

$$m_1 = T\left[u_1 - \left(\frac{L_m R_s}{L_s} i_{ry} + u_{sy}\right) i_{fx} + \frac{1}{L_d}\Psi_{sy} u_{rx}\right] \tag{3.156}$$

$$m_2 = T\left[u_2 + \left(\frac{L_m R_s}{L_s} i_{rx} + u_{sx}\right) i_{fx} - \frac{1}{L_d}\Psi_{sx} u_{rx}\right] \tag{3.157}$$

Obtained variables m_1 and m_2 are new controls and take form showed in (3.156) and (3.157), respectively. Variables u_1 and u_2 present in (3.147) and (3.149) are used to compensate the coupling between new state variables in the presented system:

$$u_1 = \frac{1}{T} m_1 + \left(\frac{L_m R_s}{L_s} i_{ry} + u_{sy}\right) i_{fx} - \frac{1}{L_d}\Psi_{sy} u_{rx} \tag{3.158}$$

$$u_2 = \frac{1}{T} m_2 - \left(\frac{L_m R_s}{L_s} i_{rx} + u_{sx}\right) i_{fx} + \frac{1}{L_d}\Psi_{sx} u_{rx} \tag{3.159}$$

From equations (3.154) and (3.155) final set of control variables can be calculated:

$$e_d = \frac{L_d u_1 z_{12} + L_d u_2 z_{22}}{\Psi_{sx} z_{22} - \Psi_{sy} z_{12}} \tag{3.160}$$

$$\omega_i = \frac{\Psi_{sx} u_1 + \Psi_{sy} u_2}{\Psi_{sx} z_{22} - \Psi_{sy} z_{12}} \tag{3.161}$$

Calculation of the derivatives of (3.147) and (3.149) will lead to yet another set of differential equations. On their basis variables u_1 and u_2 can be defined using the Static State Feedback Law, and also the control variables e_d and ω_{ir} defined by equations (3.160) and (3.161). The control variables e_d and w_{ir} paired with the Static State Feedback Law specified equations (3.156) and (3.157) will allow for decoupling the control subsystems (active power from reactive power) and further reduction of the low frequency oscillations of the controlled variables as well as simplification of decoupling functions. That statement will be tested and confirmed in simulation and experimental tests.

Diagram of the control system is shown in Figure 3.5.

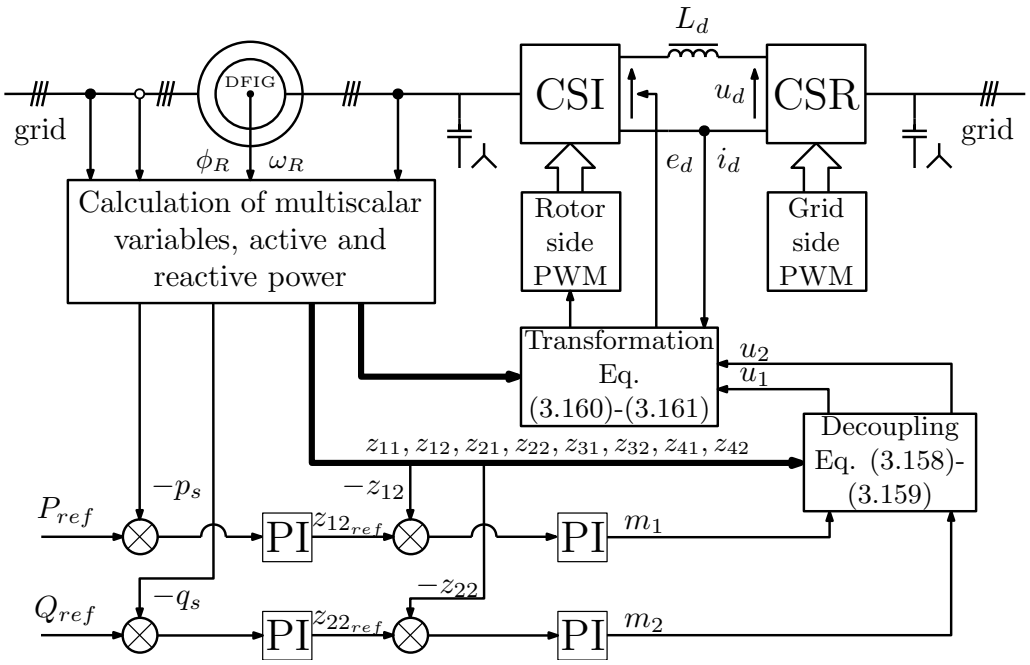

Figure 3.5: Multiscalar control structure 4 of the Doubly Fed Induction Generator

3.6 Stability of linearized control system using multiscalar transformation

The challenge of control synthesis includes the selection of the structure of the control system as well as determining the type and parameters of the controller, [83–91]. This involves:

- the mathematical model of the control object obtained as a result of identification;
- the task of the control system and indicators of control quality;
- the nature of disturbances that may act on the system (measurable, random);
- constraints on the forcing signals.

In practice, various simplifications are introduced in both the mathematical models of objects and the formulation of regulation quality indicators and regulator structures. The synthesis task is to determine the equation of the optimal regulator that best meets the adopted regulation quality criteria. Thus, an important point is the adaption of a regulation quality criteria. They can be divided into several groups, [90, 91]:

- related to the evaluation of step characteristic parameters;

- related to the evaluation of parameters of frequency characteristics;
- concerning the distribution of zeros and poles of the transmittance of a closed system;
- integral.

The selection of a specific criterion is typically influenced by factors such as the nature of the control task, computational complexity, measurement capabilities, etc. It is determined by the problem under consideration - a large number of different criteria makes it possible to choose the evaluation most suitable for the synthesis of a specific control system.

It is essential to note that the listed dynamic quality criteria are associated with achieving the desired static accuracy of the regulation. The role of the regulator is to ensure the desired behaviour of a specific output signal from the object by processing the feedback signal and the reference signal (most often their difference) and producing a control signal for the object. From the point of view of dynamics, the controller can be regarded as an element shaping the dynamic properties of a closed system.

Most of industrial applications use Proportional Integral Derivative (PID) controllers. The operation of an ideal PID controller is described by following differential equation:

$$u(t) = K_p \left[e(t) + \frac{1}{T_i} \int_0^t e dt + T_d \frac{de}{d\tau} \right] \tag{3.162}$$

The parameters K_p , T_i , T_d are to be considered adjustable in a given controller. These constant can be described as:

- K_p – amplification factor;
- T_i – doubling time - the time it takes for a step signal given to the input of a PI controller for the output signal of the controller to double its value with respect to the initial step caused by proportional action;
- T_d – advance time - the time after which, if a linearly increasing signal is applied to the input of the Proportional Derivative (PD) controller, the signal associated with the proportional action will equal the signal from the differential action.

The dynamic criteria for control systems frequently revolve around the requirement for a particular waveform of the error signal when subjected to step

inputs. Two components can be distinguished in the error signal: steady state error e_u i dynamic state error $e_p(t)$.

The most common indicators used to describe the performance of a control system are:

- t_r – regulation time - the time that elapses from the moment the disturbance is fed into the system until the transient component of the error signal decreases permanently below the assumed value of Δe;
- t_u – ramp-up time - the time required for the step characteristics to reach from 10% to 90% of the set value, determines the speed of operation of the control system;
- M_p – over-regulation - the ratio of the maximum step response value to the steady state value, is a measure of the stability of a closed system;
- e_s – steady state error - the value of the error signal $e(t)$ that persists in the system once the transient processes have disappeared.

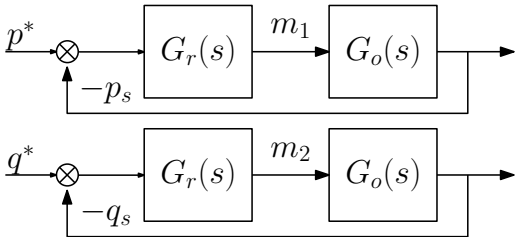

Figure 3.6: Diagram of regulation loops for multiscalar structures 1 and 2

As shown in Figure 3.6, every control structure can be simplified to the one regulator one process loop. The simplification can be made due to low influence of the internal PI controller loops in steady state. The goal of optimizing the control system is to minimize transient states time and reduce overshoot to the lowest extent possible. For Stability Control Analysis author decided to base on the Bode plot and Pole-zero map for regulation loops.

Derivative equation of the stator active power (as in Section 3.2):

$$\frac{dp_s}{d\tau} = \frac{1}{T}\left(-p_s + m_1\right) \tag{3.163}$$

Time constant of the object $\frac{1}{T}$ can be defined as:

$$\frac{1}{T} = T_i = \frac{R_s}{L_s} + \frac{R_d}{L_d} + \frac{R_c}{L_d} \tag{3.164}$$

Values of the machine parameters are detailed in Table A.1.

Equation (3.163) can be described by following transfer function:

$$G_o(s) = \frac{1}{sT + 1} \tag{3.165}$$

where:

$$T = \frac{L_s L_d}{R_s L_d + L_s R_d + R_c}$$

Regulator transfer function is as follows:

$$G_r(s) = k_p + \frac{k_i}{s} \tag{3.166}$$

Multiplying both equations will result in the transfer function of the analysed object:

$$G_{l1}(s) = \left(k_p + \frac{k_i}{s}\right)\left(\frac{1}{sT + 1}\right) \tag{3.167}$$

Closed-loop system transfer functions can be approximated as:

$$G(s) = \frac{G_{l1}(s)}{1 + G_{l1}(s)} \tag{3.168}$$

Considering equations (3.165) and (3.166) $G(s)$ will take the following form:

$$G(s) = \frac{G_{l1}(s)}{1 + G_{l1}(s)} = \frac{\left(k_p + \frac{k_i}{s}\right)\left(\frac{1}{sT+1}\right)}{1 + \left(k_p + \frac{k_i}{s}\right)\left(\frac{1}{sT+1}\right)} \tag{3.169}$$

and can be further simplified to:

$$G(s) = \frac{k_p s + k_i}{s^2 T + (k_p + 1)\, s + k_i} \tag{3.170}$$

Considering that both systems are similar and decoupled stability analysis can be conducted just for one subsystem. Stator active power subsystem has been tested against 8 sets of regulator k_p and k_i gains showed in Table 3.1

Table 3.1: Values of analysed k_p and k_i gain sets

Gain	Set 1	Set 2	Set 3	Set 4	Set 5	Set 6	Set 7	Set 8
k_p	3.45	2	1	1.75	2.5	2.25	1.1	4
k_i	0.15	0.05	0.00975	0.025	0.045	0.125	0.75	0.25

Frequency responses of tested systems are presented in the Figure 3.7, pole-zero placement map is presnted in Figure 3.8 and Figure 3.9 shows system response for unit step signal. Stability analysis provided necessary info about safe operation region for PI regulator gains which will be used as a baseline for simulation studies and experimental tests. This analysis is used to establish initial parameter of PI controllers for multiscalar structures 1 and 2.

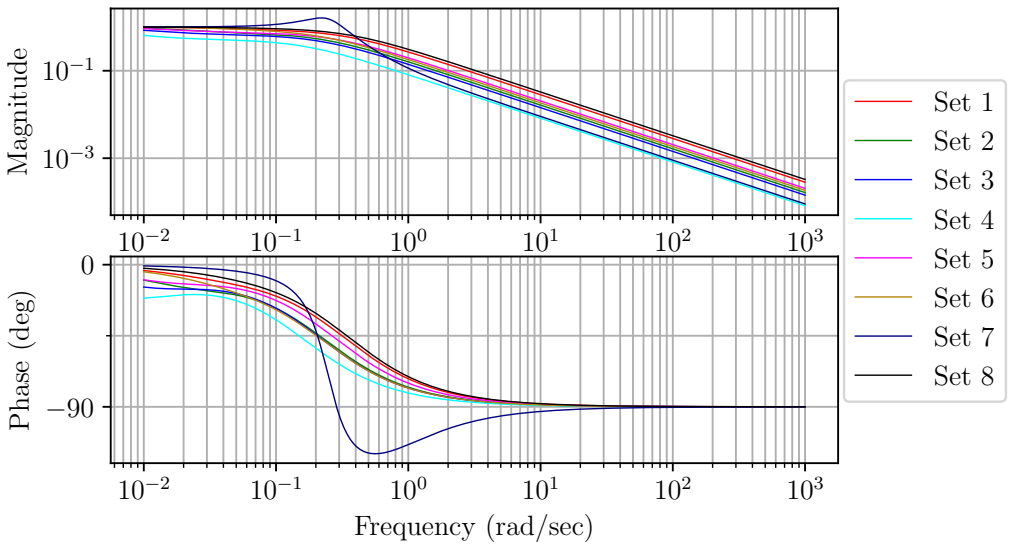

Figure 3.7: Frequency response plots for gain sets presented in Table 3.1

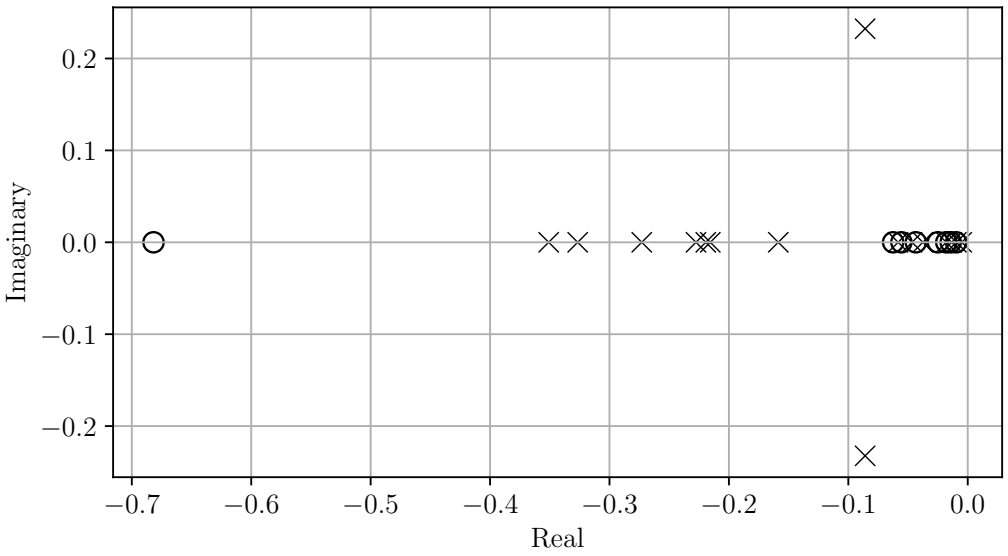

Figure 3.8: The pole-zero map for gain sets presented in Table 3.1

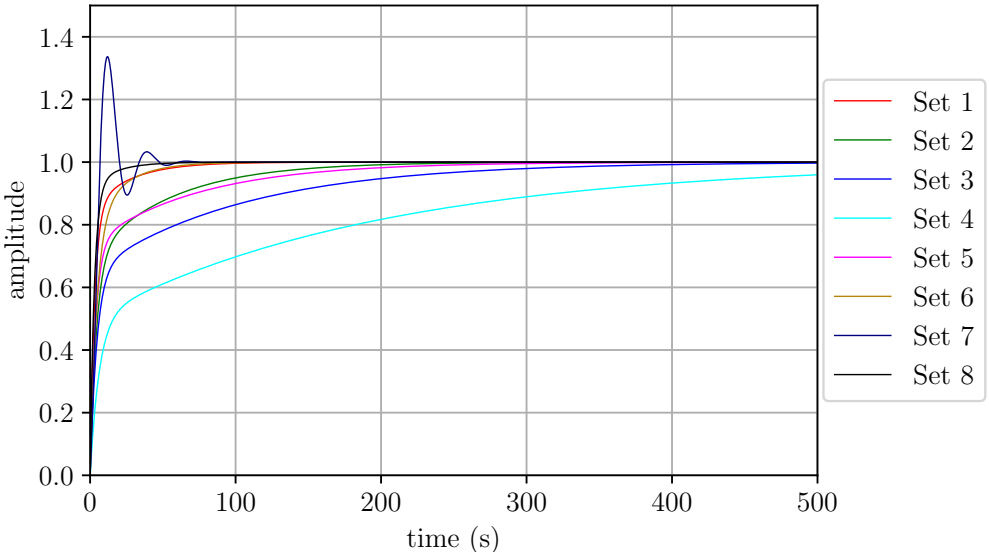

Figure 3.9: Response for unit step for gain sets presented in Table 3.1

For multiscalar structures 3 and 4 system has to be extended to accommodate external control loop. Figure 3.10 shows diagram of the control structure.

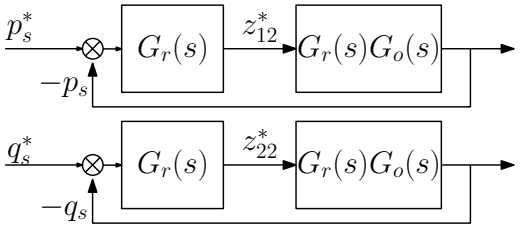

Figure 3.10: Diagram of regulation loops for multiscalar structures 3 and 4

Object can be defined by transfer function that is equal to the closed-loop function from previous example:

$$G_{O1}(s) = G_O(s)G_r(s) = \frac{k_p s + k_i}{s^2 T + (k_p + 1)\, s + k_i} \tag{3.171}$$

where:

$$T = \frac{L_s L_d}{R_s L_d + L_s R_d + R_c}$$

Regulator transfer function is as follows:

$$G_r(s) = k_{p1} + \frac{k_{i1}}{s} \tag{3.172}$$

Multiplying both equations will result in the transfer function of the analysed object:

$$G_{l2}(s) = G_r(s)G_{O1}(s) = \left(k_{p1} + \frac{k_{i1}}{s}\right)\left(\frac{k_p s + k_i}{s^2 T + (k_p + 1)\, s + k_i}\right) \tag{3.173}$$

Closed-loop system transfer functions can be approximated as:

$$G(s) = \frac{G_{l2}(s)}{1 + G_{l2}(s)} \tag{3.174}$$

Considering equations (3.171) and (3.172) $G(s)$ will take the following form:

$$G(s) = \frac{G_{l2}(s)}{1 + G_{l2}(s)} = \frac{\left(k_{p1} + \frac{k_{i1}}{s}\right)\left(\frac{k_p s + k_i}{s^2 T + (k_p + 1)s + k_i}\right)}{1 + \left(k_{p1} + \frac{k_{i1}}{s}\right)\left(\frac{k_p s + k_i}{s^2 T + (k_p + 1)s + k_i}\right)} \tag{3.175}$$

and can be further simplified to:

$$G(s) = \frac{(k_{p1}k_p)s^2 + (k_{p1}k_i + k_{i1}k_p)s + k_{i1}k_i}{s^3T + (k_p + 1 + k_{p1}k_p)\,s^2 + (k_{p1}k_i + k_{i1}k_p + k_i)\,s + k_{i1}k_i} \tag{3.176}$$

Considering that both subsystems are similar and decoupled stability analysis can be conducted just for one subsystem. Stator active power subsystem has been tested against 8 sets of regulator k_{p1} and k_{i1} gains showed in Table 3.2, k_p and k_i gains have been set to values of the Set 1 from the Table 3.1:

Table 3.2: Values of analysed k_{p1} and k_{i1} gain sets

Gain	Set 1	Set 2	Set 3	Set 4	Set 5	Set 6	Set 7	Set 8
k_{p1}	1.45	1	1.75	0.5	1.45	1.25	1.5	1
k_{i1}	0.05	0.15	0.075	0.125	0.05	0.125	0.125	0.05

Frequency responses of tested systems are presented in the Figure 3.11, pole-zero placement map is presnted in Figure 3.12 and Figure 3.13 shows system response for unit step signal. Stability analysis provided necessary information about safe operation region for PI regulator gains which will be used as a baseline for simulation studies and experimental tests. This analysis is used to establish initial parameter of PI controllers for multiscalar structures 3 and 4.

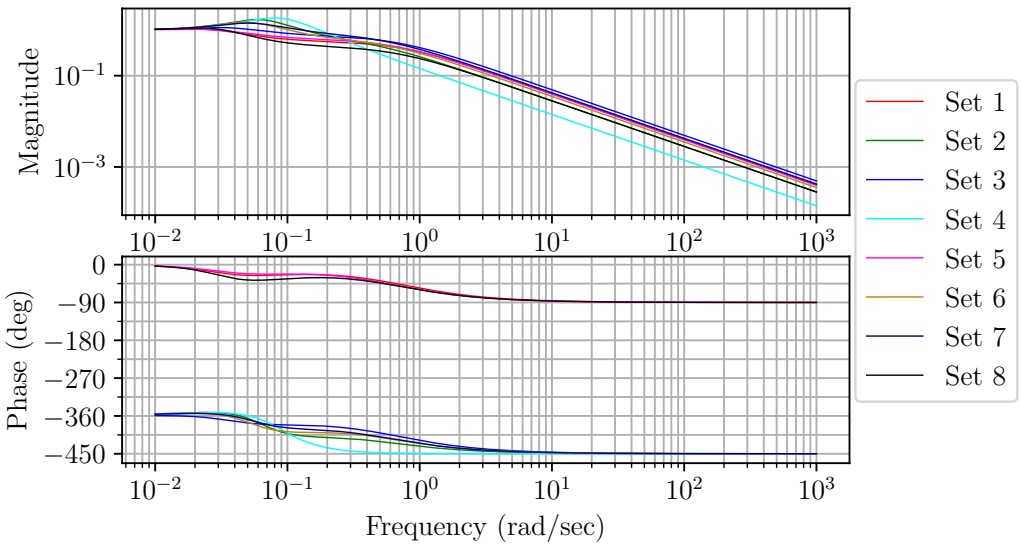

Figure 3.11: Frequency response plots for gain sets presented in Table 3.2

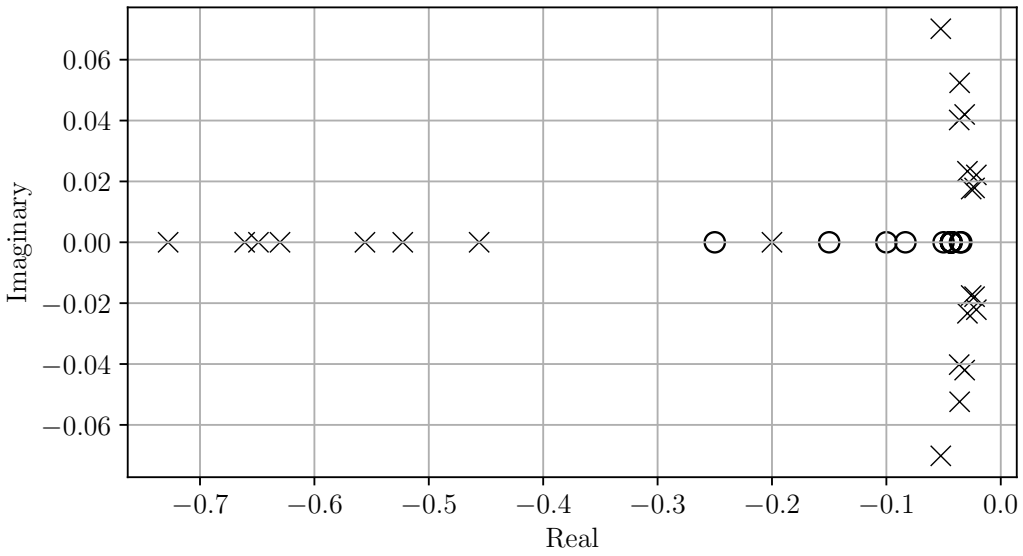

Figure 3.12: The pole-zero map for gain sets presented in Table 3.2

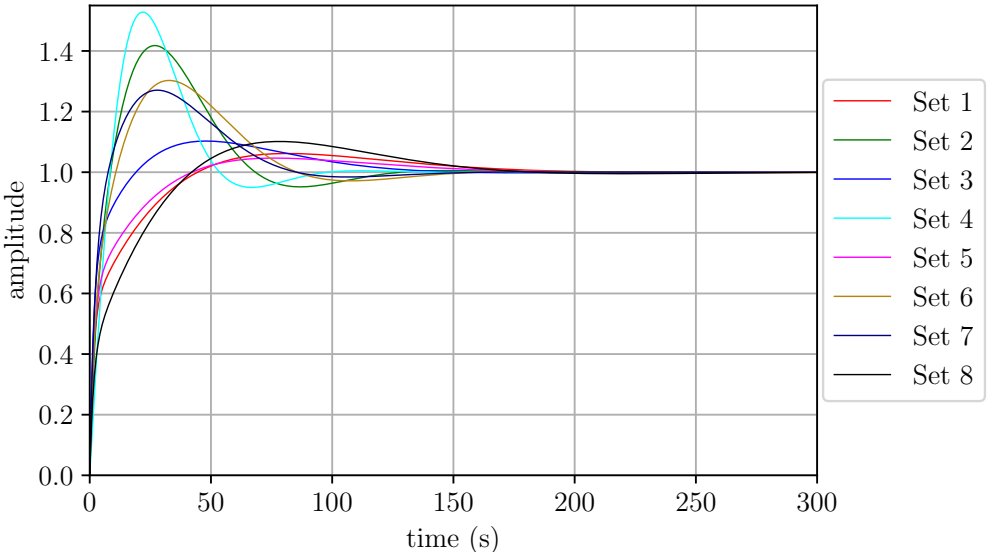

Figure 3.13: Response for unit step for gain sets presented in Table 3.2

Chapter 4

Simulation results

The verification of the control concepts for the Doubly-Fed Induction Generator needed to go through a simulation phase; laying the base for the upcoming experimental generator implementation. This initial development stage was geared towards recognizing and resolving initial challenges.

In accordance with the generator system requirements, the simulation structure must encompass the computation of:

- the vector models of the Doubly-Fed Induction Machine (DFIM);
- the Pulse Width Modulation (PWM) for independent voltage generation for the 1st and 2nd orthogonal planes;
- the Field Oriented Control (FOC) variables;
- the multiscalar variables.

The simulation process involves solving 15 differential equations per method, managing various transformation matrices, and fine-tuning PI controllers. To ensure both accuracy and efficiency in calculations, the decision was made to implement the simulation in PLECS software using the C programming language. Adapting the C programming language facilitates a smooth transition to practical Digital Signal Processor programming during the experimental phase. The simulations did not use an algorithm maintaining a constant rotor speed.

Figure 4.1 presents the overall structure of the simulation procedure. Simulation involves computing control structures, with executions occurring every $100\,\mu s$ based on the DSP time step. This methodology facilitates a practical assessment of the accuracy of state variable estimation. All these considerations provide an insight to problems that may arise during experimental implementation. In the simulations,

a few common comparative tests have been carried out for proposed methods:

- changes of the reference active power - described in Section 4.1;
- changes of the reference reactive power - described in Section 4.2;
- changes of the rotor speed from under-synchronous to over-synchronous speed with constant reference active and reactive powers - described in Section 4.3;
- voltage dips - described in Section 4.4.

Table A.1 (showed in appendix A) contains the analysed DFIG with Current Source Converter system parameters that will be used in the simulations. In this dissertation it is assumed that the parameters of the generator as well as the converter are known and invariant during operation. Those parameters are the the same as in the laboratory test bench. Table A.2 (showed in appendix A) contains gains of the controllers for tested method.

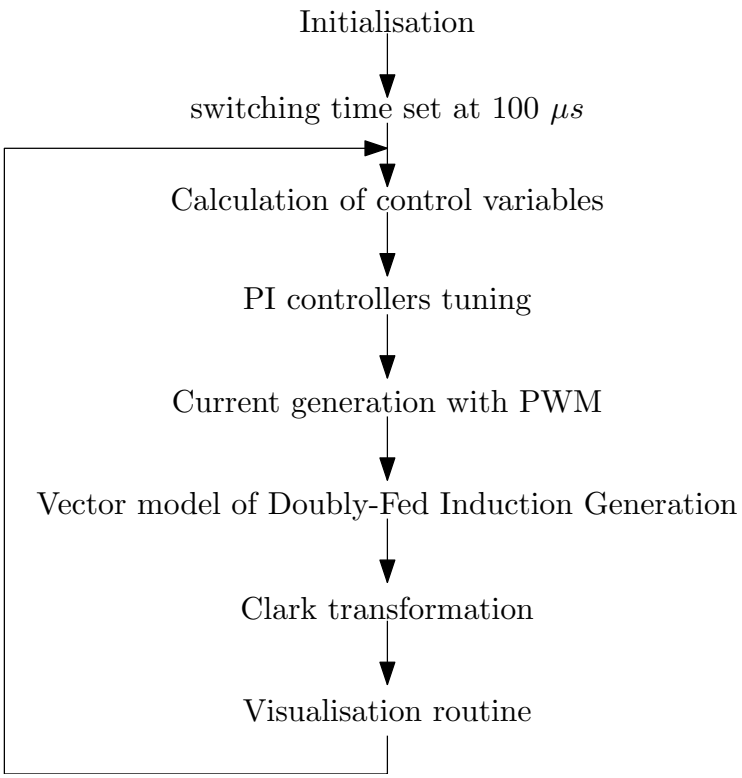

Figure 4.1: Flowchart of the Doubly-Fed Induction Generator connected to Current Source Converter simulation procedure

4.1 Control system behaviour during step changes of the reference active power

The performance of Doubly-Fed Induction Generator (DFIG) model with Field Oriented Control (FOC), presented in Section 3.1, has been evaluated. The implemented machine model in simulation is in orthogonal reference frame $(\alpha - \beta)$ and it is controlled under FOC method.

The model operates with stator active and reactive powers as inputs. The testing procedure for the Doubly-Fed Induction Generator interfaced with the Current Source Converter is presented in Figures 4.2 and 4.3. Mechanical speed is maintained at a constant 700 rpm (0.7 p.u.), providing a stable operational baseline. Simultaneously, the DC-link current is set at 1.5 times the nominal current. This deliberate measure ensures a sustained energy at an elevated level, guaranteeing the optimal functioning of the DFIG:

- at 100 ms the active power reference signal is set from -0.1 to -0.3 p.u. (left column in the figure);
- at 100 ms the active power reference signal is set from -0.3 to -0.1 p.u. (right column in the figure).

The step function is used in order to properly evaluate the performance of control system in dynamic states.

Figure 4.2 is separated into two columns where left groups results for increasing active power and right groups results for decreasing active power. Both of the columns include the waveforms of the rotor, stator and DC-link currents in reference to powers and mechanical angular speed.

Figure 4.3 is separated into two columns where left groups results for increasing active power and right groups results for decreasing active power. Both of the columns include the waveforms of the rotor, stator voltages and DC-link voltage e_d in reference to powers and mechanical angular speed.

In both simulation tests, the system exhibits proper responses to step changes in active power. Despite notable high frequency oscillations presented waveforms are the most optimal among obtained results. There is the potential to reduce steady state fluctuations but such action would proportionally increase the time of transition states. Furthermore, a coupling between active and reactive power is observed, particularly evident at higher active load values.

In summary, the implemented control of the machine achieves desired dynamic response. Simulation tests confirmed the correctness of the equations formulated in Section 3.1. However, the achieved results fall short of expectations due to significant couplings and oscillations.

To enhance the quality of processed energy and mitigate issues associated with prior methodologies, a novel approach outlined in Section 3.2 was proposed and subjected to evaluation through simulation tests. The implemented machine and control models are in orthogonal reference frame ($\alpha - \beta$).

The control block receives inputs of stator active and reactive powers, with parameters for the control loops detailed in Table A.2. Retaining consistency, mechanical and electrical parameters remain unchanged from the preceding setup as referenced in Table A.1. Mechanical speed is set at constant 700 rpm (0.7 p.u.) while reference DC-link current is derived from the $d - q$ components of the rotor current.

The testing procedure in Figures 4.4 and 4.5 mirrors that illustrated, ensuring consistency across evaluations. Both Figure 4.4 and Figure 4.5 are separated into two columns where left groups results for increasing and right groups results for decreasing active power. In Figure 4.4, columns include the waveforms of the rotor, stator and DC-link currents in reference to powers and mechanical angular speed. While in Figure 4.5, waveforms of the rotor, stator voltages and DC-link voltage e_d are appropriately displayed.

In both the conducted tests, the system responds correctly to a step change of active power. In comparison with previously described Field Oriented Control method, the generator system exhibits significantly reduced transient states duration, particularly evident during load reduction. Additionally, high frequency fluctuations in steady state are minimized. However this method is characterized by considerable overshoots during transient states. It is associated with mutual relation between control loops and decoupling block as well as excess power stored in DC-link.

Simulations validate the equations outlined in Section 3.2, affirming the accuracy of the proposed multiscalar control approach. While proving superior to Field Oriented Control in terms of transient state duration and high-frequency oscillations, this method introduces distinct challenges, noticeable overshoots during transient states. Such events might cause increased electrical exposures and elevated cost of

the converter resulting from the need to use modules capable of handling higher power conversion.

The research successfully identified and implemented strategies to significantly reduce overshoots, thus enhancing the stability of the system. As can be seen on Figures 4.6 and 4.7 multiscalar control method described mathematically in Section 3.3 allowed to reduce the problem of the previous method. However, the transition state has been extended due to complexity of proposed decoupling functions. Due to the significant computational cost, the analysis of this control method was concluded with the simulation verification of mathematical models.

Figures 4.8 and 4.9 show simulation results of multiscalar control method described mathematically in Section 3.4. It is worth noting that despite much simpler decoupling equations, this method is characterized by a significant reduction in transient states duration compared to Field Oriented Control. A negative feature of this control are oscillations in the steady state, especially noticeable at higher values of active power.

Figures 4.10 and 4.11 show simulation results of multiscalar control method described mathematically in Section 3.5. It is worth noting that the change of reference system did not negatively affect the dynamics of the system.

All presented multiscalar control systems respond correctly to a step change of active power. Progressive reduction of overshoots and time of the transient states can be observed. Additionally, high frequency fluctuations in steady state are reduced to minimum.

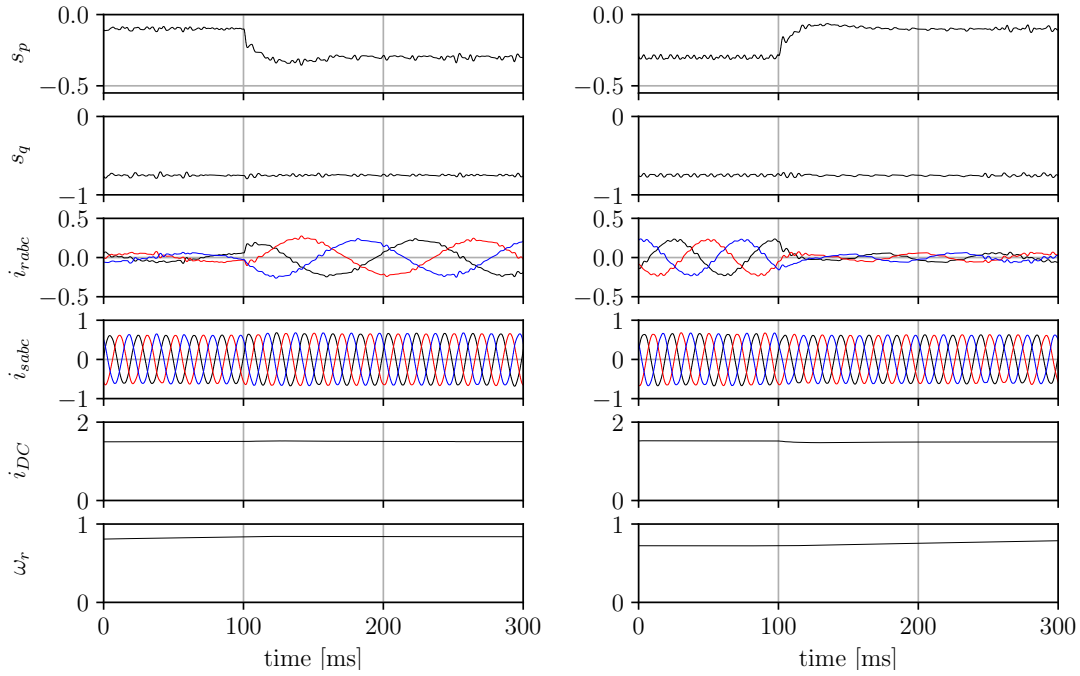

Figure 4.2: Simulation waveforms of currents during step changes of active power for Field Oriented Control

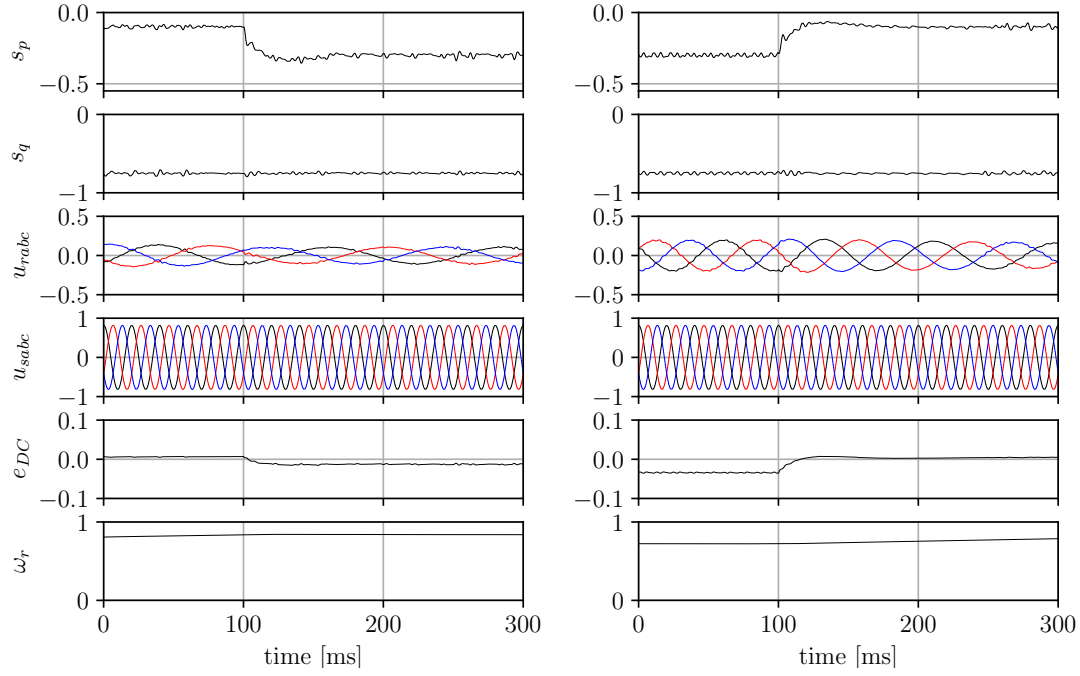

Figure 4.3: Simulation waveforms of voltages during step changes of active power for Field Oriented Control

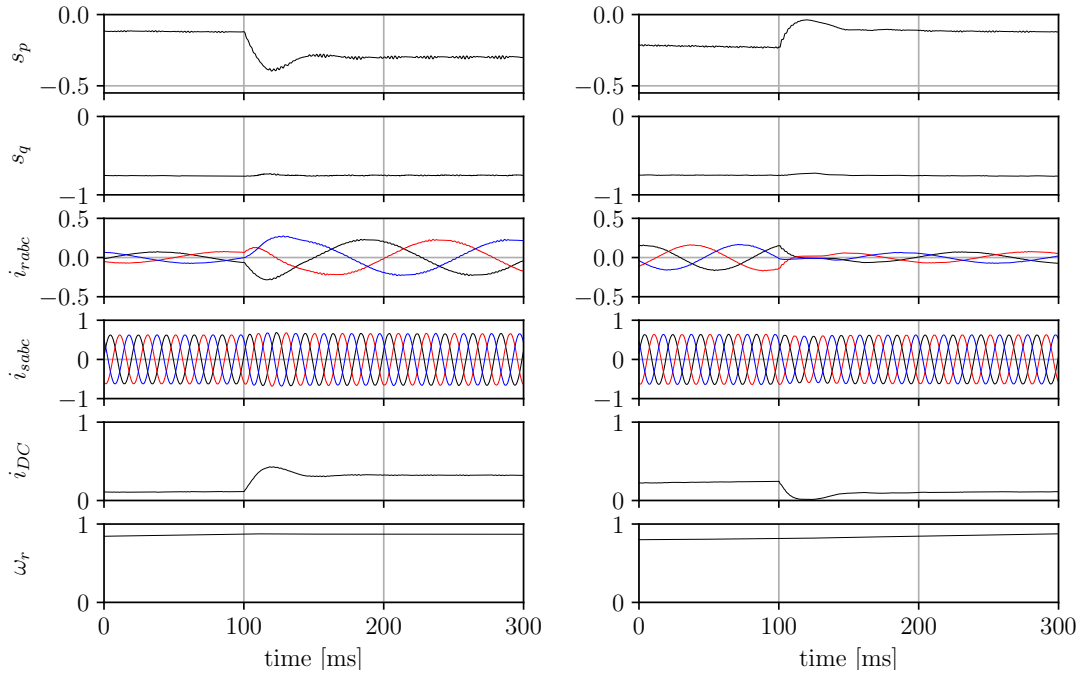

Figure 4.4: Simulation waveforms of currents during step changes of active power for multiscalar control structure 1

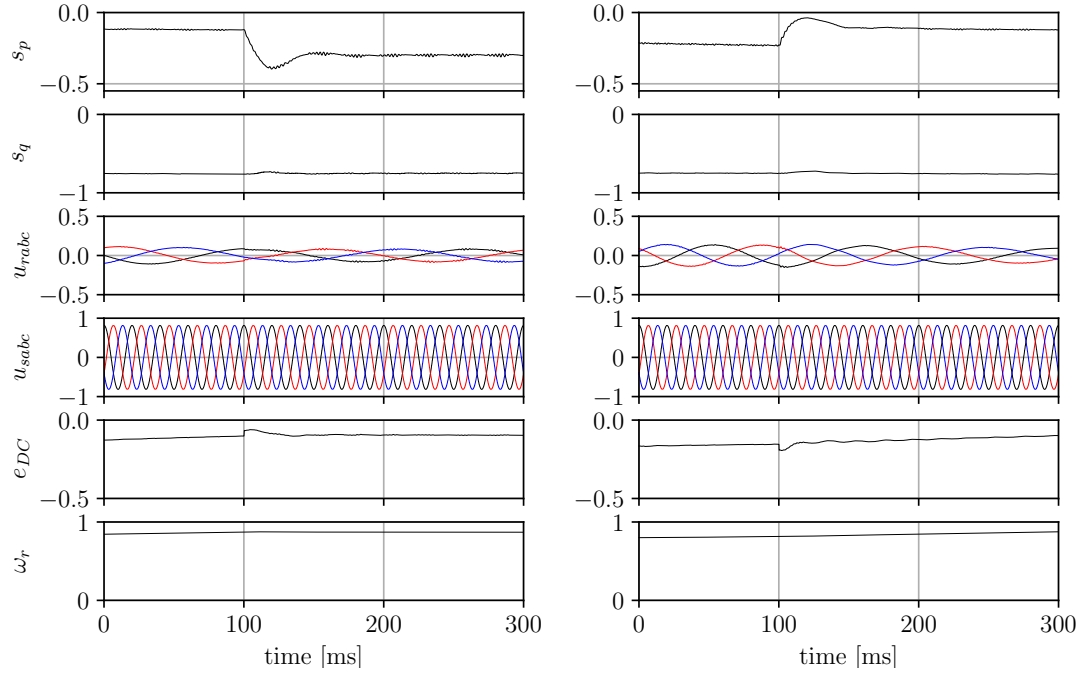

Figure 4.5: Simulation waveforms of voltages during step changes of active power for multiscalar control structure 1

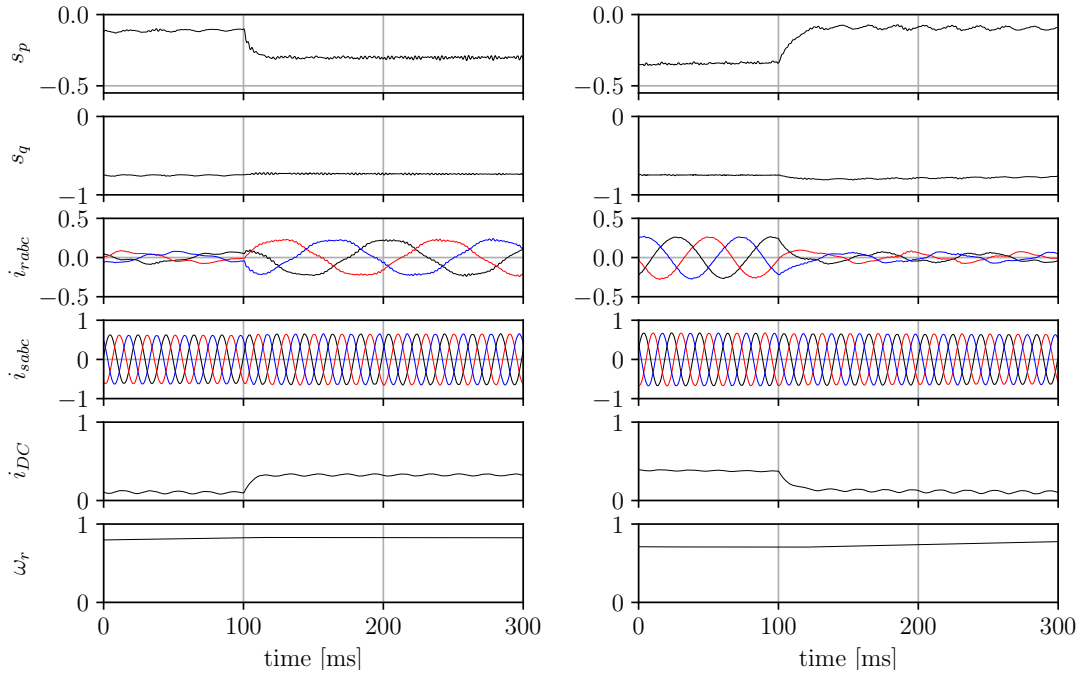

Figure 4.6: Simulation waveforms of currents during step changes of active power for multiscalar control structure 2

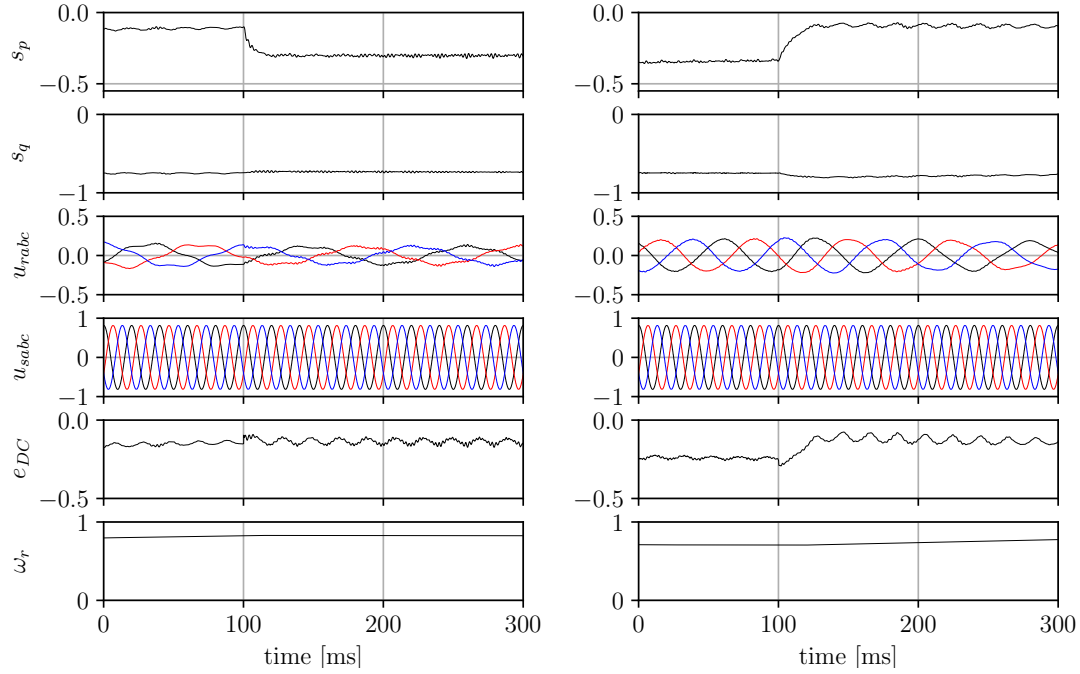

Figure 4.7: Simulation waveforms of voltages during step changes of active power for multiscalar control structure 2

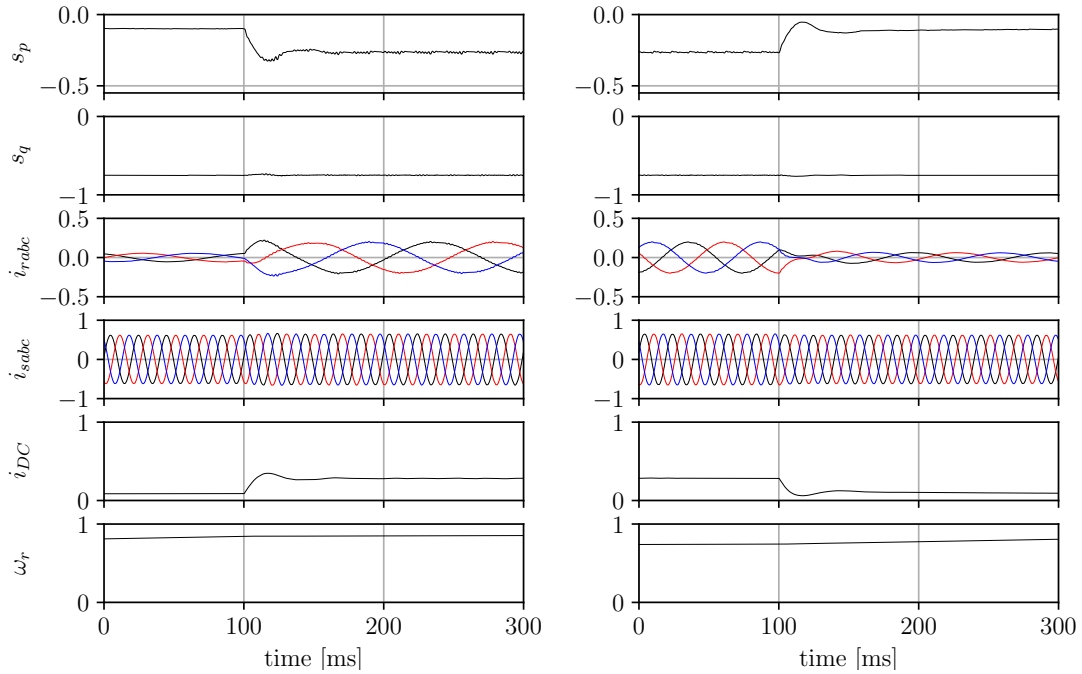

Figure 4.8: Simulation waveforms of currents during step changes of active power for multiscalar control structure 3

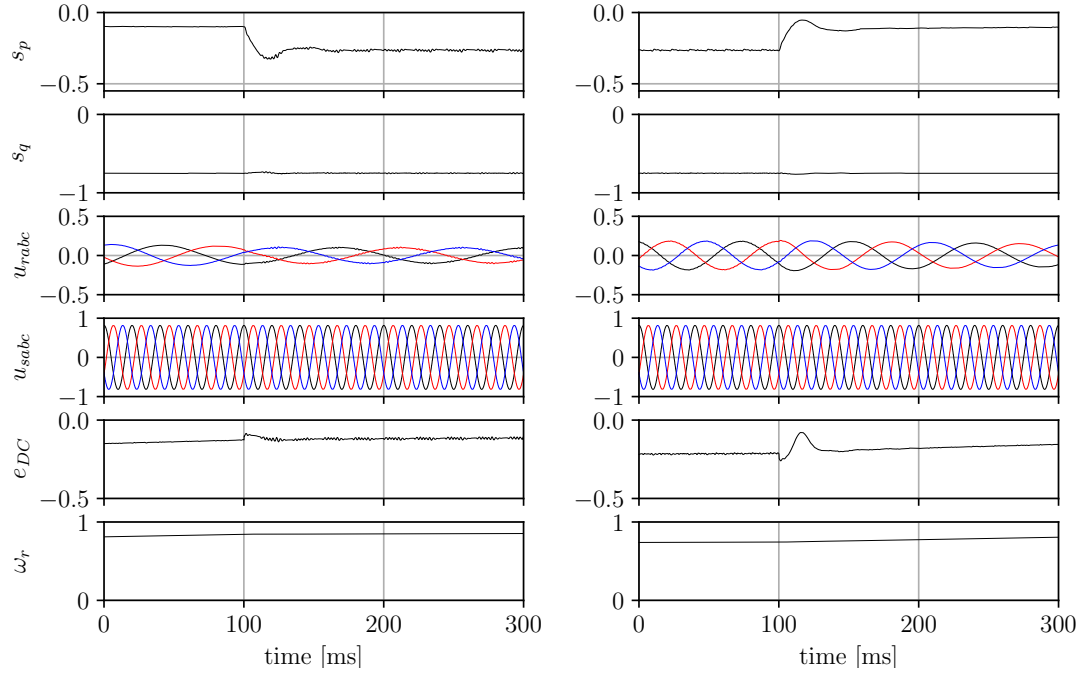

Figure 4.9: Simulation waveforms of voltages during step changes of active power for multiscalar control structure 3

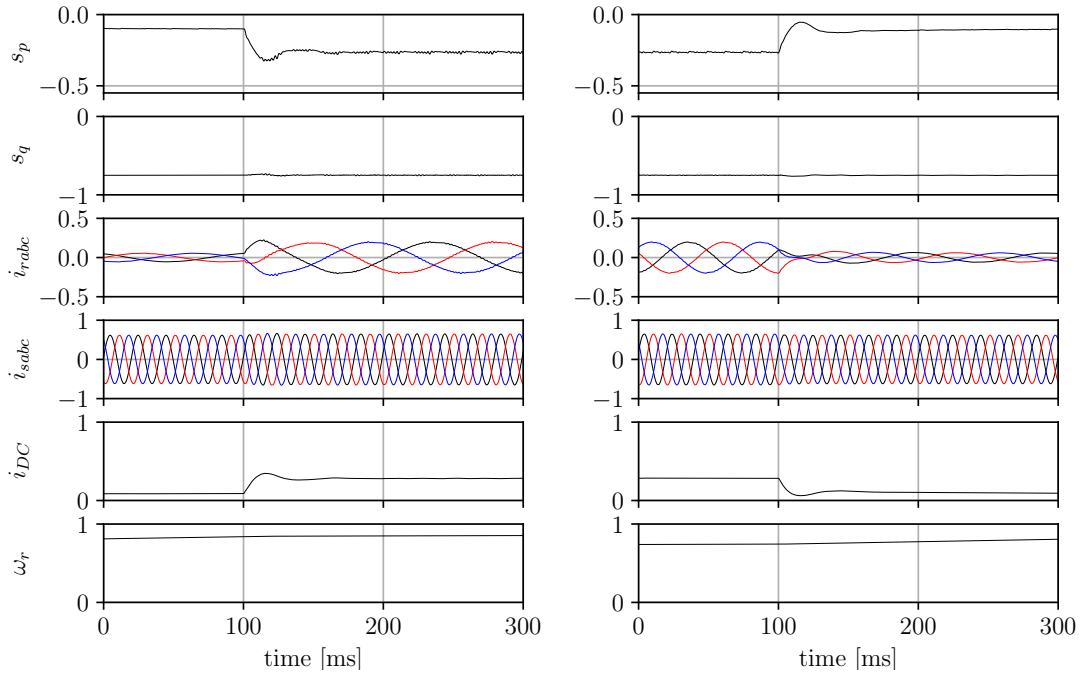

Figure 4.10: Simulation waveforms of currents during step changes of active power for multiscalar control structure 4

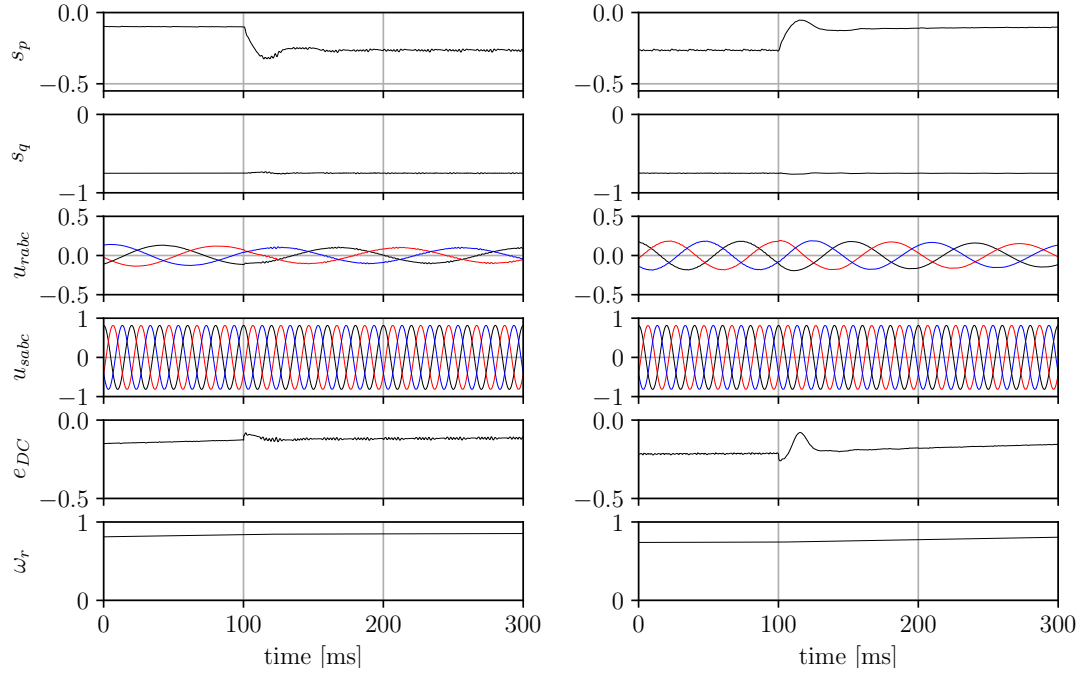

Figure 4.11: Simulation waveforms of voltages during step changes of active power for multiscalar control structure 4

4.2 Control system behaviour during step changes of the reference reactive power

Maintaining the same machine and control system parameters as in Section 4.1 the performance of DFIG, for all control methods described in Sections 3.1 – 3.5, under step changes of the reference reactive power has been investigated. The testing procedure for all of the methods is as follows:

- at 100 ms the active power reference signal is set from -0.75 to -0.5 p.u. (left column in the figure);
- at 100 ms the active power reference signal is set from -0.5 to -0.75 p.u. (right column in the figure).

Beginning with Field Oriented Control, Figure 4.12 is divided into two columns. In the left column, results are organized for increasing reactive power, while the right column showcases outcomes for decreasing reactive power. Each column features waveforms depicting the relationships between rotor, stator, and DC-link currents concerning powers and mechanical angular speed. Similarly, Figure 4.13 is structured into two columns. The left column encapsulates results for increasing reactive power, while the right column stores outcomes for decreasing reactive power. In both columns, the waveforms portray the interactions among rotor, stator voltages, and DC-link voltage e_d relative to powers and mechanical angular speed.

In both tests, the system exhibits proper responses to step changes in reactive power. Despite notable high frequency oscillations presented waveforms are the most optimal among obtained results. Furthermore, flattening in rotor current waveforms at the higher load of reactive power can be noticed. Subsequent analysis revealed that this phenomenon arises from insufficient active power supplied to the machine, leading to challenges in maintaining a sufficiently high output current. To ensure continuity and comparability, the results of the original simulations are presented. There is the potential to reduce steady state fluctuations at cost of increasing the transition state times. Furthermore, a coupling between active and reactive power also can be observed, particularly evident at higher load values.

In conclusion, the applied control strategy attains the desired response to step changes in reactive powers. Once more, simulations validate the accuracy of the equations outlined in Section 3.1. However, the obtained results do not meet

expectations, primarily due to substantial couplings, oscillations and saturation of the machine.

Similar to the tests involving step changes in active power, mulitscalar control structure 1 (mathematical description in Section 3.2) was subjected to simulation tests. The improvements in processed energy quality and the mitigation of issues associated with the previous methodology are evident in Figure 4.14 and Figure 4.15. In both figures, the system responds accurately to a step change in reactive power. When compared to the previously tested Field Oriented Control method, the generator system exhibits significantly reduced high-frequency fluctuations in steady state. Despite much longer transition state for increasing the reactive power, this approach is characterized by reduced transient states when the power decreases. Additionally, it is noteworthy that there is an absence of flattening in the rotor current.

As can be seen on Figures 4.16 and 4.17 multiscalar control described mathematically in Section 3.3 allowed to increase overall dynamics of the system at cost of more significant high frequency oscillations in steady states.

Figures 4.18 and 4.19 show simulation results of multiscalar control method described mathematically in Section 3.4. It is worth noting that despite much simpler decoupling equations, this method is characterized by a reduction in transient states duration. A negative feature of this control are oscillations noticeable at higher values of active power.

Figures 4.20 and 4.21 show simulation results of multiscalar control method described mathematically in Section 3.5. It is worth noting that the change of reference system did not negatively affect the dynamics of the system.

Simulation results confirm the validity of the equations detailed in Sections 3.2 – 3.5, substantiating the precision of the proposed multiscalar control methods. Outperforming the FOC in both transient state duration and high-frequency oscillations, all presented multiscalar control systems exhibit accurate responses to step changes in reactive power with minimal coupling between powers. A progressive reduction in overshoots and transient state duration is observed, accompanied by a noteworthy minimization of high-frequency fluctuations in steady state.

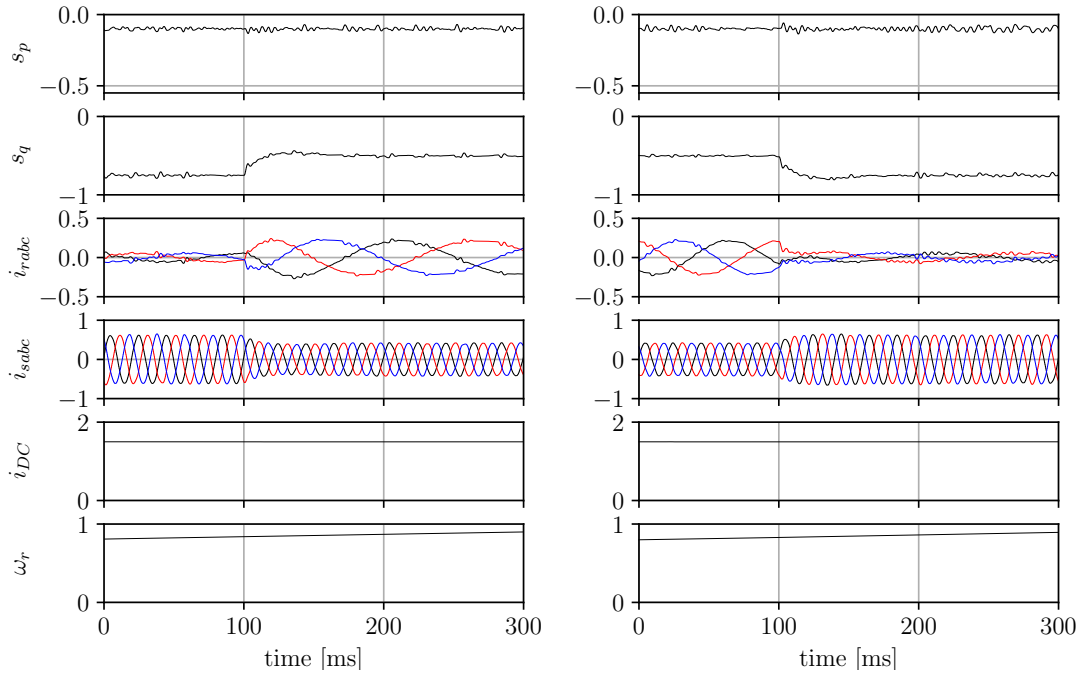

Figure 4.12: Simulation waveforms of currents during step changes of reactive power for Field Oriented Control

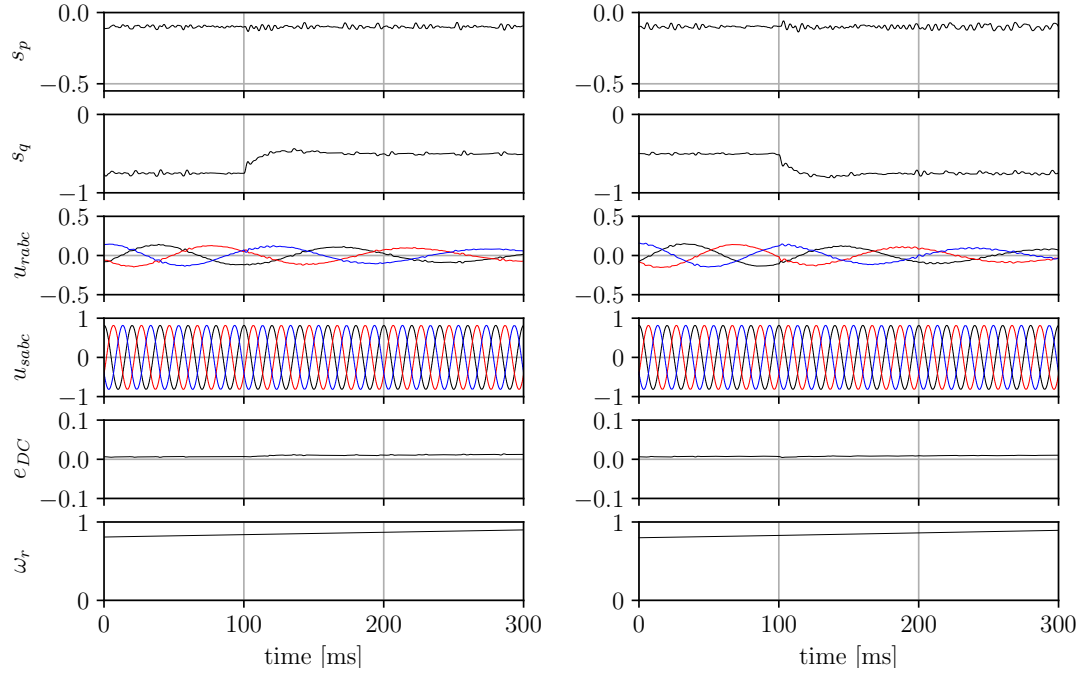

Figure 4.13: Simulation waveforms of voltages during step changes of reactive power for Field Oriented Control

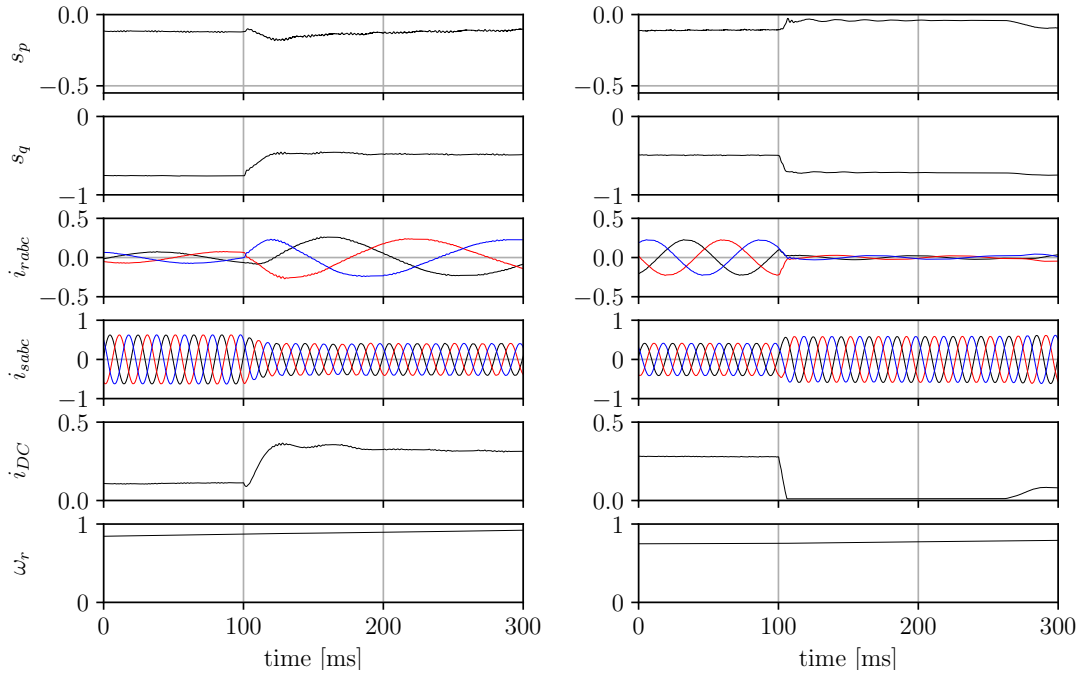

Figure 4.14: Simulation waveforms of currents during step changes of reactive power for multiscalar control structure 1

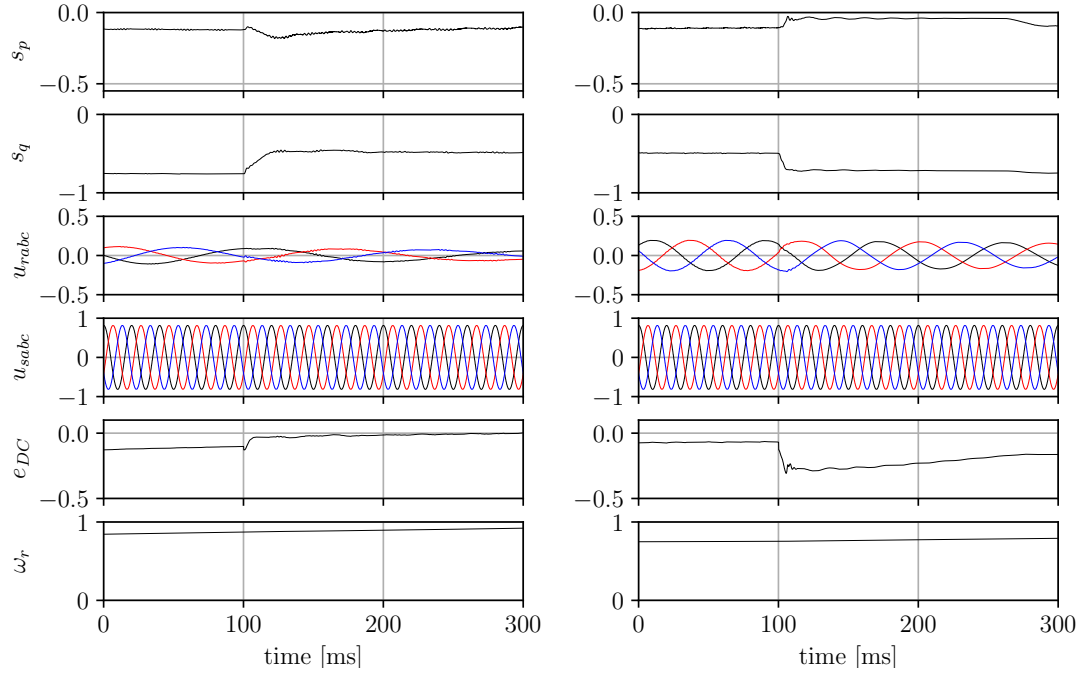

Figure 4.15: Simulation waveforms of voltages during step changes of reactive power for multiscalar control structure 1

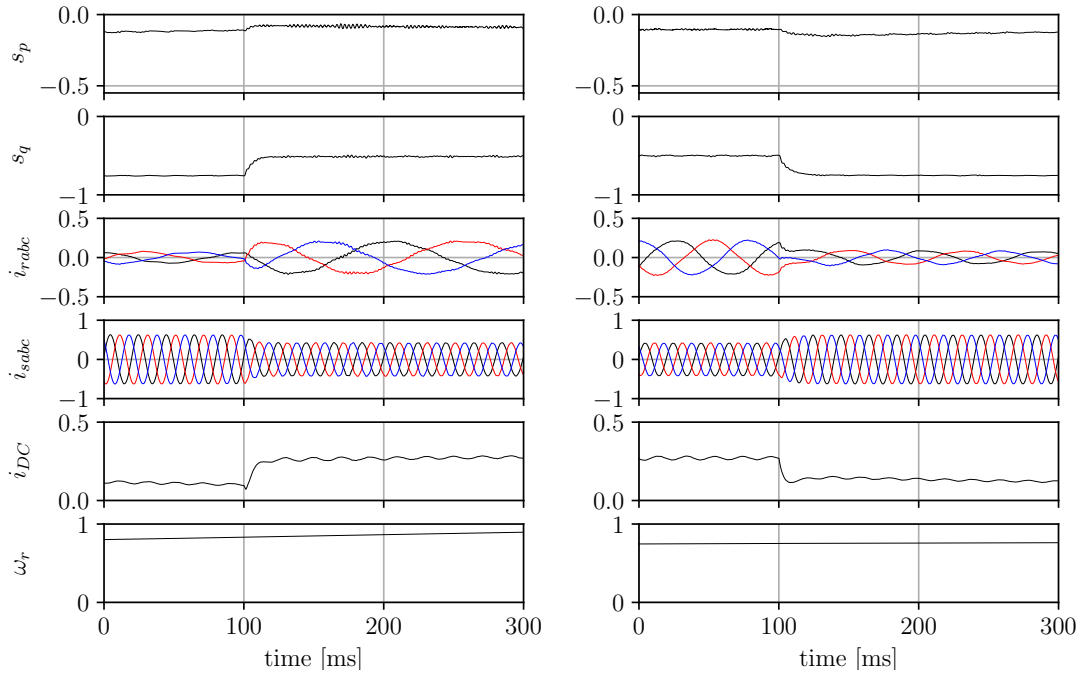

Figure 4.16: Simulation waveforms of currents during step changes of reactive power for multiscalar control structure 2

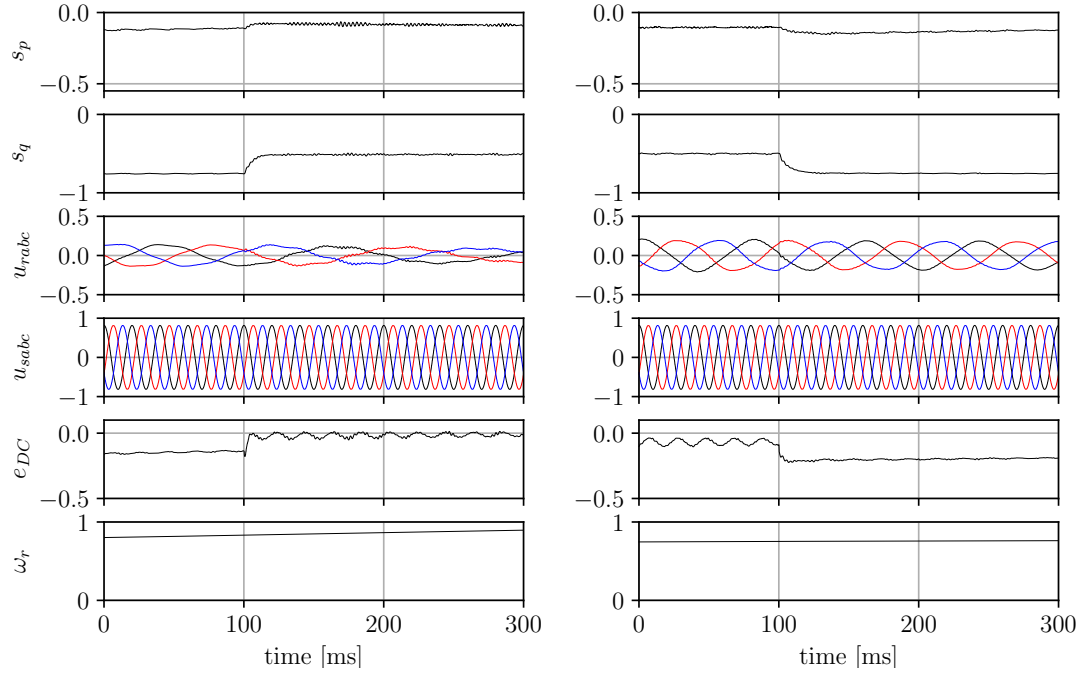

Figure 4.17: Simulation waveforms of voltages during step changes of reactive power for multiscalar control structure 2

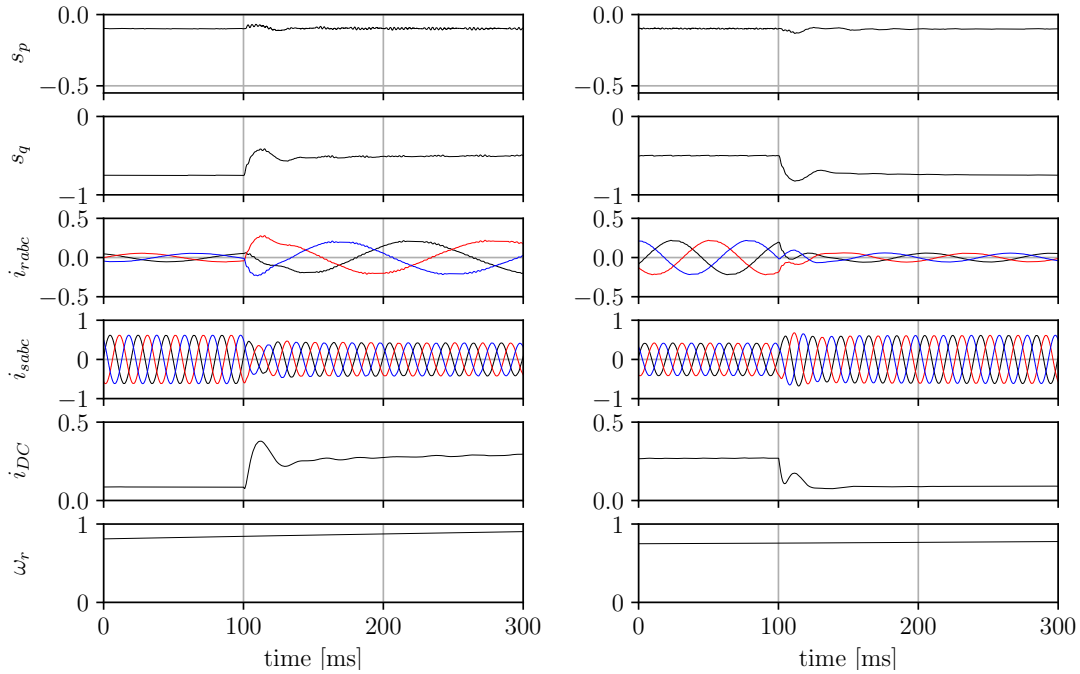

Figure 4.18: Simulation waveforms of currents during step changes of reactive power for multiscalar control structure 3

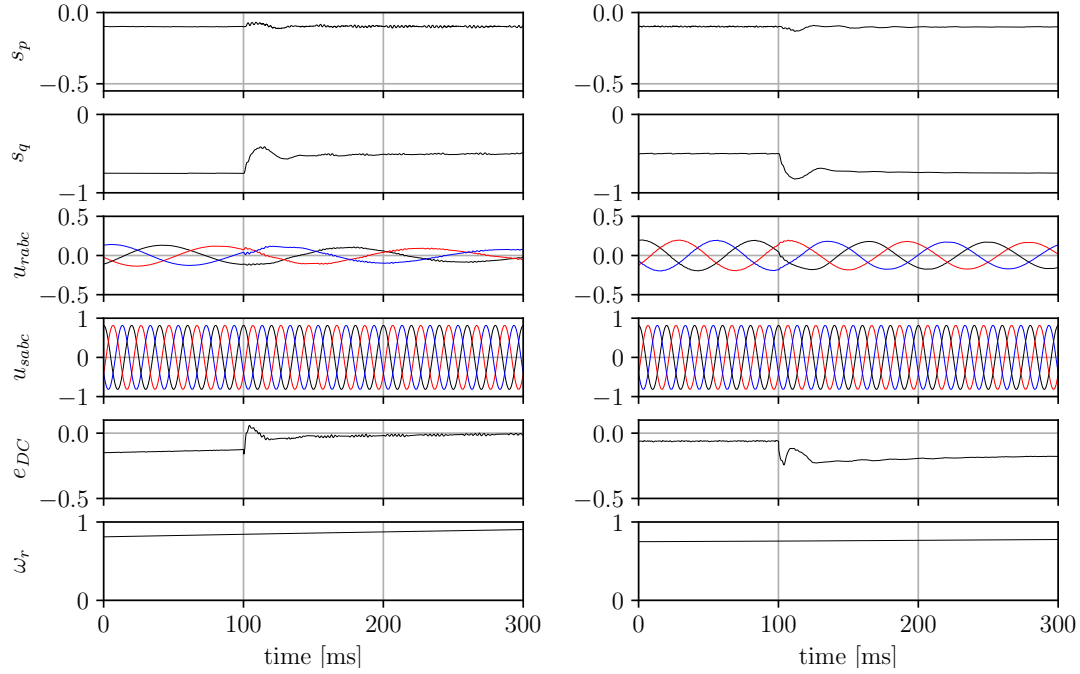

Figure 4.19: Simulation waveforms of voltages during step changes of reactive power for multiscalar control structure 3

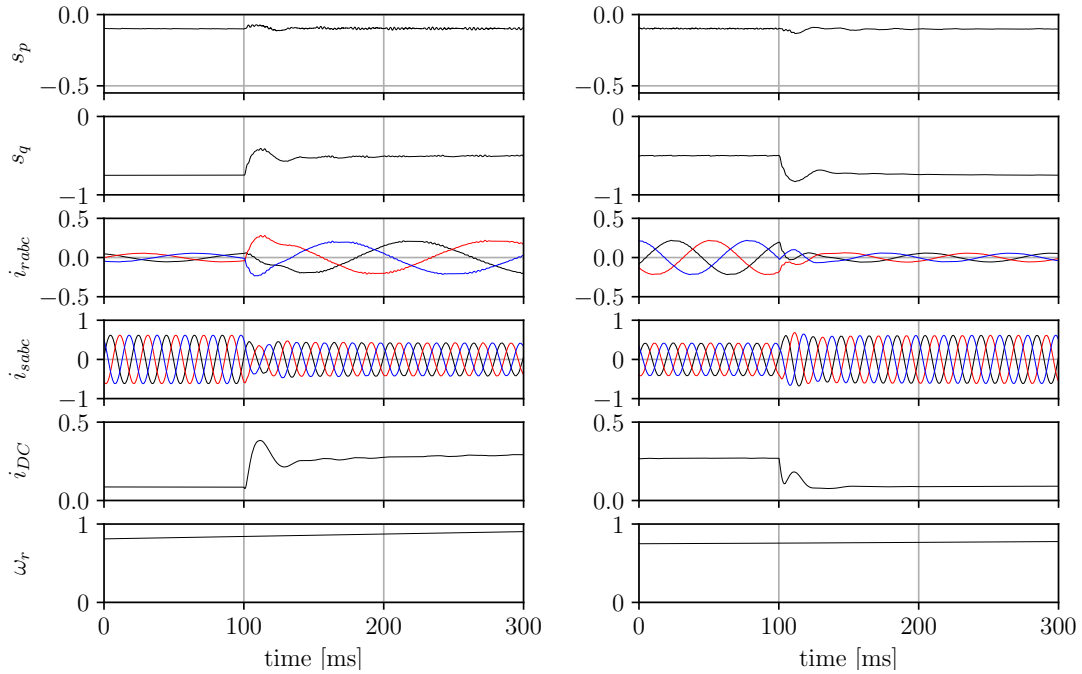

Figure 4.20: Simulation waveforms of currents during step changes of reactive power for multiscalar control structure 4

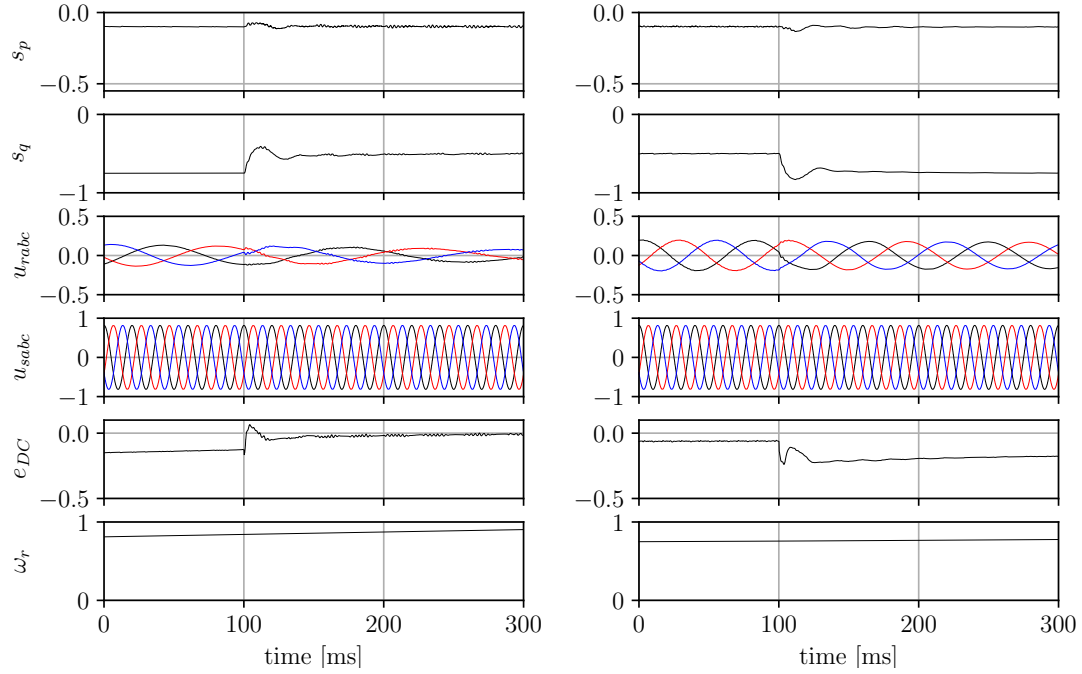

Figure 4.21: Simulation waveforms of voltages during step changes of reactive power for multiscalar control structure 4

4.3 Control system behaviour during changes of the rotor speed with constant reference powers

After the preceding simulation tests, another crucial set of experiments was carried out for all the methods. The testing procedure is outlined as follows:

- active power is set and maintained at $s_p = -0.1\,p.u.$;
- reactive power is set and maintained at $s_p = -0.75\,p.u.$;
- angular speed is changing from $\omega_r = 0.8\,p.u.$ to $\omega_r = 1.25\,p.u.$.

Analysing the dynamic responses of the system controlled under Field Oriented Control during speed transition shown on Figure 4.22, it is noteworthy that the active and reactive powers are consistent, exhibiting stability with minimal deviations. However, the pronounced distortions in these current and voltage waveforms merit further analysis to understand their implications on the overall performance and efficiency of the system under consideration. In the Figure 4.23, depicting the first of multiscalar methods it can be noticed that, despite the proper response for the speed change, control system was not able to maintain stable active and reactive power waveforms due to disturbances in the rotor currents after exceeding the synchronous speed. This is related to the reversal of rotation direction of the space vector fed to the control system. This phenomenon became evident during experiments conducted at the laboratory stand. Further explanation and proposed solutions will be detailed in Chapter 5.

The second of the proposed multiscalar methods (described Section 3.3) showed in the Figure 4.24 did not exhibit the same behaviour as the previously tested control scheme. Unlike the prior method, it successfully maintained constant active and reactive power outputs. Furthermore, in comparison to both Field Oriented Control and multiscalar control structure 1 methods, the rotor and stator currents, as well as rotor voltages are sinusoidal without noticeable distortions for entire duration of the experiment. Finally, the multiscalar control structures 3 and 4 were also evaluated under same scenario. Results presented in the Figure 4.25 and 4.26 respectively indicate their capability to maintain not only a constant power output, but also sinusoidal waveforms of rotor and stator currents and voltages.

In summary, simulation evaluation confirm the validity of all proposed methods, detailed in Sections 3.1 – 3.5.

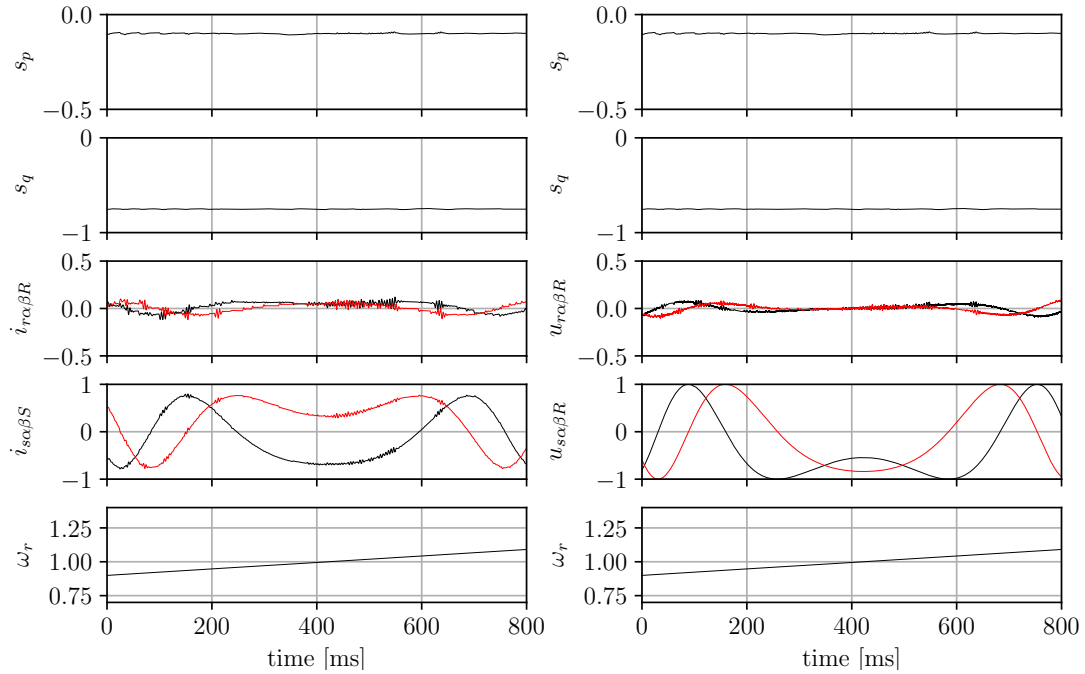

Figure 4.22: Simulation waveforms during change of speed from sub- to super-synchronous for Field Oriented Control

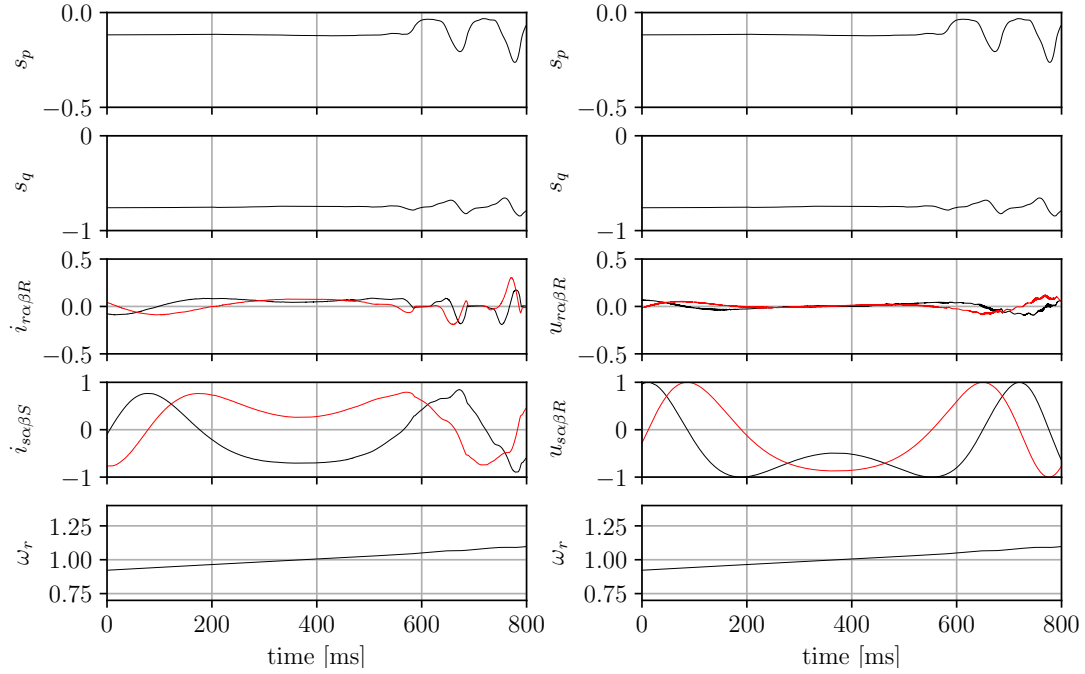

Figure 4.23: Simulation waveforms during change of speed from sub- to super-synchronous for multiscalar control structure 1

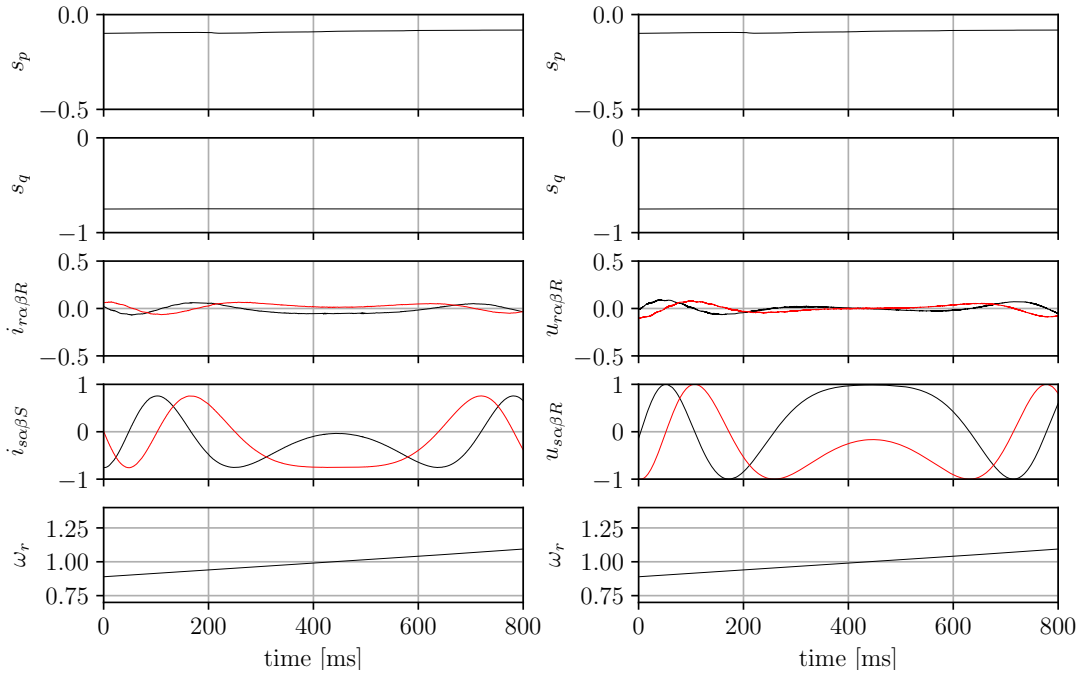

Figure 4.24: Simulation waveforms during change of speed from sub- to super-synchronous for multiscalar control structure 2

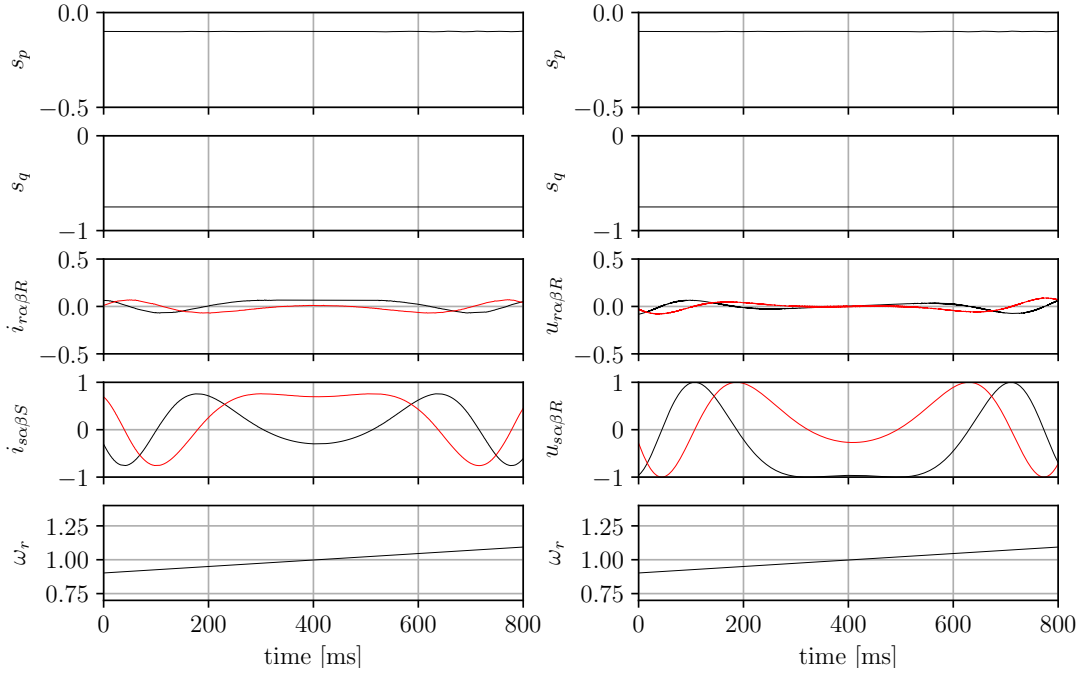

Figure 4.25: Simulation waveforms during change of speed from sub- to super-synchronous for multiscalar control structure 3

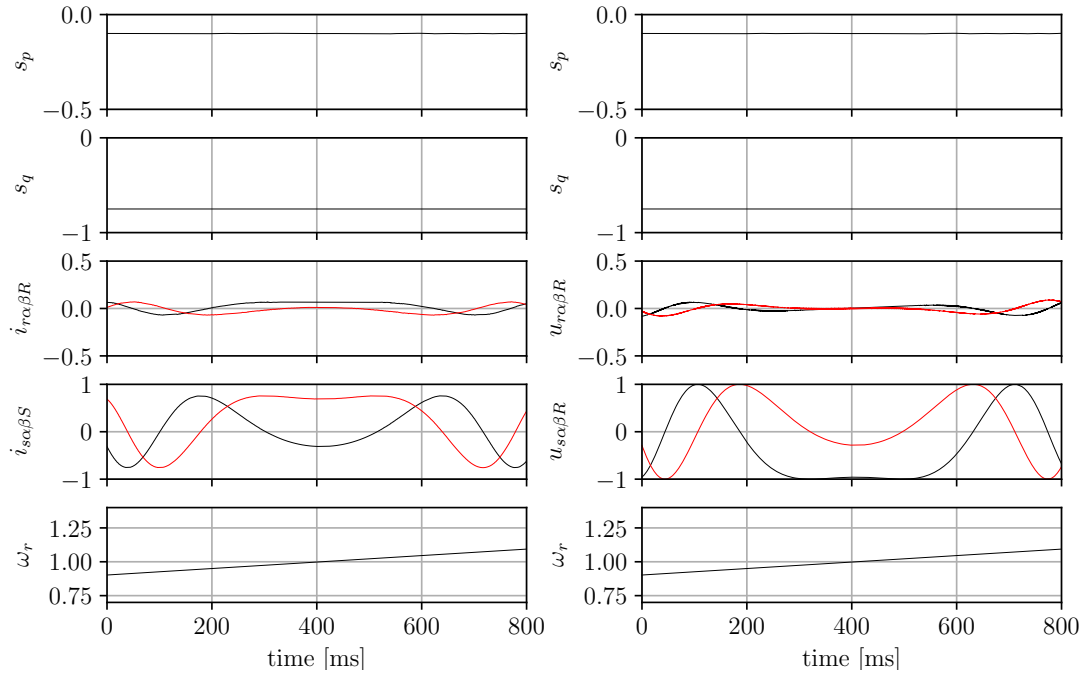

Figure 4.26: Simulation waveforms during change of speed from sub- to super-synchronous for multiscalar control structure 4

4.4 Control system behaviour during changes in grid voltage

Lastly, simulation tests were carried out to validate the control systems' behaviour during voltage dips. This phenomena refers to a brief, temporary reduction in the voltage magnitude within a distribution or customer's electrical system. Voltage dip (Figure 4.27) is characterized by a decrease between 10 and 90 percent of the normal voltage value, lasting for a duration of 0.5 cycles and extending up to 1 minute, [92–95]. According to their duration they can be categorized as:

- instantaneous - last between 0.5 and 30 cycles;
- momentary - last between 30 cycles and 3 seconds;
- temporary - last between 3 seconds to 1 minute.

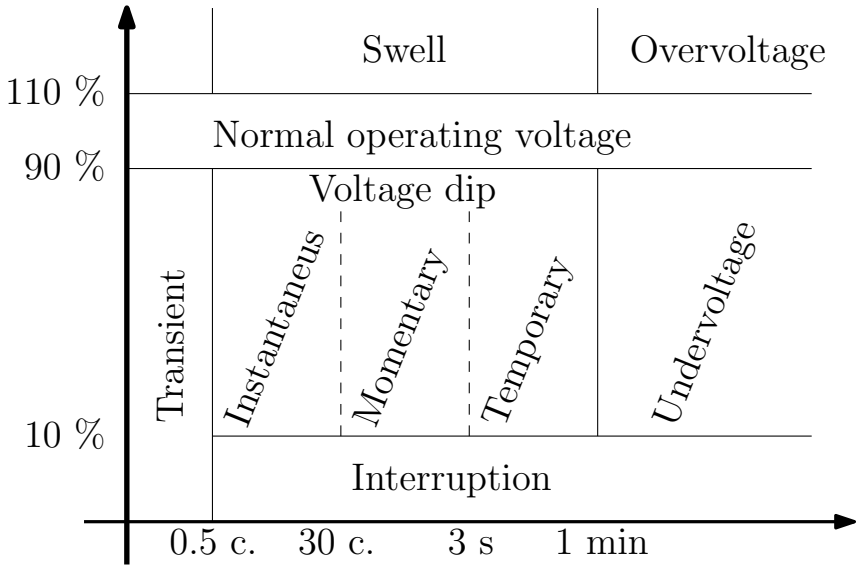

Figure 4.27: Voltage dips according to IEEE Std. 1159-2019, [95]

Although a broad spectrum of voltage dips was analysed within the power system, proposed methods have been tested under the following procedure:

- active power is set and maintained at $s_p = -0.1\,p.u.$;
- reactive power is set and maintained at $s_q = -0.75\,p.u.$;
- at 100 ms the stator voltage is lowered to $U_s = 0.75\,p.u.$;
- at 300 ms the stator voltage is set back to $U_s = 0.95\,p.u.$.

Examining Figures 4.28 through 4.32, it is evident that all the discussed methods successfully restored the system to its pre-voltage dip state. The figures illustrate

that, for each tested method, there was a temporary alteration in the direction of active power flow, associated with a momentary shift in the control angle. Conducted analysis demonstrates that the Field Oriented Control emerged as the most effective in terms of overall characteristics and dynamic response among the four methods tested. Followed closely by the FOC, which was impacted by the significantly increased time of stabilization.

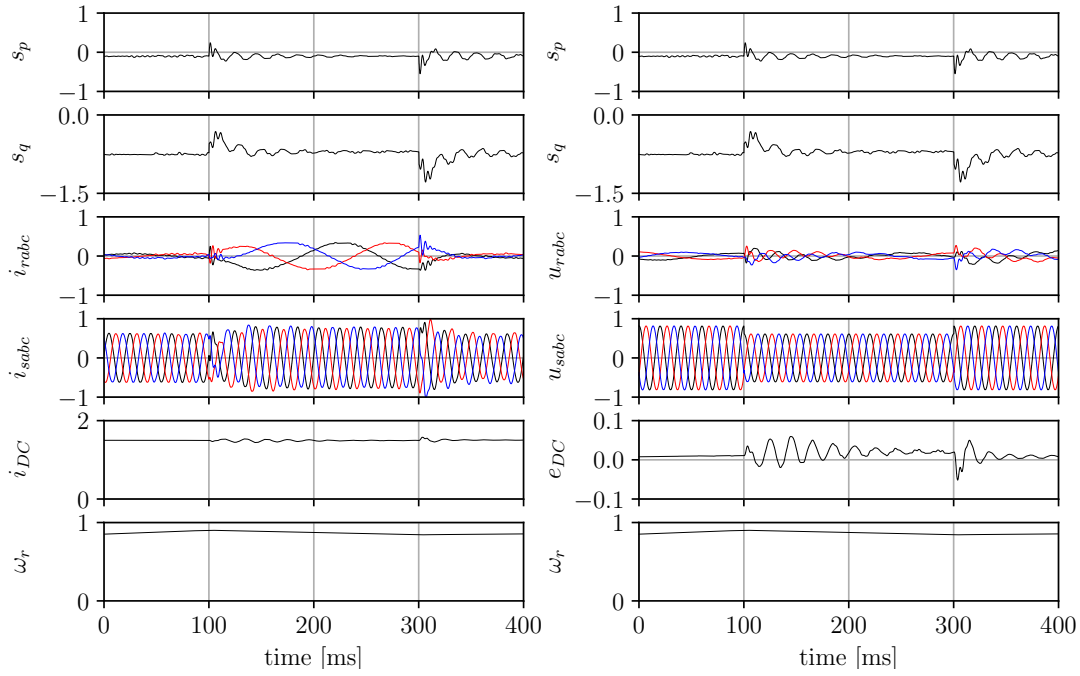

Figure 4.28: Simulation results of voltage dips - Field Oriented Control

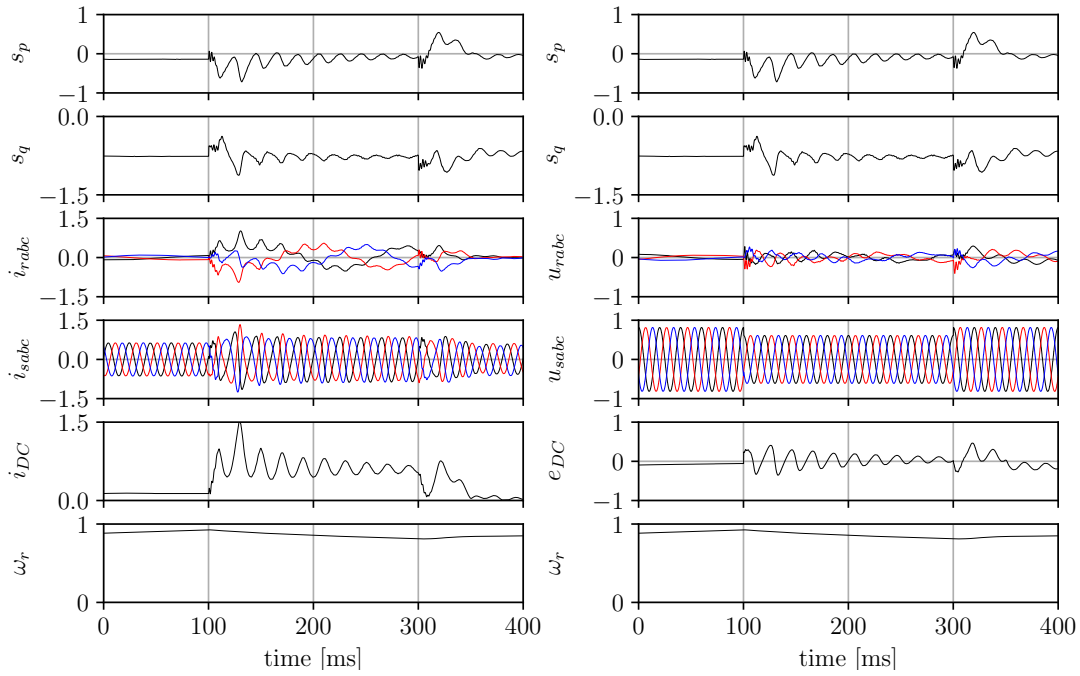

Figure 4.29: Simulation results of voltage dips - multiscalar control structure 1

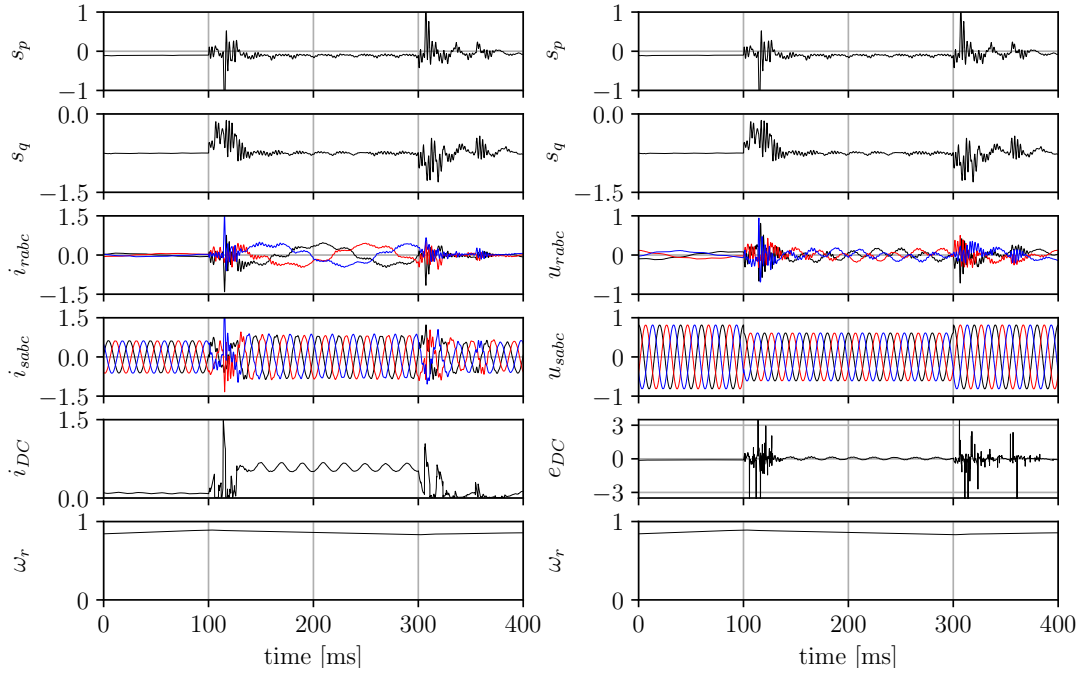

Figure 4.30: Simulation results of voltage dips - multiscalar control structure 2

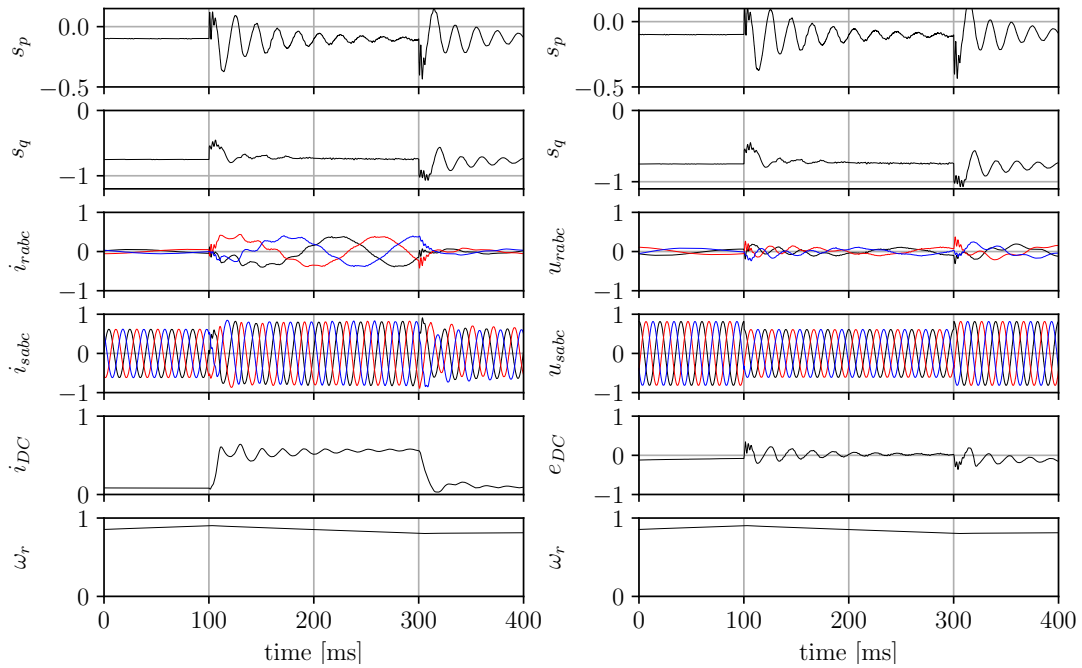

Figure 4.31: Simulation results of voltage dips - multiscalar control structure 3

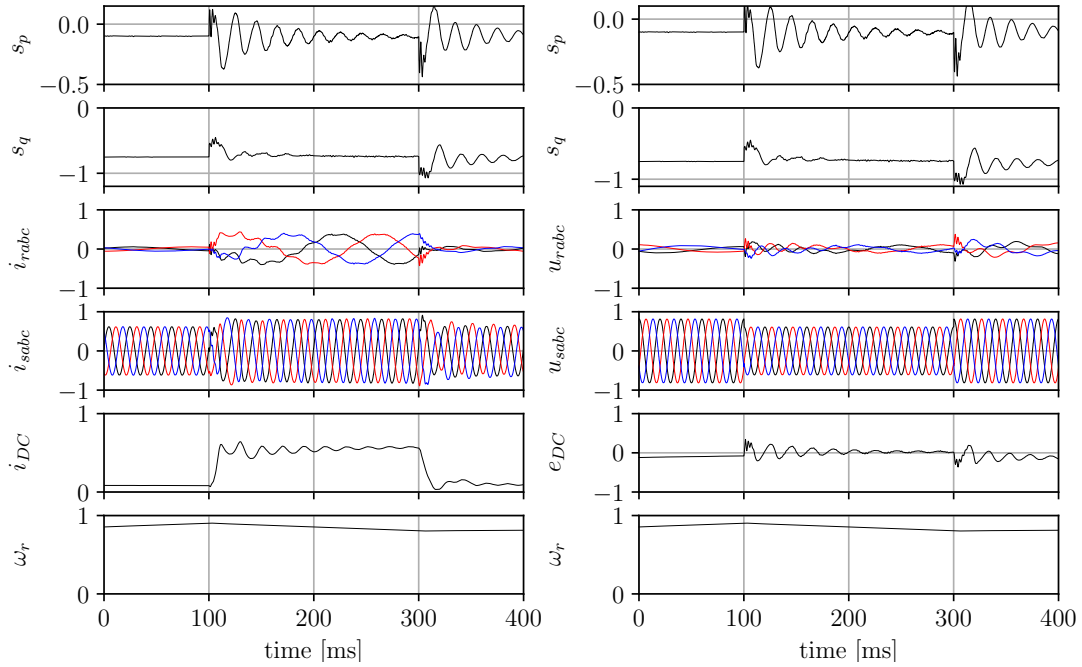

Figure 4.32: Simulation results of voltage dips - multiscalar control structure 4

4.5 Analysis of errors in power regulation

In Figures 4.33 – 4.38 the waveforms of active and reactive power, as well as the waveforms of percentage control errors for the proposed multiscalar control methods are collected. The following designations are used in all figures:

- MCS1 - multiscalar control structure 1;
- MCS2 - multiscalar control structure 2;
- MCS3 - multiscalar control structure 3;
- MCS4 - multiscalar control structure 4;
- s_p - stator active power;
- e_p - stator active power controller error, defined as $e_p = (P_{ref} - s_p) \times 100\%$
- s_q - stator reactive power
- e_q - stator reactive power controller error, defined as $e_q = (Q_{ref} - s_q) \times 100\%$.

Figure 4.33 shows the results of the error analysis for increasing the active power load. As can be seen, multiscalar control structure 2 has the smallest error (less than 1.5%) for $s_p = -0.3$. This method is also the fastest to reach the set value of active power. This method ensures an error for reactive power control of 2-2.5%, which is the highest error value among the analysed methods. Multiscalar control structure 1 is characterized by the highest overshoot in the transient state. Multiscalar control structures 3 and 4 are characterized by approximately the same dynamics and values of control errors.

Figure 4.34 shows the results of the error analysis for decreasing the active power load. As can be observed, multiscalar control structure 2 is the fastest to reach the set value of active power; but is characterized by highest oscillations. This method generates an error for reactive power control of 2-4%, which is the highest error value among the analysed methods. Multiscalar control structures 3 and 4 generate the smallest error when the active power setpoint is reached (less than 1%). These methods also generate smallest dynamic error for reactive power (less than 1.5%). Multiscalar control structure 1 is characterized by the highest overshoot in the transient state.

Figure 4.35 shows the results of the error analysis for increasing the reactive power load. As can be seen, all multiscalar control structures generate less than 2% regulation error for $s_q = -0.5$. Method 1 has the highest settling time (over 100 ms), methods 3 and 4 are characterised by the highest overshoots in transient states. It is worth noting that multiscalar control structures 3 and 4 provide the

best interference suppression in the second control subpath.

Figure 4.36 shows the results of the error analysis for decreasing the reactive power load. As can be seen, multiscalar control structures 2, 3 and 4 generate less than 1% regulation error for $s_q = -0.75$. Method 1 has the highest settling time (over 100ms) and steady state error of 2%. Methods 3 and 4 are characterised by the highest overshoots in transient states. It is worth noting that multiscalar control structures 3 and 4 provide the best interference suppression in the second control subpath while multiscalar control structure 1 provides the least robustness.

Figure 4.37 shows the results of the error analysis for speed change from subsynchronous to supersynchronous. As can be noted, multiscalar control structure 1 falls into undamped oscillations for both active and reactive powers after exceeding synchronous speed. The other three structures achieve a control error of less than 2%.

Figure 4.38 shows the results of the error analysis for grid voltage dips. As can be seen, all control structures responded correctly to the voltage dip. Multiscalar control structure 2 has the largest transient error, which reaches 150% for the change in active power and 60% for reactive power. Multiscalar control structures 3 and 4 achieve the smallest post-voltage dip control error of 1.5-2% for both active and reactive power control paths.

Despite errors in dynamic states, especially when investigating the behaviour of the system to the occurrence of voltage dips, the proposed control structures remained stable.

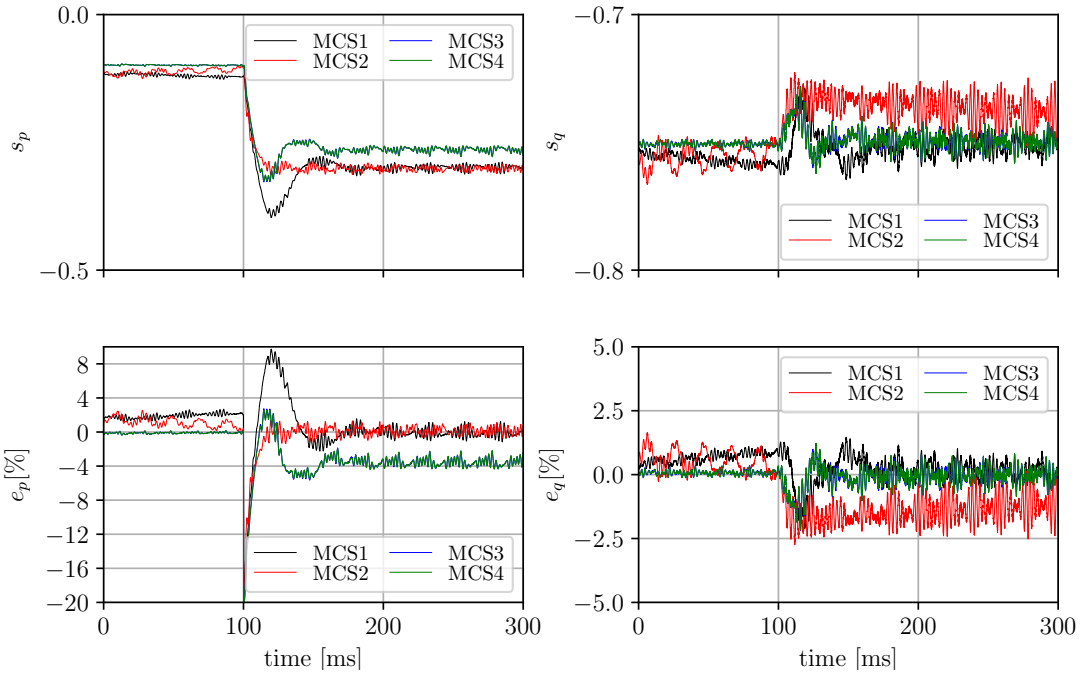

Figure 4.33: Control errors waveforms for changing active power from -0.1 to -0.3 p.u

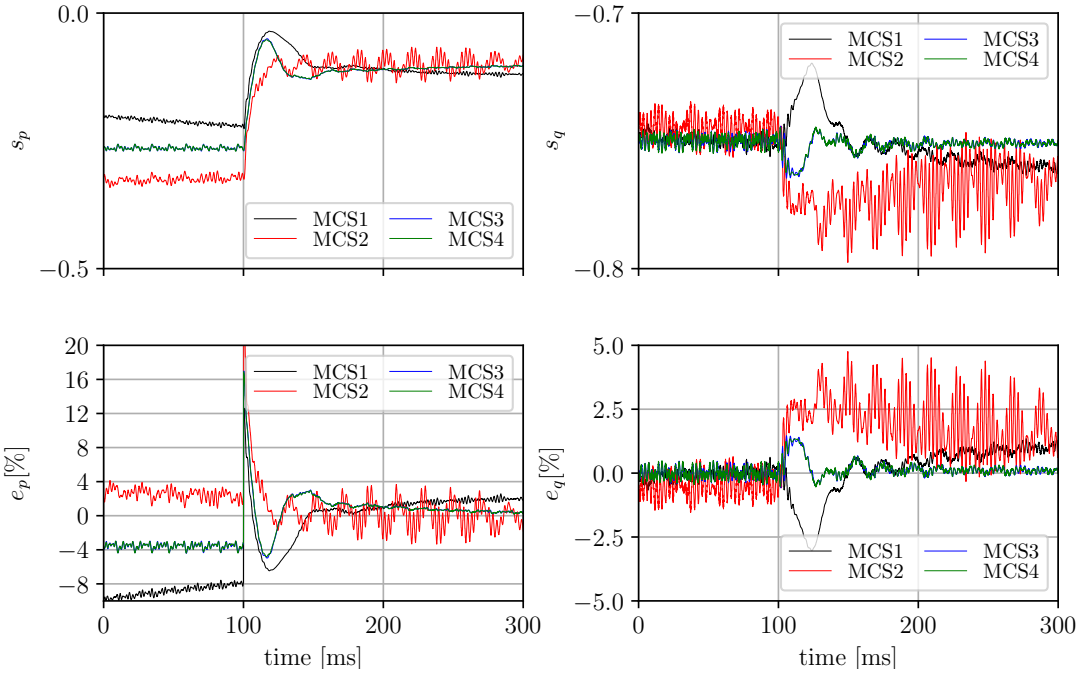

Figure 4.34: Control errors waveforms for changing active power from -0.3 to -0.1 p.u

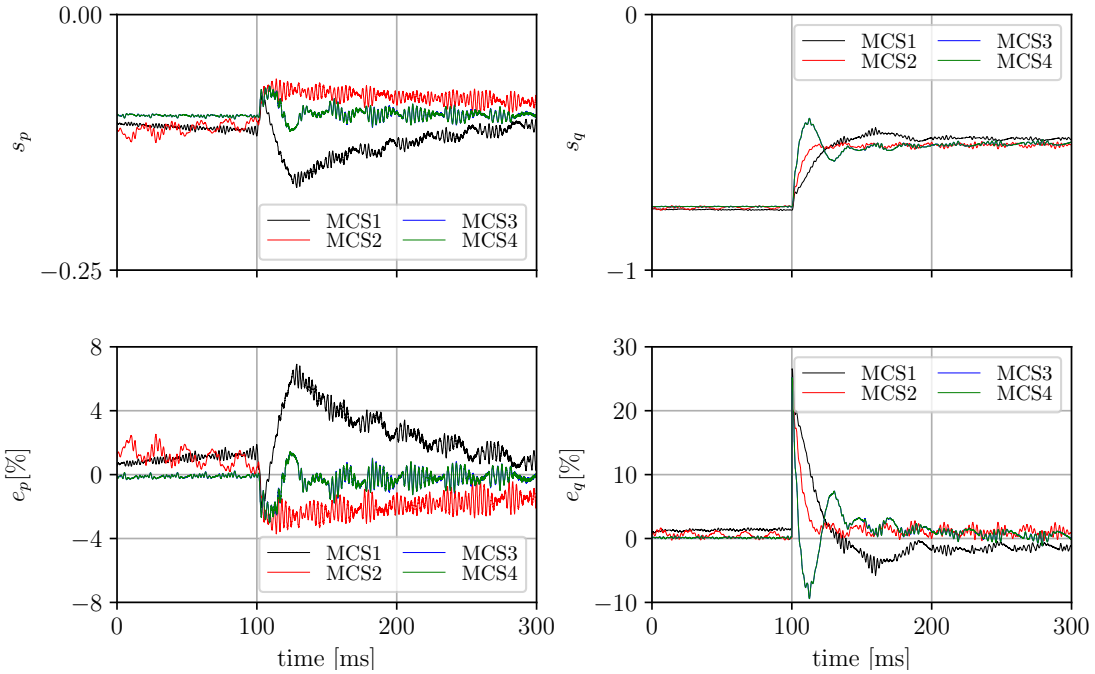

Figure 4.35: Control errors waveforms for changing reactive power from -0.75 to -0.5 p.u

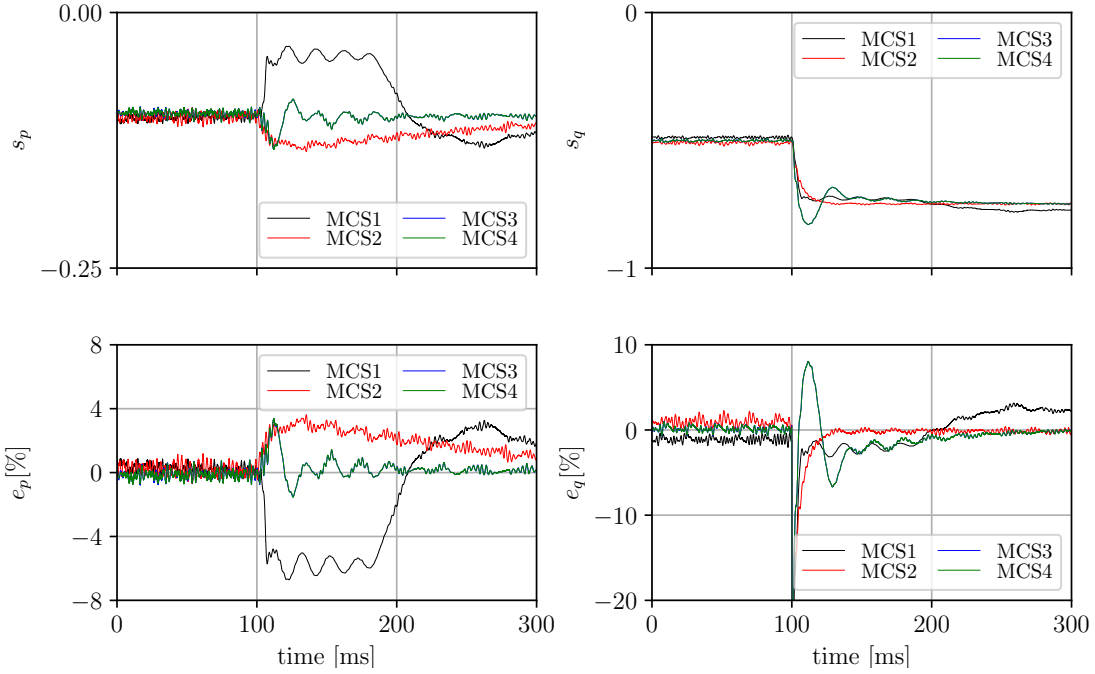

Figure 4.36: Control errors waveforms for changing reactive power from -0.5 to -0.75 p.u

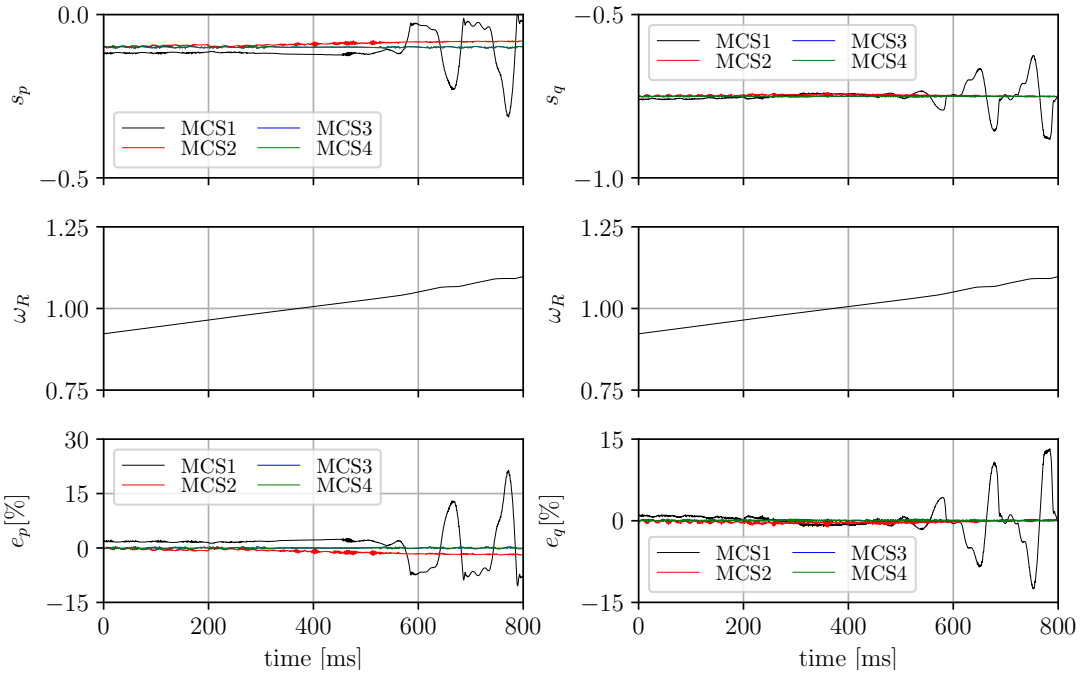

Figure 4.37: Control errors for crossing through the synchronous speed from 0.7 to 1.2 p.u

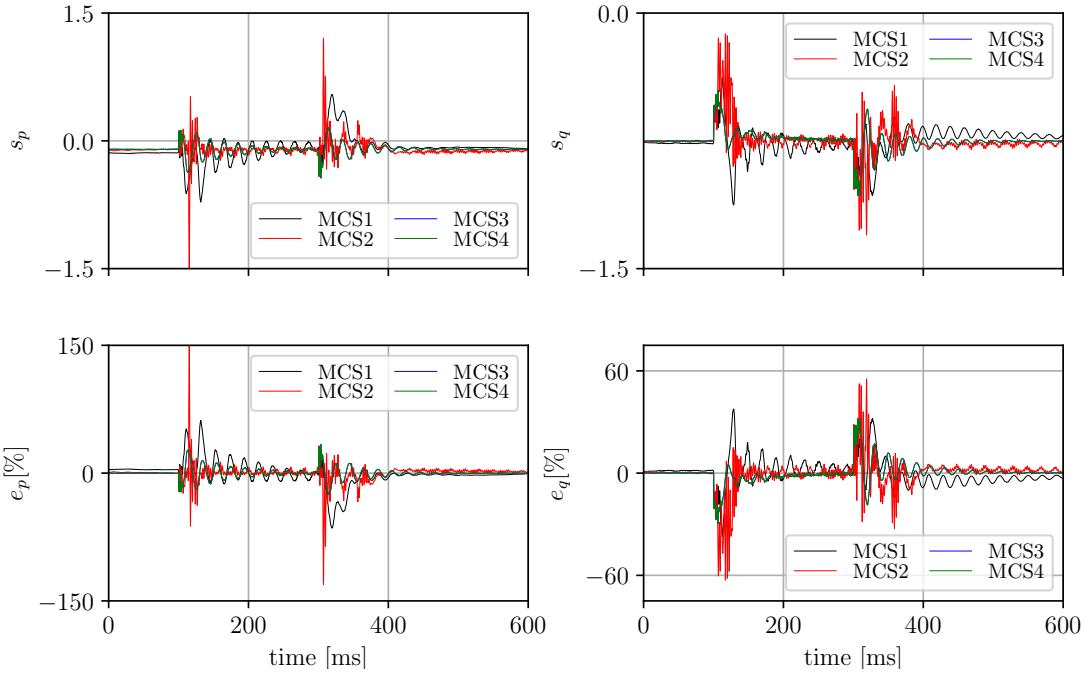

Figure 4.38: Control errors waveforms for voltage dips

Chapter 5

Experimental results

This section outlines the experimental investigation of the Doubly-Fed Induction Machine interfaced with the Current Source Converter (CSC); serving as validation for all theoretical assumptions and concepts. To begin, a brief introduction to the signal processing unit will be provided to highlight its software capabilities.

The signal processing unit provides an essential part in complete generator implementation. Unlike in simulations, where computing power is theoretically limitless, computations in the experimental setup are constrained by a strict execution time of $100\mu s$. Consequently, optimizing code and making time-saving compromises become crucial considerations.

As depicted in Figure 5.1, the computations and signal processing are partitioned between two subsystems. The Field Programmable Gate Array (Altera Cyclone II) manages communication between the computer console, memory, and Analog-to-Digital Converter (ADC). It is also tasked with driving the relays, transistor gate unit, and other components. The DSP (Analog Devices ADSP 21363) and the FPGA are interconnected through the address and data bus, facilitating data exchange between the integrated circuits.

FPGA provides the clock, as well as triggers, for the Digital Signal Processor (DSP) interrupt routine, in which calculations are executed. The initiation of the interrupt routine involves data exchange to the FPGA and processing of the collected data. It also monitors fault detection tasks. Next, depending on the selected control structure, the Field Oriented Control or one of the proposed multiscalar control is activated. Then, all necessary Space Vector Pulse Width Modulation (SVPWM) calculations are performed to determine the switching times for the desired currents.

All calculations are performed in the time period of less than 100 μs. Duration of the PWM vector is passed to the FPGA every 100 μs. Parameters for the control loops are detailed in Table A.3. Photographs of the Current Source Converter with the processing unit and generator system are presented in Appendix B.

The next sections will cover the presentation and evaluation of the experimental investigations performed in several generator conditions:

- changes of the reference active power - Section 5.1;
- changes of the reference reactive power - Section 5.2;
- changes of the rotor speed from under-synchronous to over-synchronous speed with constant reference active and reactive powers - Section 5.3;
- system behaviour during voltage dips - Section 5.4.

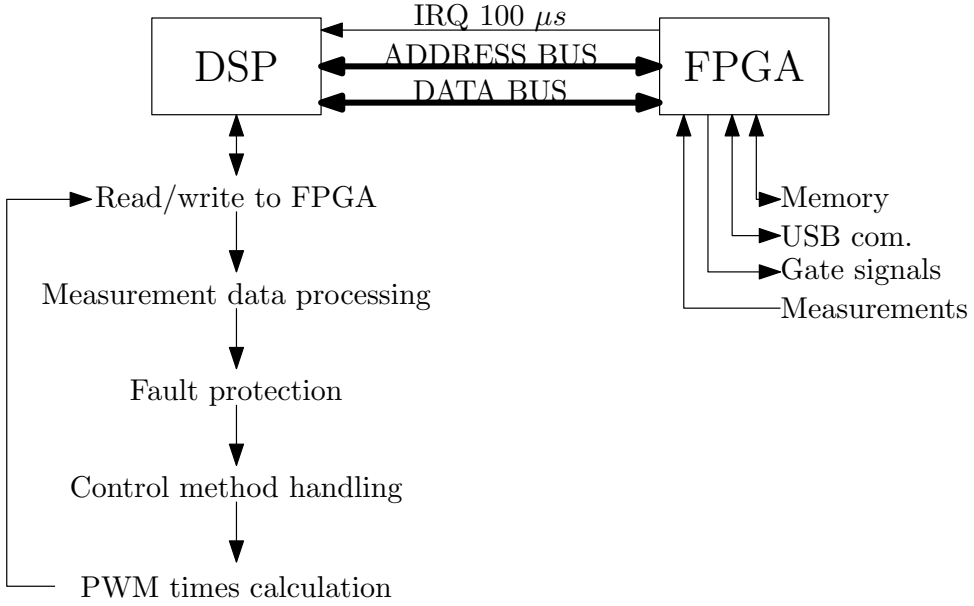

Figure 5.1: Flowchart of the Doubly-Fed Induction Generator connected to Current Source Converter simulation procedure

5.1 Control system behaviour during step changes of the reference active power

The performance of Doubly-Fed Induction Generator (DFIG) with Field Oriented Control (FOC), has been evaluated at the laboratory stand. As in simulations the control system operates with stator active and reactive powers as inputs. Mechanical speed is maintained at a constant 700 rpm (0.7 p.u.), providing a stable operational

baseline. The DC-link current is maintained based on the voltage e_d by additional PI. The testing procedure for the Doubly-Fed Induction Generator interfaced with the Current Source Converter is presented in Figures 5.2 and 5.3:

- at 400 ms the active power reference signal is set from -0.1 to -0.3 p.u. (left column in the figures);
- at 400 ms the active power reference signal is set from -0.3 to -0.1 p.u. (right column in the figures).

Figure 5.2 is separated into two columns where left groups results for increasing active power and right groups results for decreasing active power. Both display the waveforms of the rotor, stator and DC-link currents in reference to powers and mechanical angular speed. Both sides of Figure 5.3 show the waveforms of the rotor, stator voltages and DC-link voltage e_d in reference to powers and mechanical angular speed. Left column groups results for increasing active power and right - for decreasing power.

In both experiments, the system exhibits proper responses to step changes in active power. Due to low resolution of the registration (500 points per trace) in operator console waveforms of the powers have been filtered by Finite Impulse Response filters for presentation. As can be seen the Field Oriented Control is characterised by long transient states (about 150 ms), however it does not exhibit overshoots. There is the potential to reduce steady state fluctuations but such action would proportionally increase the time of transition states. In comparision to the simulations (Section 4.1), a coupling between active and reactive power is much less evident. In summary, the implemented control of the machine achieves desired dynamic response.

The subsequent control algorithm subjected to experimental research was the multiscalar control structure 1. As can be seen in Figure 5.4 and Figure 5.5, this approach exhibits notably reduced transient states (approximately 10 – 15 ms). However, this improvement comes at the cost of significantly heightened harmonic distortions in both current and voltage e_d within the DC-link. Additionally, it is observed that the rapid response of the active power control loop has an impact on the reactive power control loop, despite the utilization of decoupling methods.

Utilizing an alternative method, as outlined in Section 3.4 of this dissertation, has effectively mitigated high-frequency oscillations observed in both current and voltage e_d waveforms, as illustrated in Figures 5.6 and 5.7 respectively. Nonetheless, the

integration of this method into the generator system has led to prolonged transient periods and heightened occurrences of low-frequency oscillations following a state change.

Further refinements to the control and decoupling functions have facilitated the development of a structure capable of optimizing system response. Notably, the coupling between active and reactive powers has become negligible, while high-frequency oscillations in DC-link currents and voltages persist but have been significantly diminished. It is worth highlighting that the voltage e_d has been capped at 0.5 for safety considerations. Transient states duration are comparable to those achieved by the multiscalar control structure 1. Experimental results illustrating the performance of the aforementioned method are depicted in Figures 5.8 and 5.9.

Laboratory investigations validate both developed mathematical models and conducted simulations. All proposed multiscalar control structures respond correctly to a step change of active power.

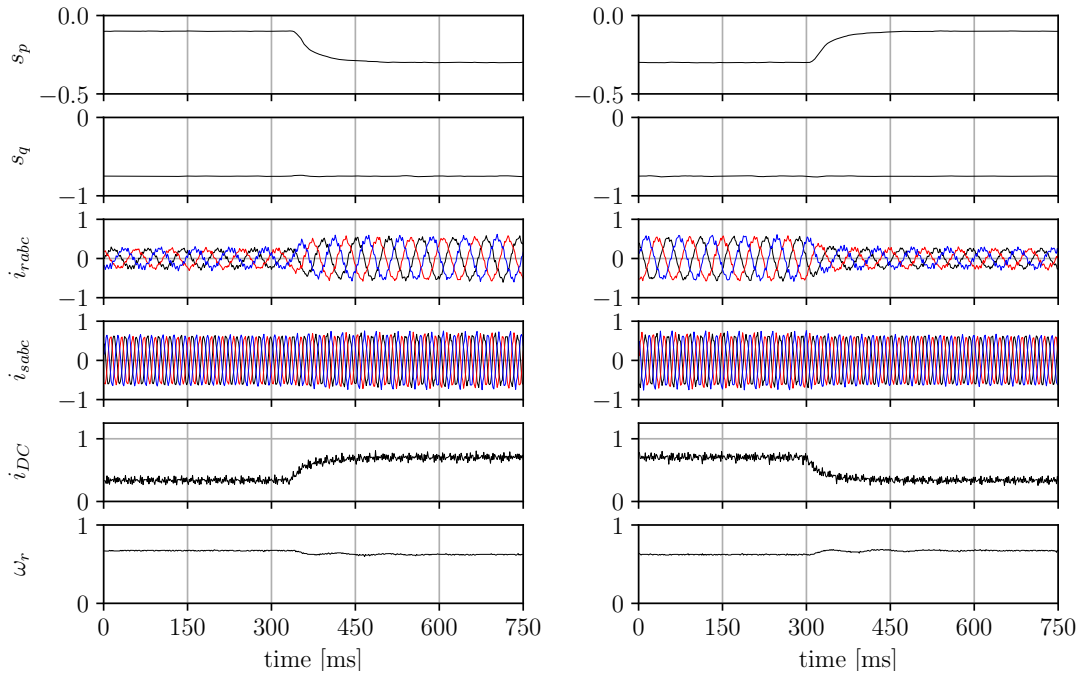

Figure 5.2: Experimental waveforms of currents during step changes of active power for Field Oriented Control

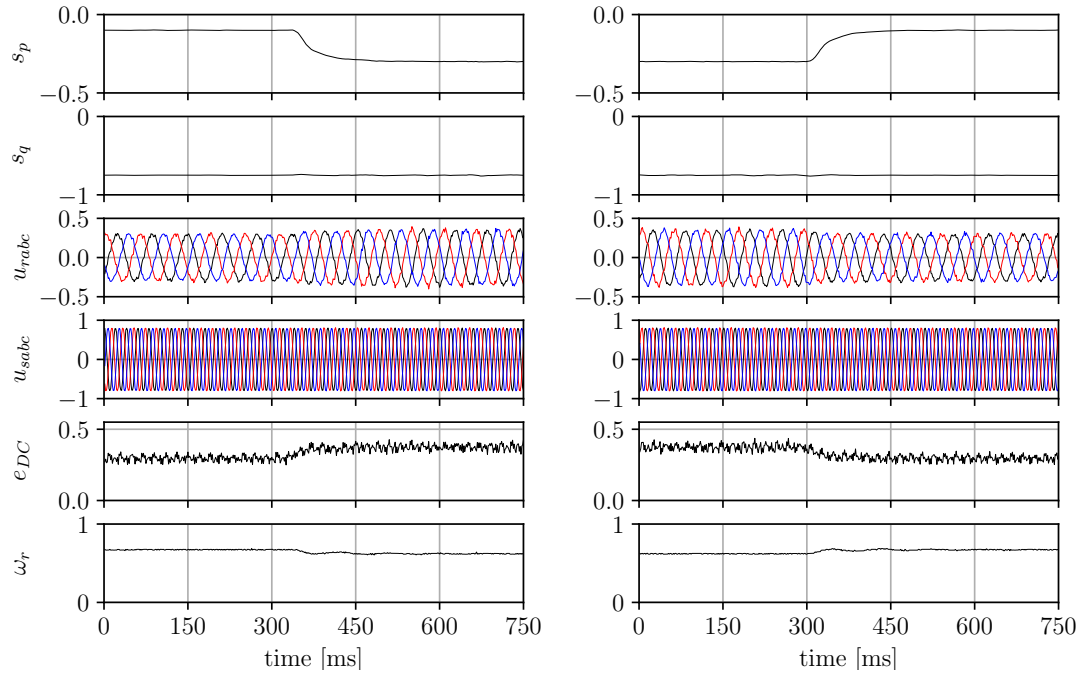

Figure 5.3: Experimental waveforms of voltages during step changes of active power for Field Oriented Control

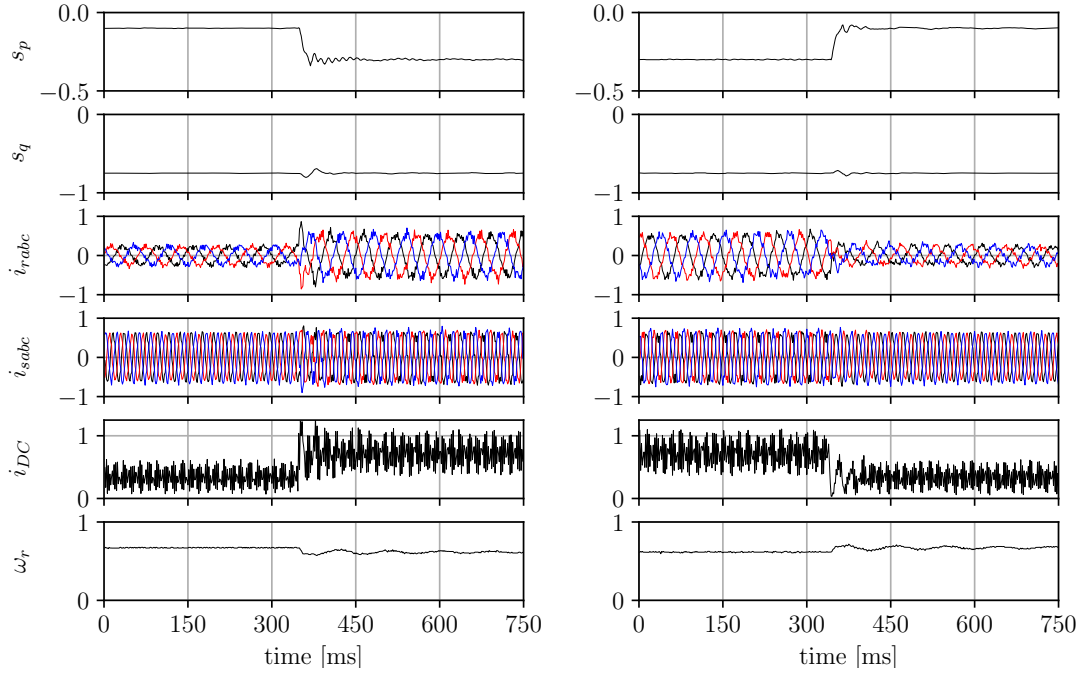

Figure 5.4: Experimental waveforms of currents during step changes of active power for multiscalar control structure 1

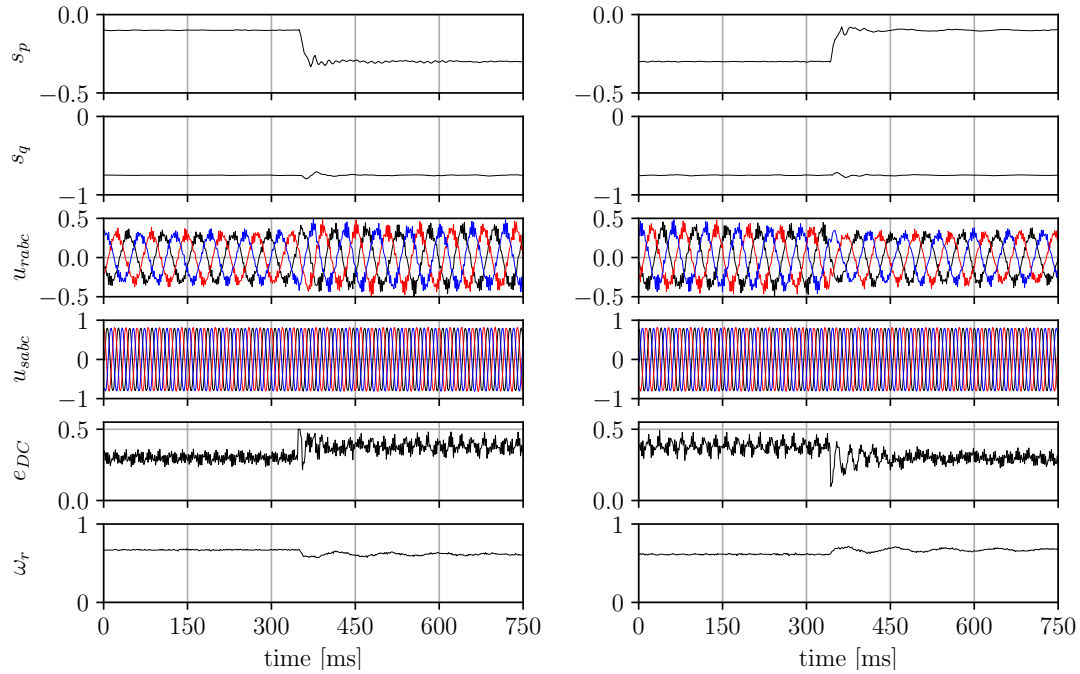

Figure 5.5: Experimental waveforms of voltages during step changes of active power for multiscalar control structure 1

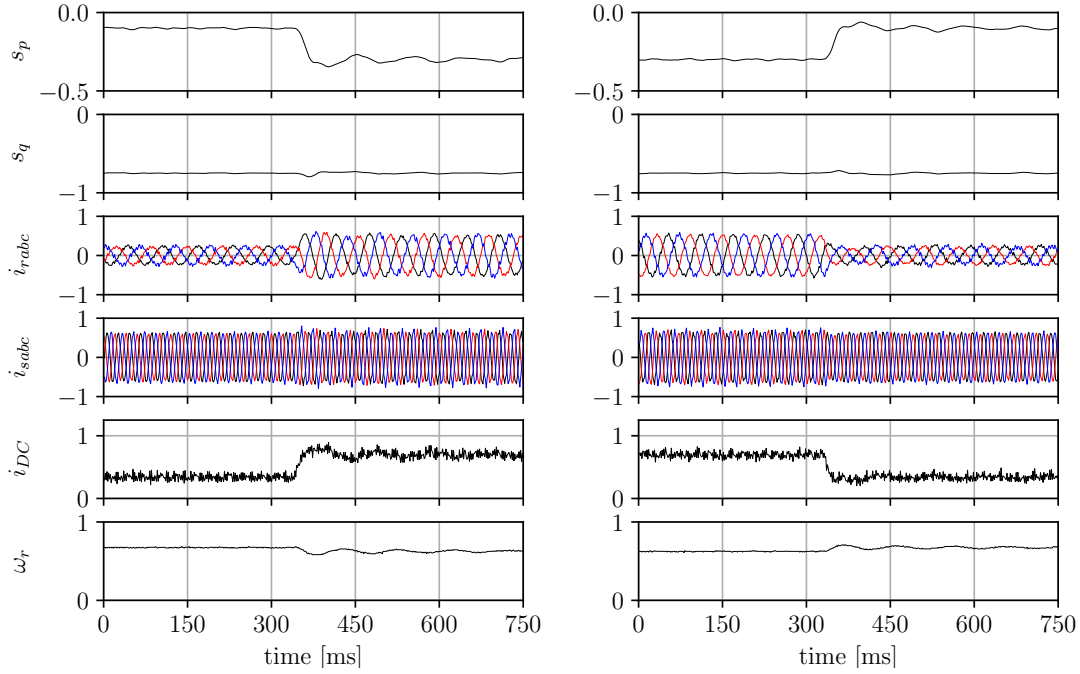

Figure 5.6: Experimental waveforms of currents during step changes of active power for multiscalar control structure 3

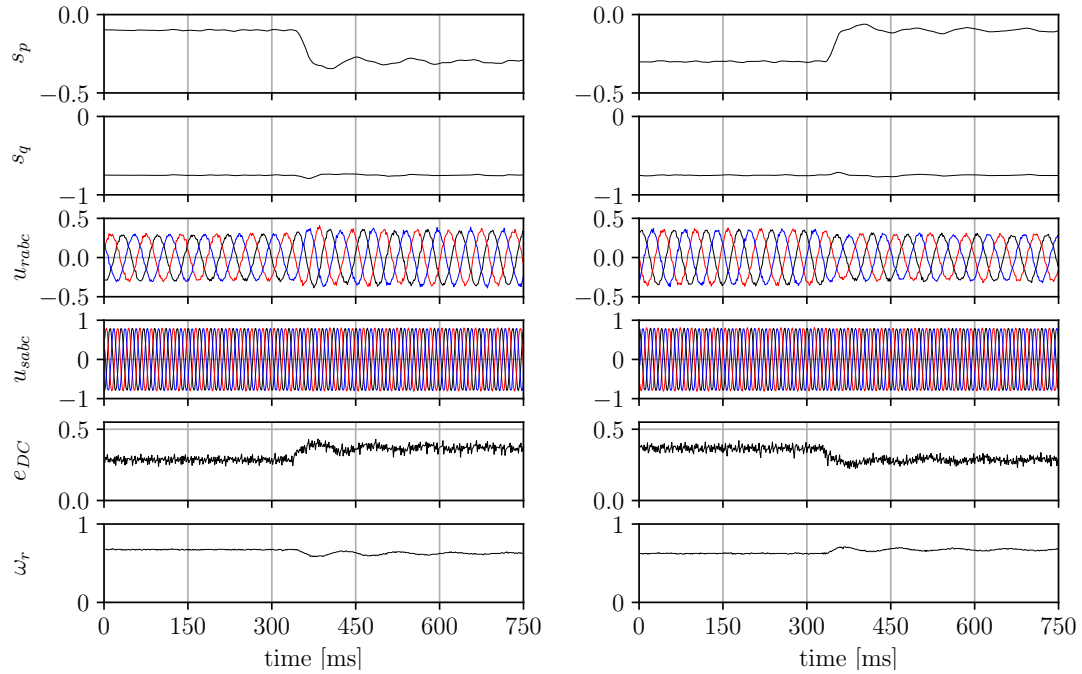

Figure 5.7: Experimental waveforms of voltages during step changes of active power for multiscalar control structure 3

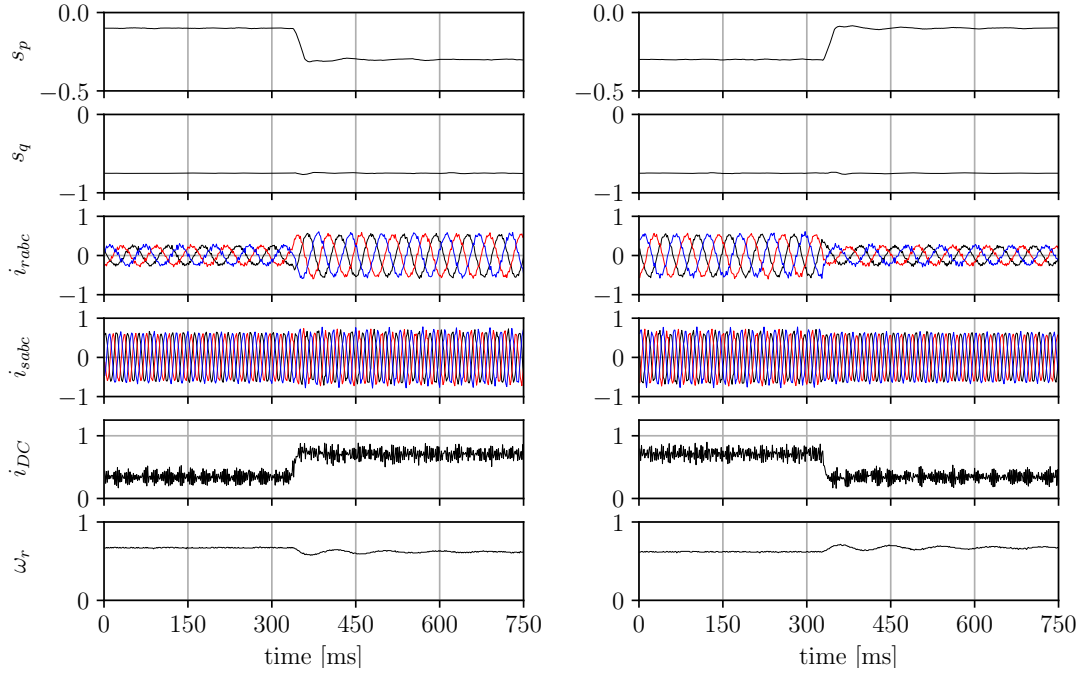

Figure 5.8: Experimental waveforms of currents during step changes of active power for multiscalar control structure 4

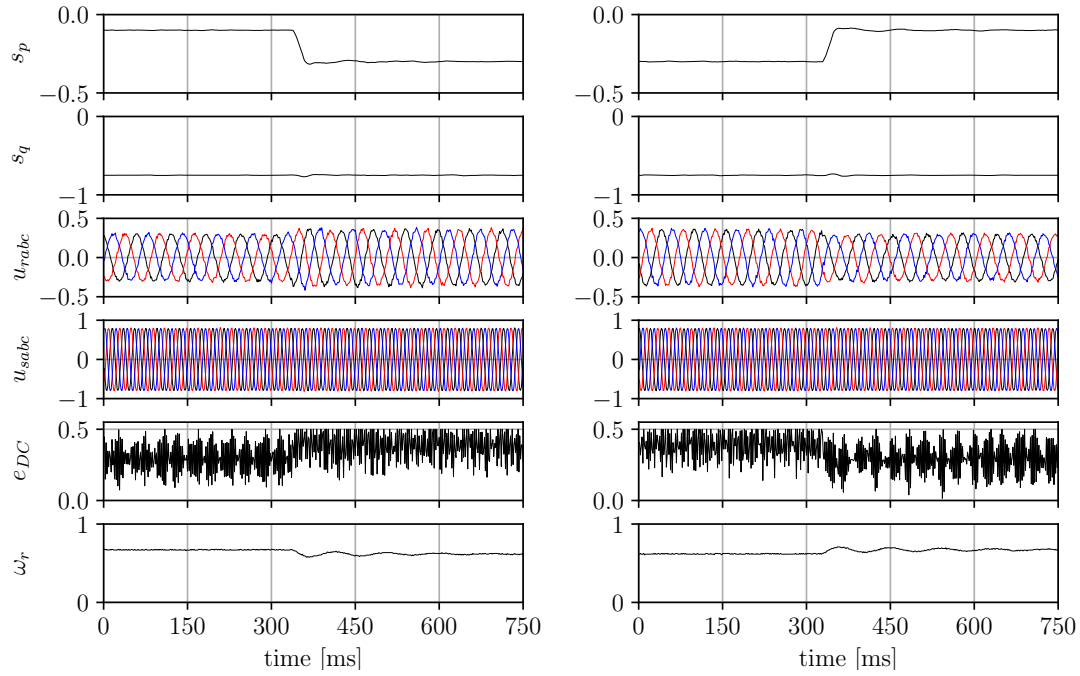

Figure 5.9: Experimental waveforms of voltages during step changes of active power for multiscalar control structure 4

5.2 Control system behaviour during step changes of the reference reactive power

Subsequently the performance of DFIG, for all control methods, under step changes of the reference reactive power has been investigated. The testing procedure is as follows:

- at 400 ms the reactive power reference signal is set from -0.75 to -0.5 p.u. (left column in the figure);
- at 400 ms the reactive power reference signal is set from -0.5 to -0.75 p.u. (right column in the figure).

Figures 5.10 – 5.17 are divided into two columns. In the left column, results are organized for increasing reactive power, while the right column showcases outcomes for decreasing reactive power. Each column features waveforms depicting the relationships between rotor, stator, and DC-link currents and voltages concerning powers and mechanical angular speed.

Figures 5.10 and 5.11 hold the results of Field Oriented Control tests. As can be

seen they show much better dynamic properties compared to active power changes maintaining minimal high-frequency fluctuations. Comparing to the simulation results presented in Section 4.2, a coupling between active and reactive power is much less evident. In summary, the implemented control of the machine achieves desired dynamic response.

Following, an experimental investigation was conducted on the multiscalar method 1 control structure. As can be seen in Figures 5.12 and 5.13, this approach exhibits comparable rise and fall times. However, heightened harmonic distortions in both current and voltage e_d within the DC link and additionally. Furthermore, it exerts a more pronounced effect on active power, despite the incorporation of decoupling functions.

The application of the subsequent method has mitigated high-frequency oscillations observed in both DC-link current and voltage e_d waveforms, as illustrated in Figures 5.14 and 5.15 respectively. However, longer transient periods are now evident. Furthermore, significant low-frequency oscillations in active power waveforms are present as response to step change. The developed decoupling functions have proven to be inadequate.

The subsequent control algorithm, implemented in the laboratory setup, has led to a significant enhancement in the characteristics of the tested energy conversion system. Results demonstrating the performance of this method are illustrated in Figures 5.16 and 5.17. The correlation between active and reactive powers has become negligible. Despite this improvement, high-frequency oscillations persist in DC-link currents and voltages, while transient states show comparable results to those obtained with the FOC method.

Laboratory investigations validate both the developed mathematical models and the conducted simulations. All proposed multiscalar control structures exhibit accurate responses to a step change in active power.

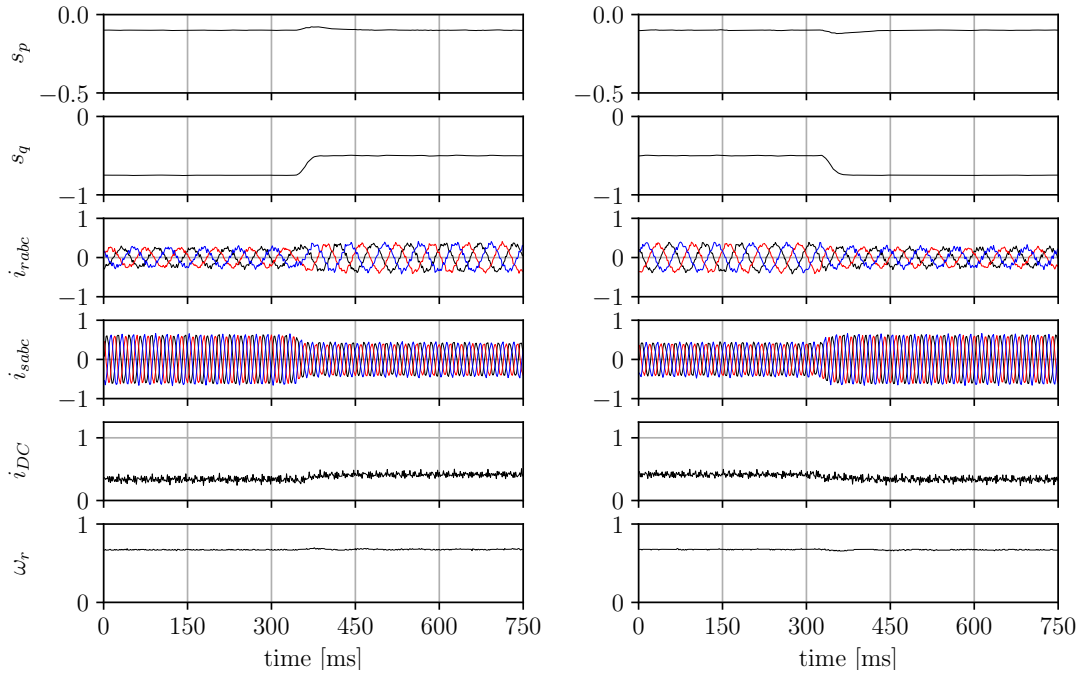

Figure 5.10: Experimental waveforms of currents during step changes of reactive power for Field Oriented Control

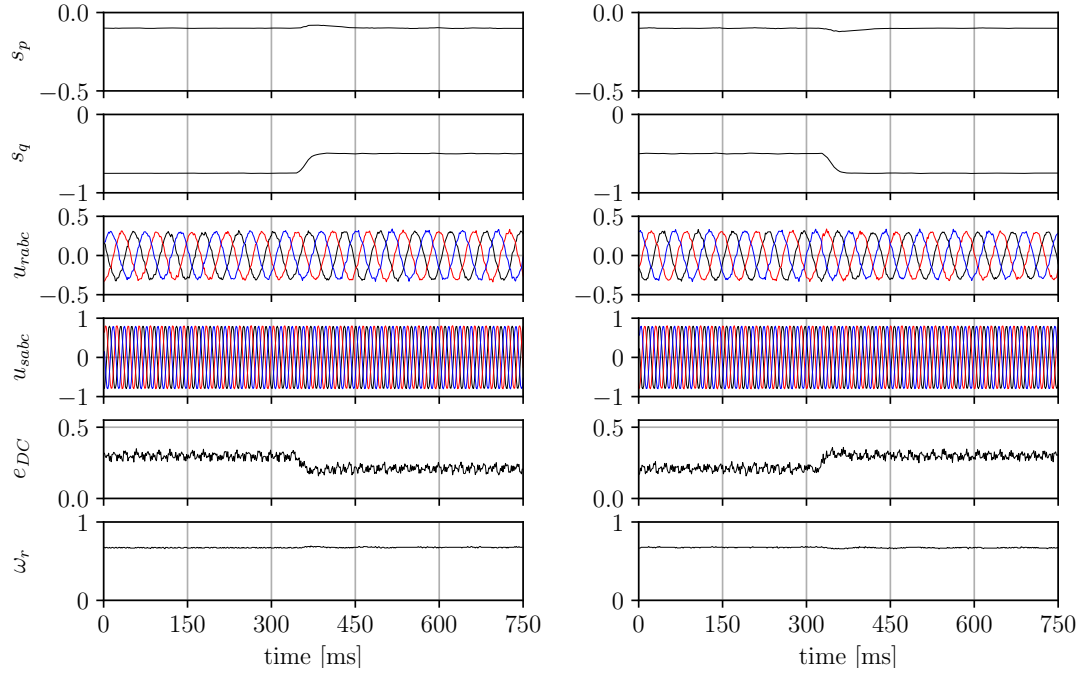

Figure 5.11: Experimental waveforms of voltages during step changes of reactive power for Field Oriented Control

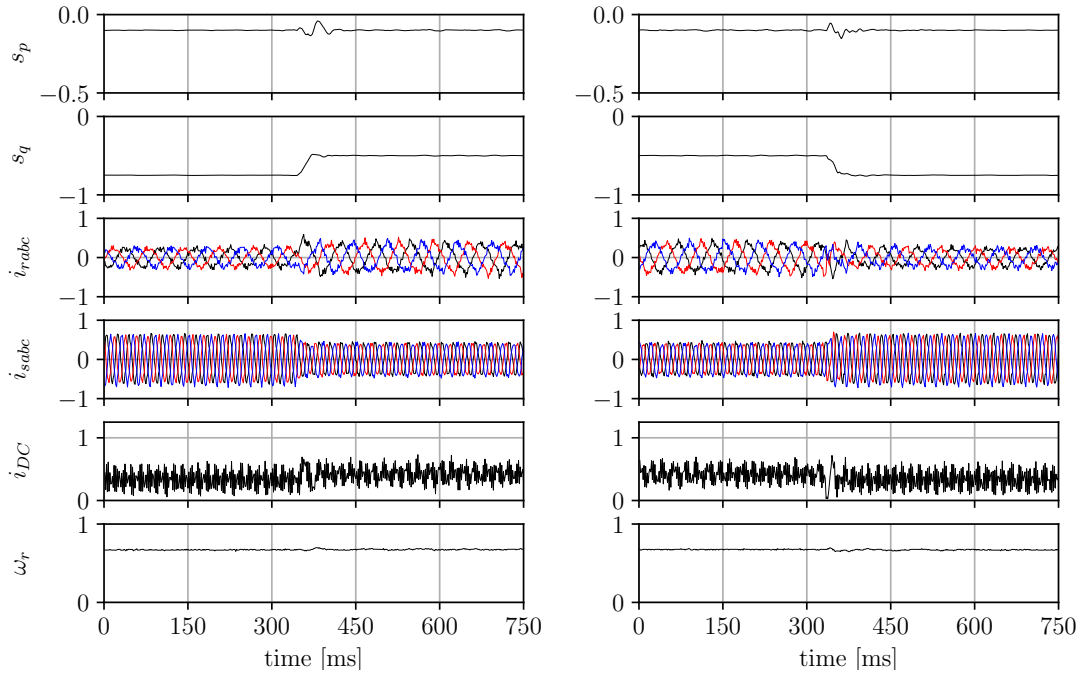

Figure 5.12: Experimental waveforms of currents during step changes of reactive power for multiscalar control structure 1

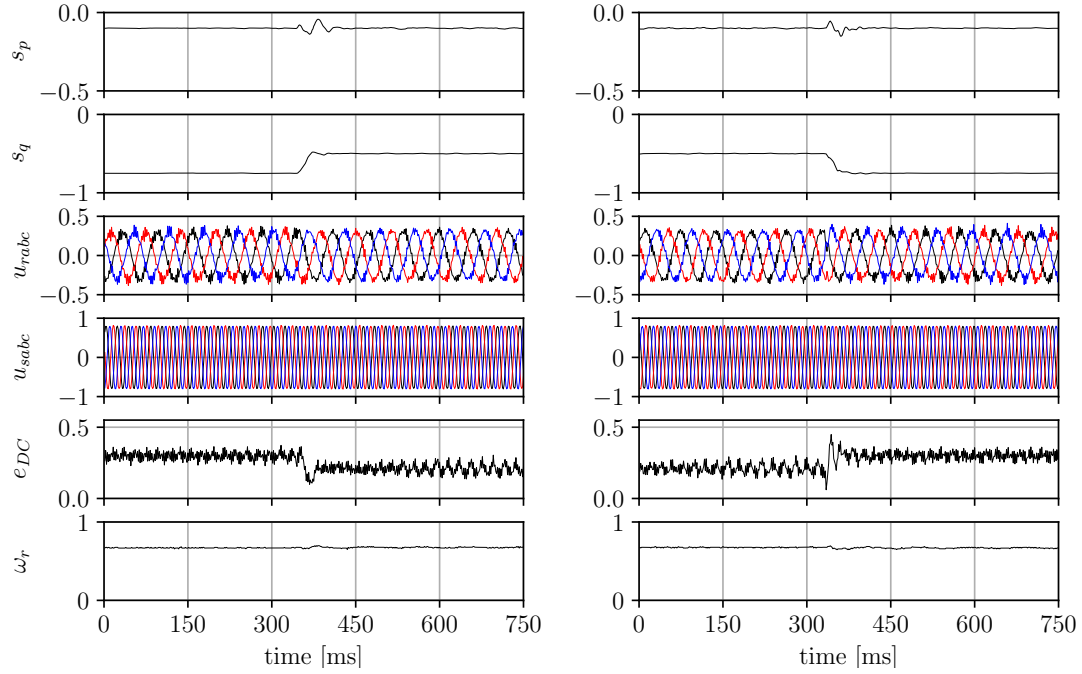

Figure 5.13: Experimental waveforms of voltages during step changes of reactive power for multiscalar control structure 1

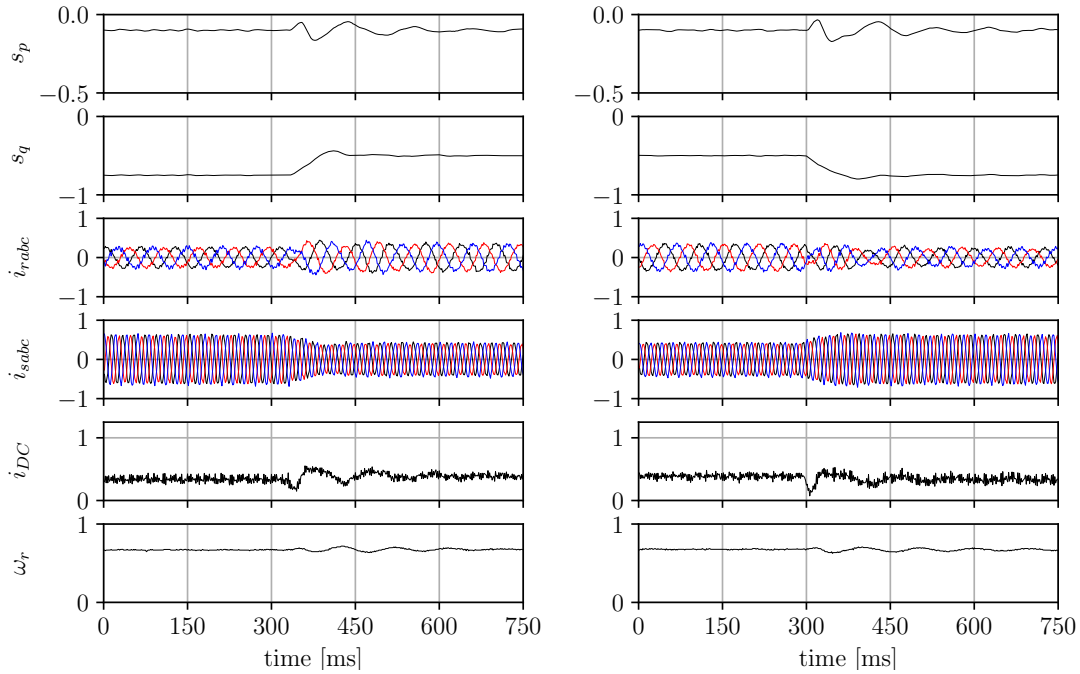

Figure 5.14: Experimental waveforms of currents during step changes of reactive power for multiscalar control structure 3

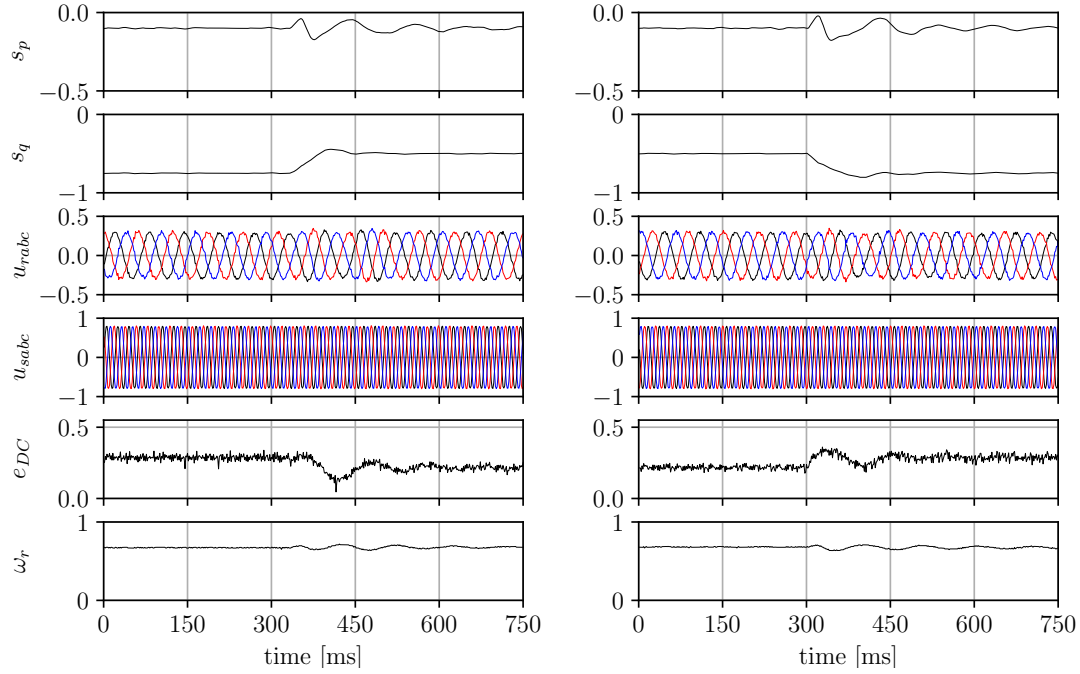

Figure 5.15: Experimental waveforms of voltages during step changes of reactive power for multiscalar control structure 3

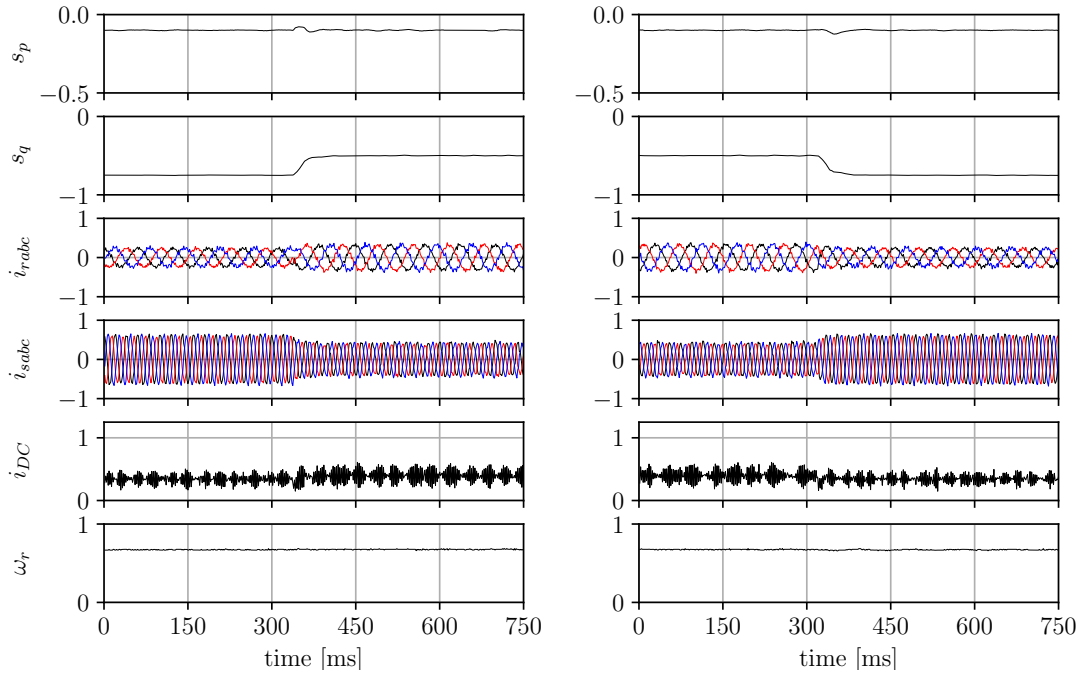

Figure 5.16: Experimental waveforms of currents during step changes of reactive power for multiscalar control structure 4

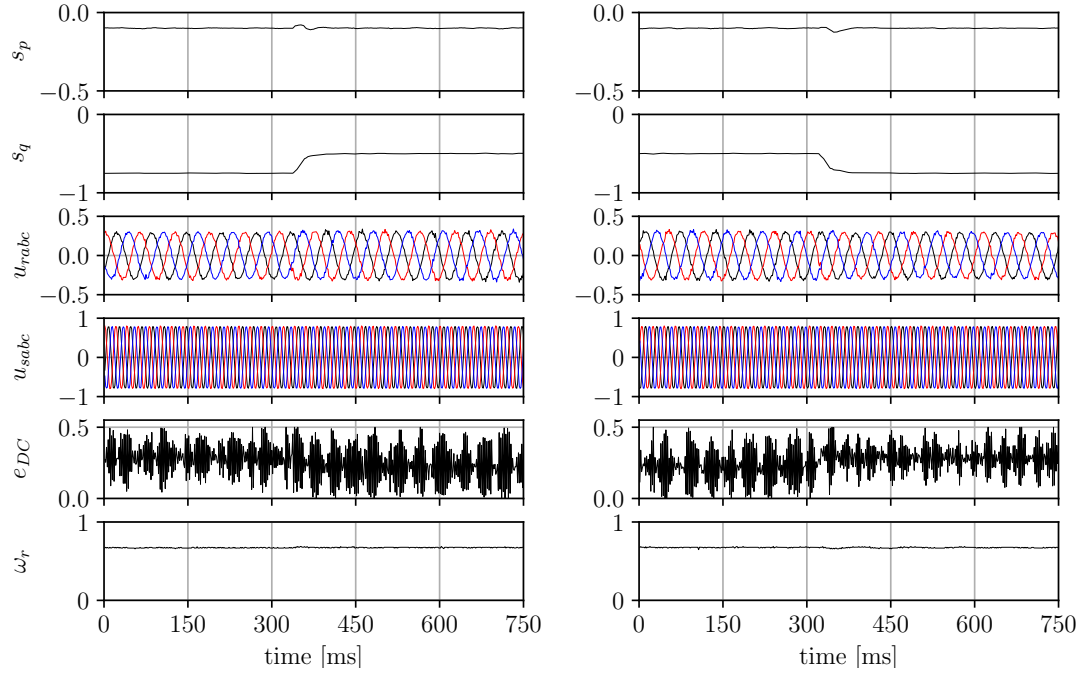

Figure 5.17: Experimental waveforms of voltages during step changes of reactive power for multiscalar control structure 4

5.3 Control system behaviour during changes of the rotor speed with constant reference powers

This experiment depicts an increase in propulsive torque resulting from higher wind speeds. The objective of the control systems is to sustain the desired levels of active power and reactive power across the entire range of torque/speed variations. Figures 5.18 – 5.21 display the waveforms of active power, reactive power, rotor currents, stator currents, rotor voltages, stator voltages and speed, recorded during the experiment at the laboratory bench. The torque variation is forced by a wind simulator consisting of a shaft-connected induction motor with a DFIG controlled from a commercial voltage inverter.

The testing procedure for changes of the rotor speed with constant reference powers is outlined as follows:

- active power is set and maintained at $s_p = -0.1\ p.u.$ during the experiment;
- reactive power is set and maintained at $s_p = -0.75 p.u.$ during the experiment;
- angular speed is changing from $\omega_r = 0.8\ p.u.$ to $\omega_r = 1.25\ p.u.$.

Observing the experimental results, it is evident that 3 out of 4 examined methods successfully cleared the laboratory assessments. The multiscalar control structure 1, as depicted in Figure 5.19, failed to go through synchronous speed. For the methods depicted in Figures 5.20 and 5.21, altering the sign of the decoupling functions became necessary upon surpassing synchronous speed. This adjustment was required due to the shift in the direction of electrical flow within the rotor.

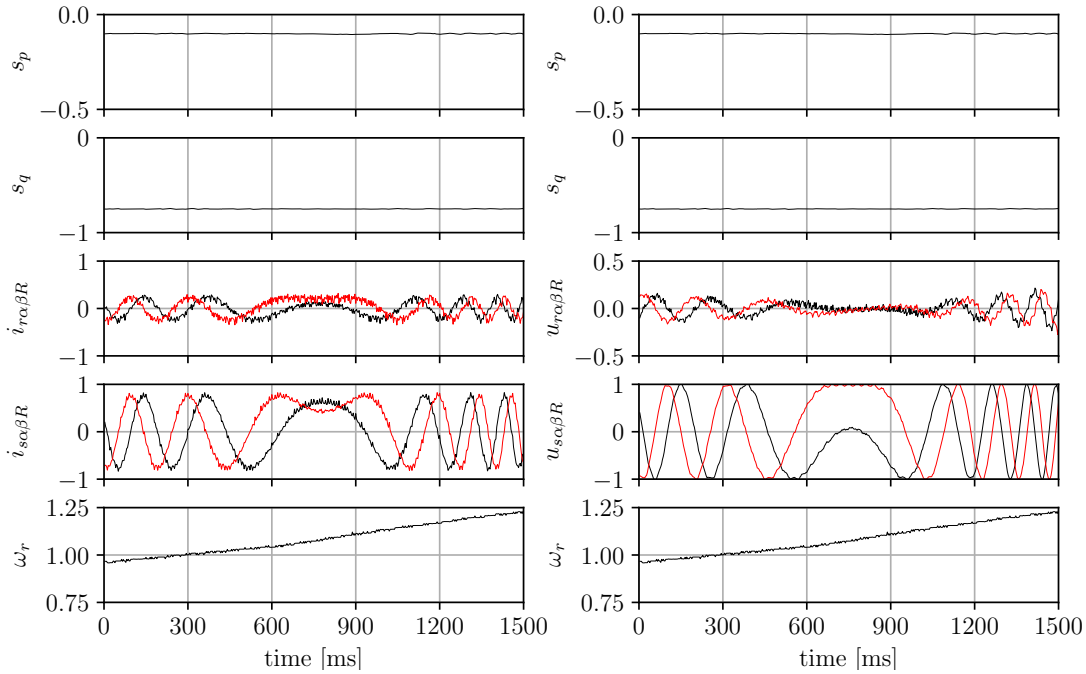

Figure 5.18: Experimental waveforms during change of speed from sub- to super-synchronous for Field Oriented Control

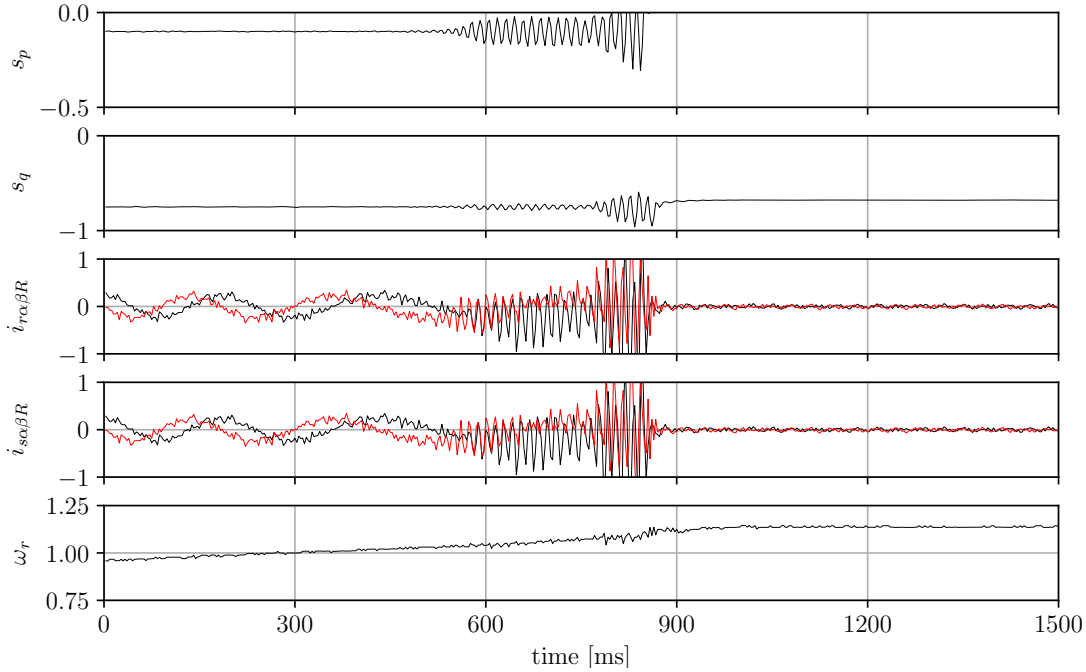

Figure 5.19: Experimental waveforms during change of speed from sub- to super-synchronous for multiscalar control structure 1

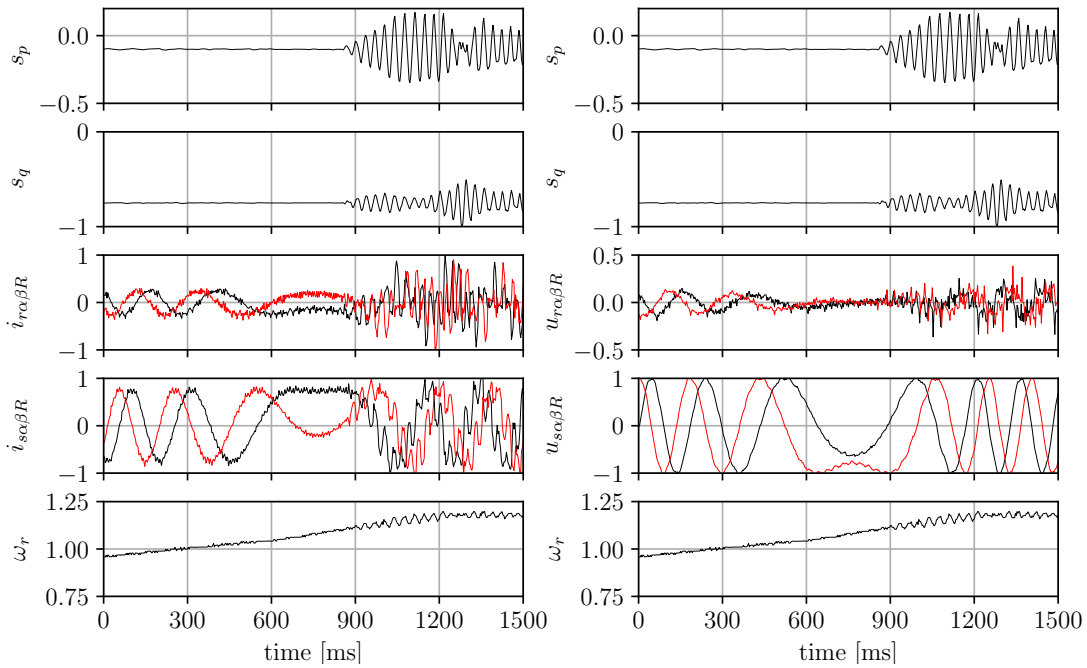

Figure 5.20: Experimental waveforms during change of speed from sub- to super-synchronous for multiscalar control structure 3

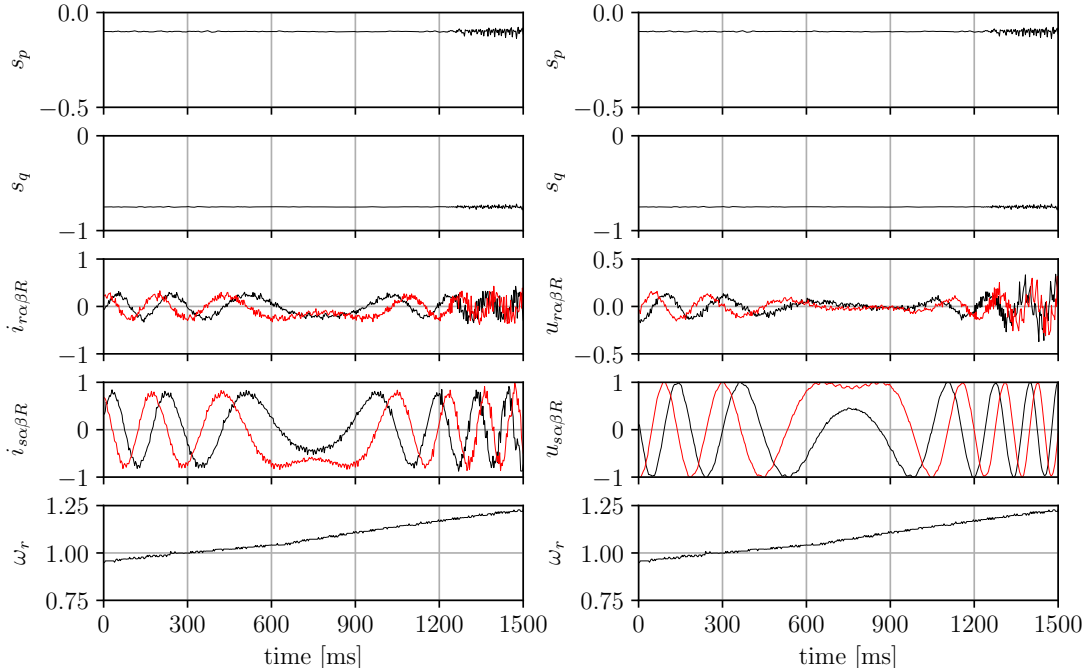

Figure 5.21: Experimental waveforms during change of speed from sub- to super-synchronous for multiscalar control structure 4

5.4 Control system behaviour during changes in grid voltage

In order to analyse the behaviour of control systems in laboratory conditions, a research stand was constructed, the diagram of which is shown in Figure 5.22. The voltage dip at the connection point of the DFIM to the power supply grid was realized by 3 phase adjustable, star-connected resistor. Changing the resistance made it possible to force voltage dips of various depths. Triggering the thyristor controller with pulses from the signal processor at a set time allowed for voltage dips of variable time.

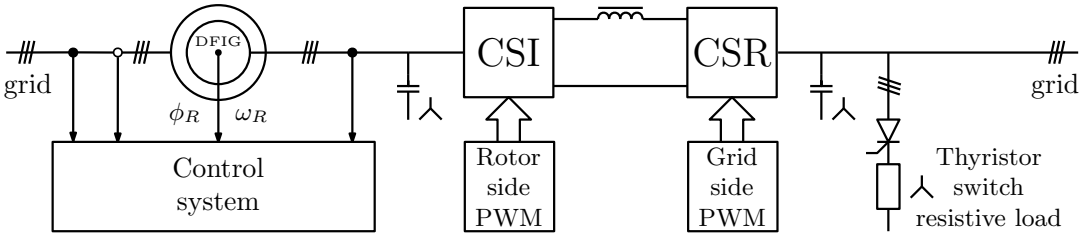

Figure 5.22: Block diagram of the test stand used to study the impact of grid voltage dips on DFIG operation

During the experiments, the rotational speed of the generator shaft and the set active power and reactive power values were assumed to remain constant. The PI controller gains for all methods remained the same as in the case of tuning for normal operating conditions.

Tests of individual control algorithms were carried out to determine:

- the impact of the dip depth and duration on the operation of the generator and control systems;
- the response of the proposed control structures to the grid voltage dip;
- the influence of control systems on the damping of output power oscillations.

Selected results obtained during laboratory measurements for individual CSC control systems are presented below in the form of graphs. Registration time, unless otherwise noted, in all cases was 250 ms.

Experimental results for Field Oriented Control are depicted in Figures 5.23 – 5.26. It is evident that this approach effectively restores its functionality with brief (up to 50 ms) and minor voltage dips. However, when dips exceed 50 ms or dip depth surpasses 80% of the grid voltage, undamped oscillations manifest in the waveforms

post-dip, which cannot be mitigated by this method. Despite these oscillations, the system remains operational. On the contrary, in the case of the multiscalar control structure 1, as illustrated in Figures 5.27 – 5.30, the system fully recuperates its functionality. Oscillations observed post-voltage dip are dampened by the applied decoupling functions.

In the laboratory setup, in contrast to simulation tests, an additional PI controller was implemented in the DC-link. The spikes evident in the i_{DC} waveforms are a typical response to the dynamically changing voltage e_d.

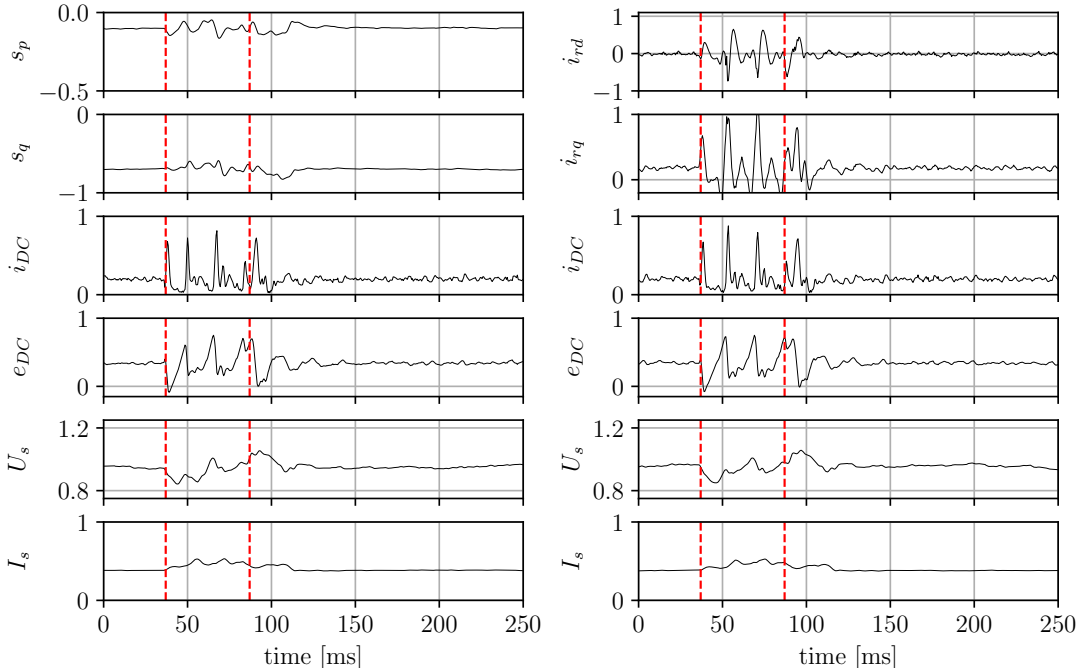

Figure 5.23: Experimental results of voltage dip to 80% of U_{sN}, 50 ms - FOC (the red lines indicate the duration of voltage dip)

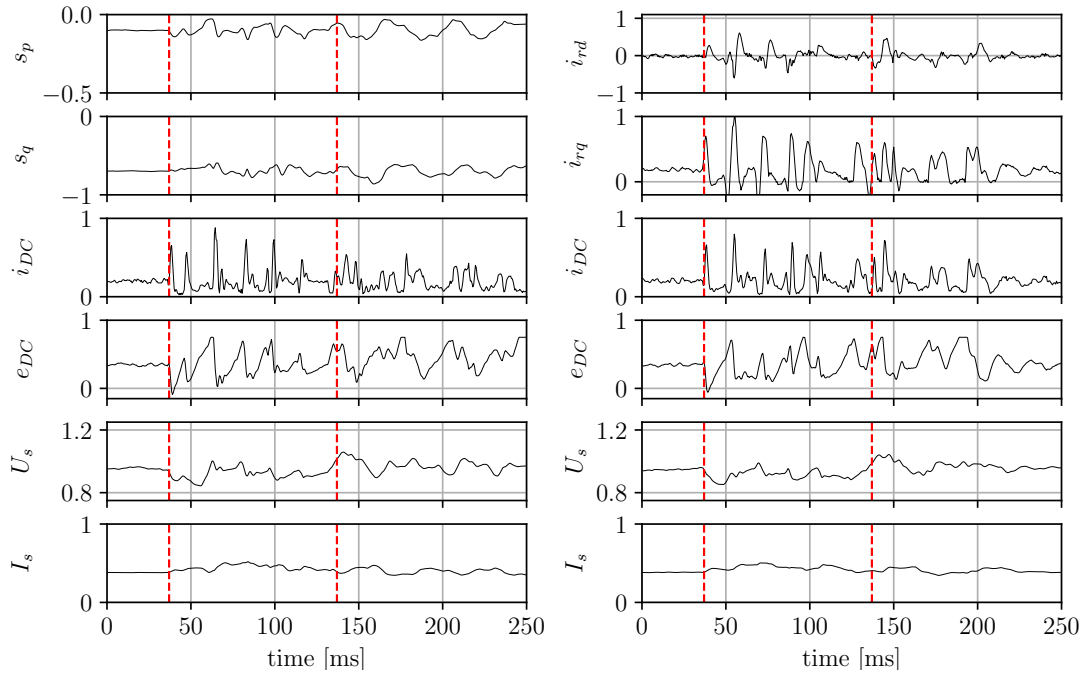

Figure 5.24: Experimental results of voltage dip to 80% of U_{sN}, 100 ms - FOC (the red lines indicate the duration of voltage dip)

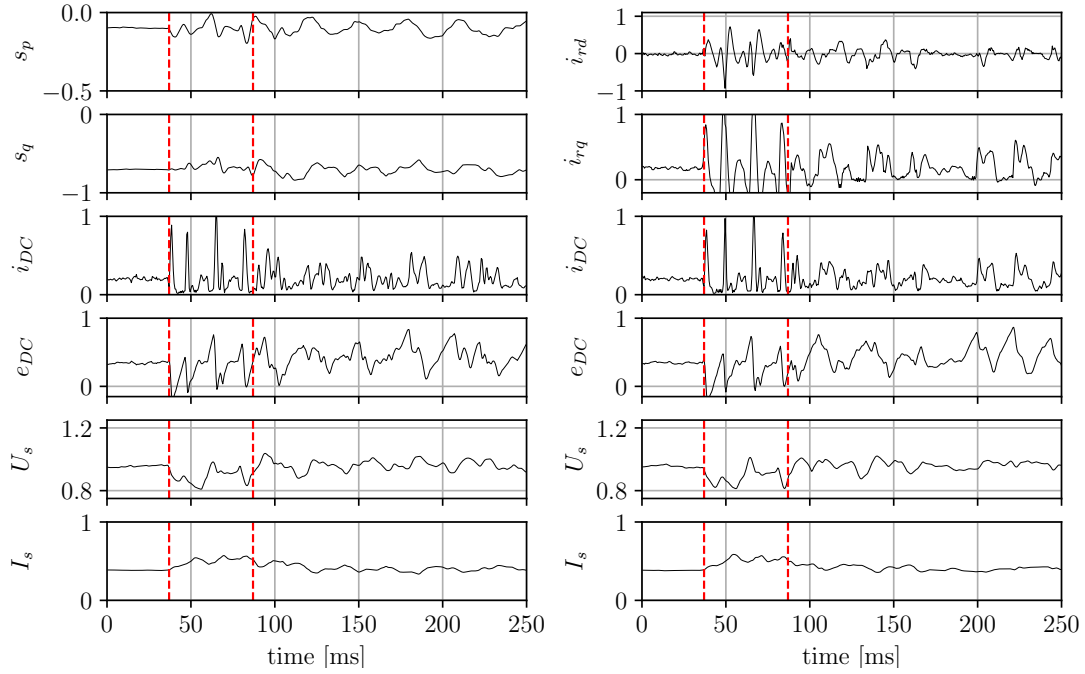

Figure 5.25: Experimental results of voltage dip to 75% of U_{sN}, 50 ms - FOC (the red lines indicate the duration of voltage dip)

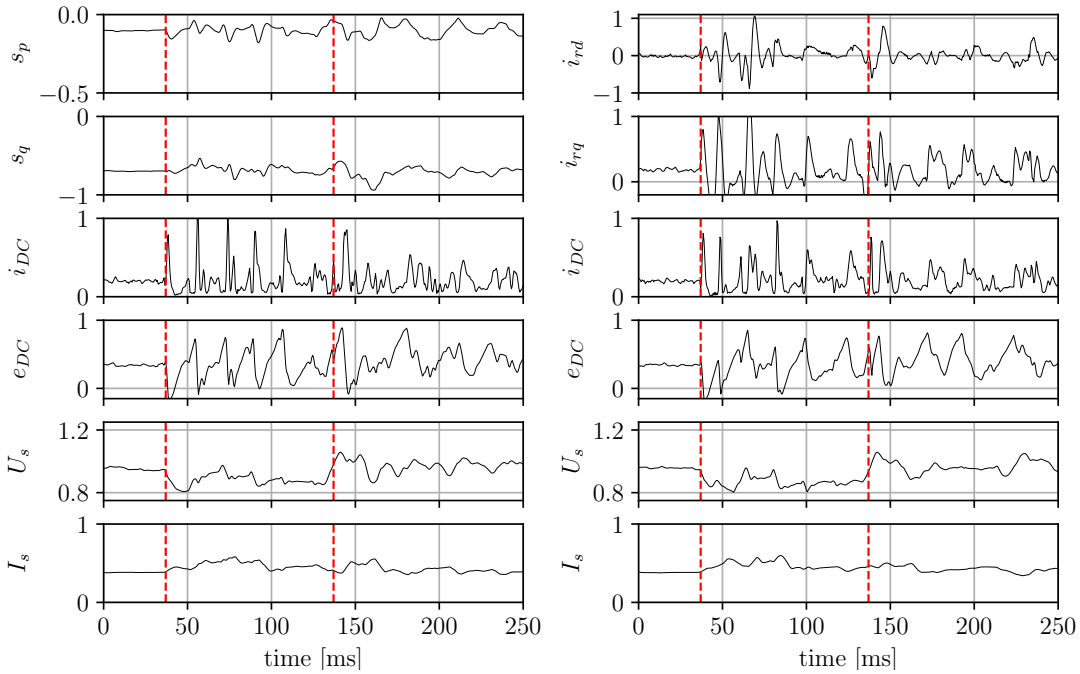

Figure 5.26: Experimental results of voltage dip to 75% of U_{sN}, 100 ms - FOC (the red lines indicate the duration of extortion signal)

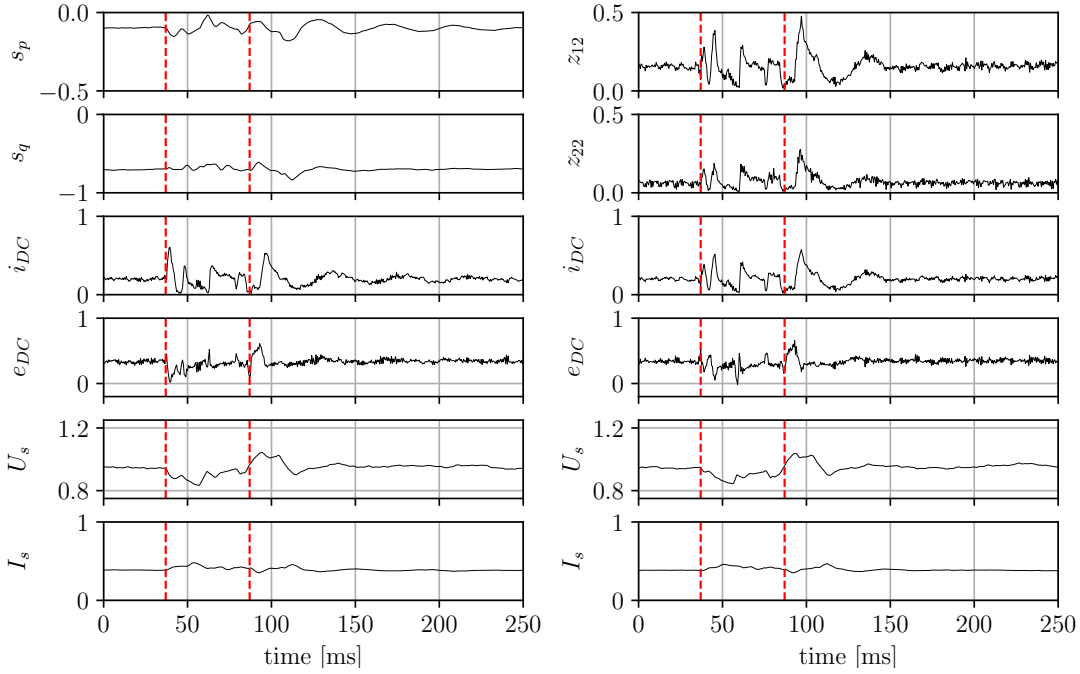

Figure 5.27: Experimental results of voltage dip to 80% of U_{sN}, 50 ms - multiscalar control structure 1 (the red lines indicate the duration of voltage dip)

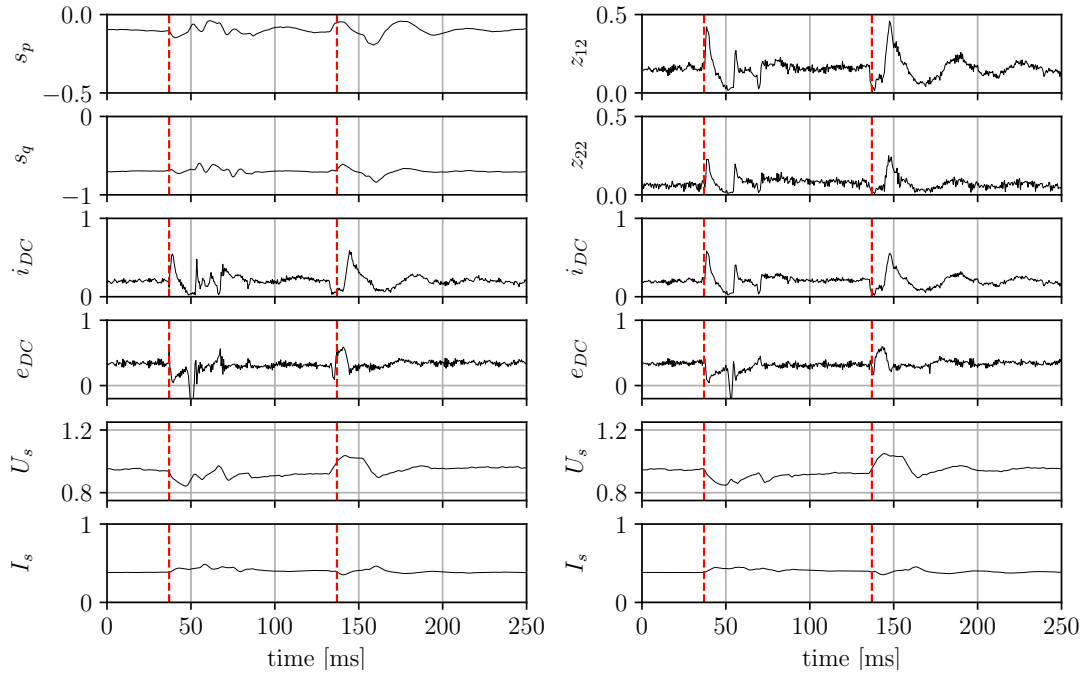

Figure 5.28: Experimental results of voltage dip to 80% of U_{sN}, 100 ms - multiscalar control structure 1 (the red lines indicate the duration of voltage dip)

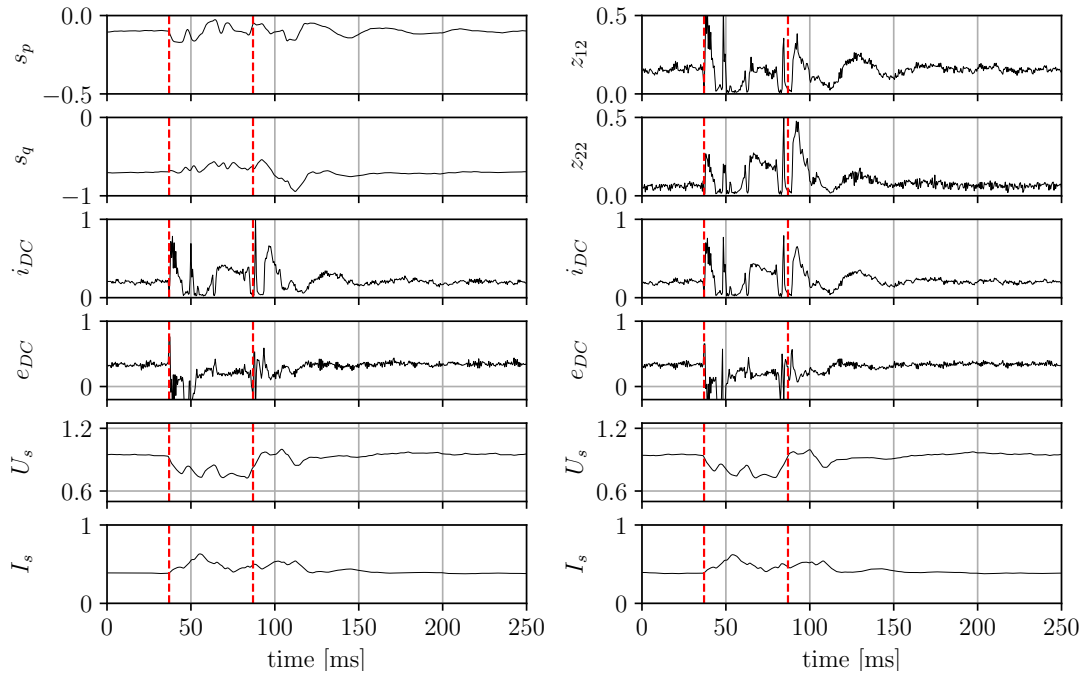

Figure 5.29: Experimental results of voltage dip to 70% of U_{sN}, 50 ms - multiscalar control structure 1 (the red lines indicate the duration of voltage dip)

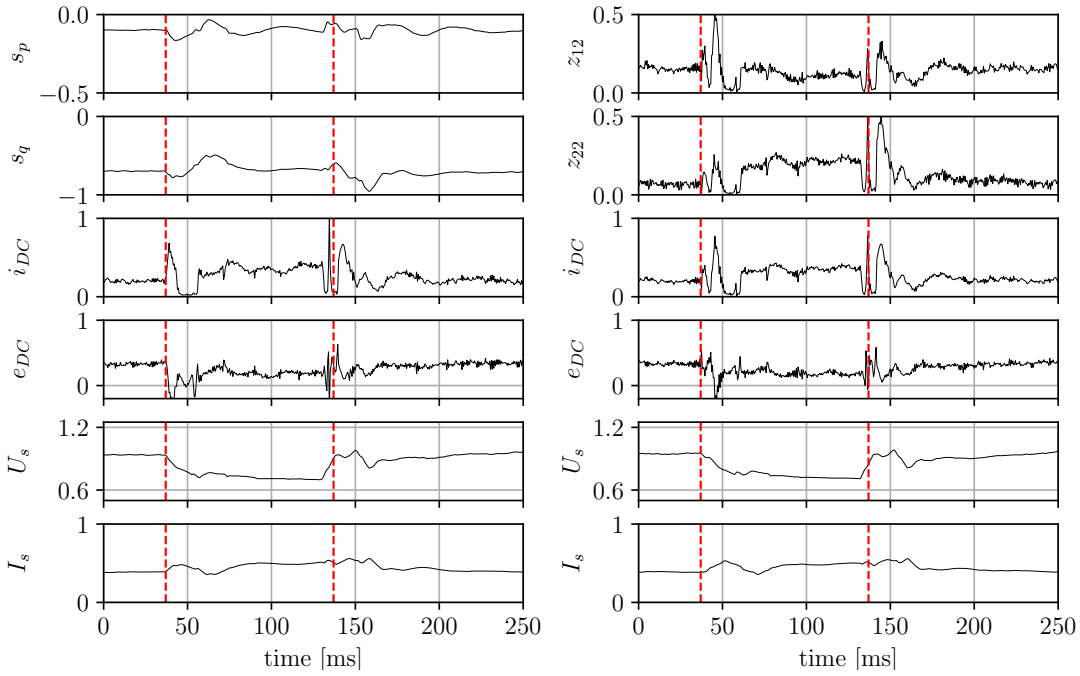

Figure 5.30: Experimental results of voltage dip to 70% of U_{sN}, 100 ms - multiscalar control structure 1 (the red lines indicate the duration of voltage dip)

5.5 System behaviour in steady state

This experiment depicts the normal operating conditions of a Doubly-Fed Induction Generator. The objective of the control systems is to sustain the desired levels of active and reactive powers which are $s_p = -0.1$ and $s_q = -0.75$. Figures 5.31 – 5.34 present oscillograms of current and voltage waveforms as well as their Fast Fourier Transform (FFT) analysis measured by Tektronix MSO3034 oscilloscope:

- Figure 5.31 shows oscillograms of stator voltage u_{sa} and FFT;
- Figure 5.32 shows oscillograms of stator current i_{sa} and FFT;
- Figure 5.33 shows oscillograms of rotor voltage u_{rab} and FFT;
- Figure 5.34 shows oscillograms of rotor current i_{ra} and FFT.

The rotor current and voltage harmonics visible in the FFT waveforms are due to the generator design and can be referred to as slot harmonics. Due to their occurrence, the generated current and rotor voltage waveforms are non-sinusoidal. Despite this, the control structures are resistant to interference from slot harmonics.

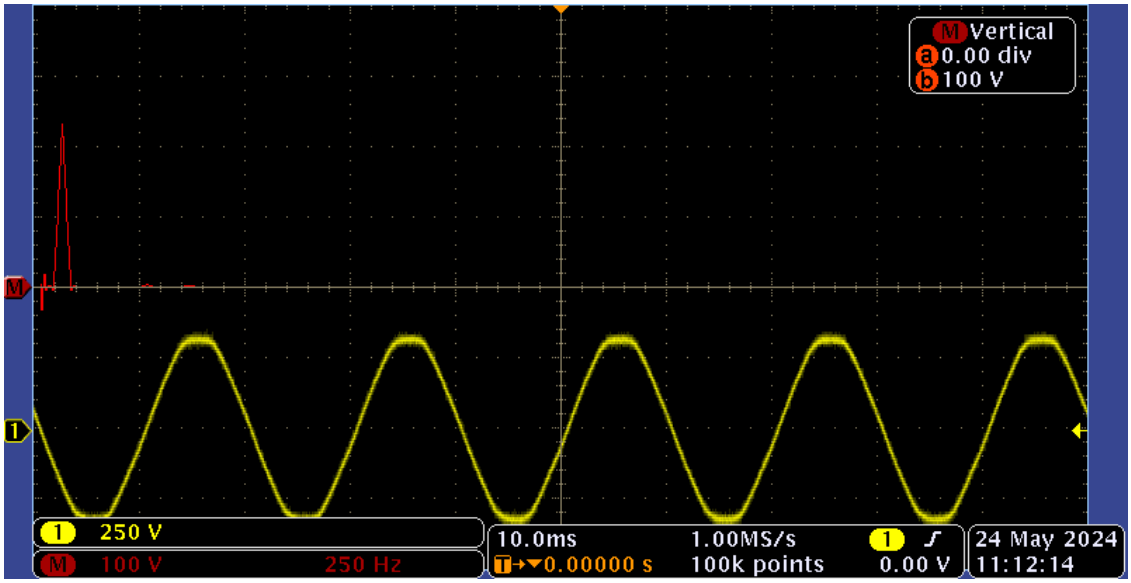

Figure 5.31: Stator voltage u_{sa} and FFT

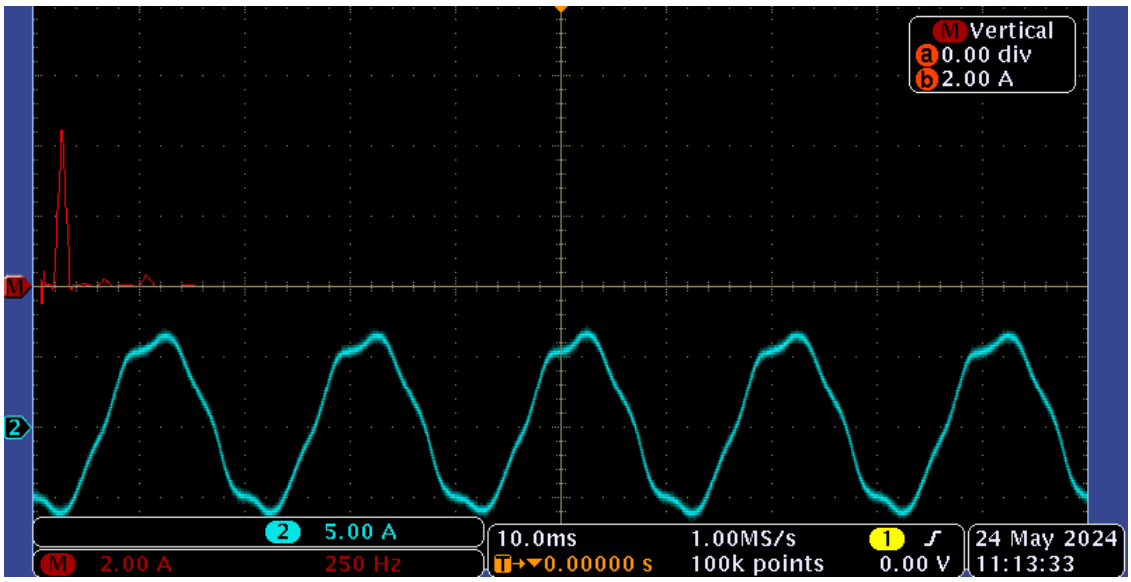

Figure 5.32: Stator current i_{sa} and FFT

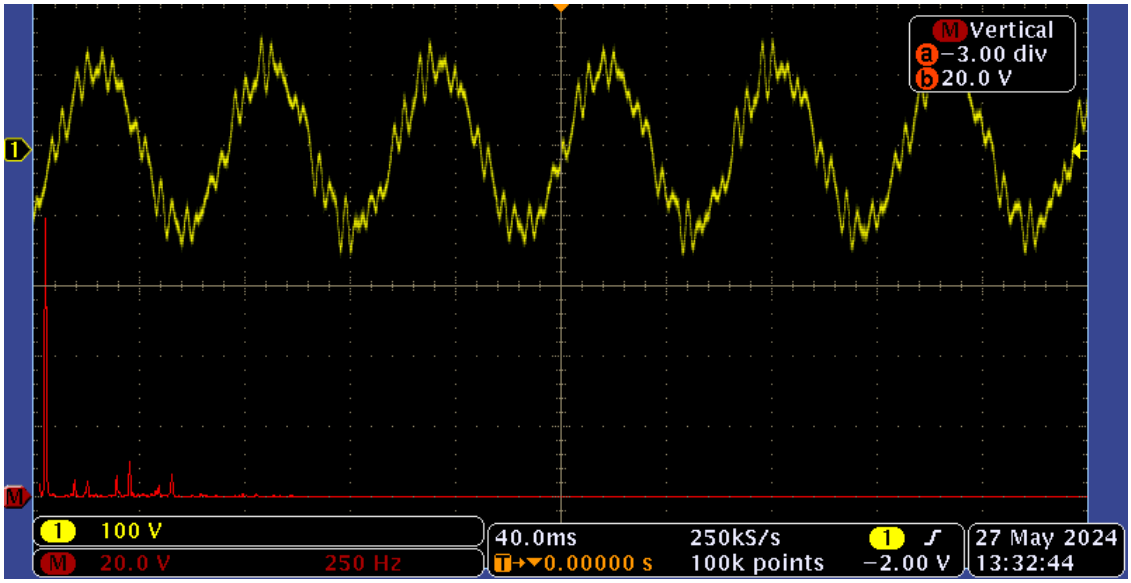

Figure 5.33: Rotor voltage u_{rab} and FFT

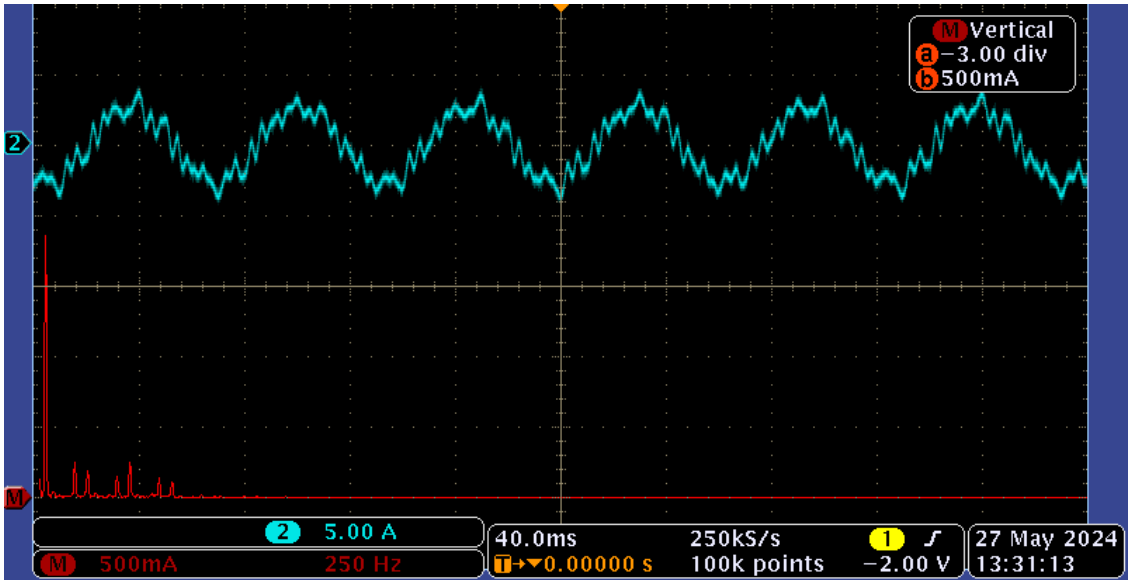

Figure 5.34: Rotor current i_{ra} and FFT

Conclusions

In this thesis, the control of two-level three-phase Current Source Converter interfaced with Doubly-Fed Induction Generator that operated in grid mode was considered. The proposed control structures facilitate independent control of variables, mitigate oscillations in both steady and transient states, and ensure robustness during grid faults.

Simulation and laboratory experiments were conducted to assess the response of DFIG supplied by CSC to step changes in active and reactive power, changes of the rotor speed, as well as to supply voltage disturbances in the form of voltage dips of various depths and duration. Five different power control structures for DFIG were tested, utilizing dependencies of multiscalar DFIG models to synthesize three nonlinear control systems. Additionally, a simulation program was developed to facilitate testing of the proposed regulatory structures.

Proposed multiscalar control structures 1, 3 and 4 (described in Sections 3.2, 3.4 and 3.5 respectively) were deployed on a laboratory setup to evaluate their dynamic characteristics, allowing for subsequent comparison and analysis. Multiscalar control structure 2, due to its computational complexity, has been analysed only in simulation studies. The most important conclusions obtained on the basis of simulation and laboratory tests:

- the developed structures of control systems enable independent regulation of active and reactive power DFIG under normal generator operating conditions;
- the proposed DFIG power control systems with nonlinear multiscalar control are characterized by good dynamic properties such as response times below 75 ms for changes in active and reactive powers;
- due to a more complex control structure than the FOC the best properties of damping oscillations in the generator output power waveforms are characterized by the control system with nonlinear multiscalar control

described in Section 3.5;

- in case of a shallow dip, the proposed power control systems enable control of rotor currents, but their effectiveness depends on the depth of the dip;
- in case of a deep voltage dip, it is necessary to use additional protection circuits for Current Source Converter on the rotor side - an example is a supplementary energy storage system connected to DC-link by a bridge converter and switched on for the duration of the dip. This system would function as a temporary power source.

Nevertheless, the configurations of power control system topologies for Doubly-Fed Induction Generator outlined by the author do not comprehensively explore the potential for synthesizing novel control systems utilizing multiscalar models. The control system configurations outlined in the thesis serve as a foundation for future investigations of poly-phase DFIG systems which are currently investigated at the Gdańsk University of Technology.

Bibliography

[1] C. Kumar, A. Sarma, and P. Prasad, "Fuzzy logic based control of wind turbine driven squirrel cage induction generator connected to grid," in *2006 International Conference on Power Electronic, Drives and Energy Systems*, pp. 1–6, 2006.

[2] R. Bansal, T. Bhatti, and D. Kothari, "Bibliography on the application of induction generators in nonconventional energy systems," *IEEE Transactions on Energy Conversion*, vol. 18, no. 3, pp. 433–439, 2003.

[3] L. I. Mazurenko, O. V. Dzhura, A. V. Kotsiuruba, and M. O. Shykhnenko, "A wind-hydro power system using a back-to-back pwm converter and parallel operated induction generators," in *2020 IEEE Problems of Automated Electrodrive. Theory and Practice (PAEP)*, pp. 1–5, 2020.

[4] P. K. Goel, B. Singh, S. S. Murthy, and N. Kishore, "Autonomous hybrid system using scig for hydro power generation and variable speed pmsg for wind power generation," in *2009 International Conference on Power Electronics and Drive Systems (PEDS)*, pp. 55–60, 2009.

[5] Y. Shurub and A. Dudnyk, "Realization techniques of statistical optimization modes of induction drives," in *2017 International Conference on Modern Electrical and Energy Systems (MEES)*, pp. 68–71, 2017.

[6] V. Yaramasu, B. Wu, P. C. Sen, S. Kouro, and M. Narimani, "High-power wind energy conversion systems: State-of-the-art and emerging technologies," *Proceedings of the IEEE*, vol. 103, no. 5, pp. 740–788, 2015.

[7] R. Nair and G. Narayanan, "Emulation of wind turbine system using vector controlled induction motor drive," *IEEE Transactions on Industry Applications*, vol. 56, no. 4, pp. 4124–4133, 2020.

[8] H. Yu, L. Li, J. Jin, and S. Feng, "Indirect power control of doubly-fed induction generator," in *2021 IEEE 5th Conference on Energy Internet and Energy System Integration (EI2)*, pp. 2775–2780, 2021.

[9] Y. Liu, G. Tao, H. Wang, and F. Blaabjerg, "Analysis of indirect rotor field oriented control-based induction machine performance under inaccurate

field-oriented condition," in *IECON 2017 - 43rd Annual Conference of the IEEE Industrial Electronics Society*, pp. 1810–1815, 2017.

[10] A. Zhang, X. Wang, W. Jia, and Y. Ma, "Indirect stator-quantities control for the brushless doubly fed induction machine," *IEEE Transactions on Power Electronics*, vol. 29, no. 3, pp. 1392–1401, 2014.

[11] L. Qiang-wen, Q.-f. Teng, Y.-s. Wang, and X.-p. Ma, "Application of high-order sliding mode variable structure control b ased on power- function in doubly fed induction generator," in *2018 IEEE International Conference of Intelligent Robotic and Control Engineering (IRCE)*, pp. 144–148, 2018.

[12] C. Bo, Z. Wei, and H. Wei, "Frequency domain analysis method of forced power oscillation induced by doubly-fed induction generator," in *2018 2nd IEEE Conference on Energy Internet and Energy System Integration (EI2)*, pp. 1–6, 2018.

[13] N. Bouchiba, S. Sallem, and M. B. A. Kammoun, "Three-phase self-excited induction generator analysis in stand-alone mode," in *IREC2015 The Sixth International Renewable Energy Congress*, pp. 1–6, 2015.

[14] R. S. R. Chilipi, B. Singh, and S. S. Murthy, "A 3-leg vsc based integrated voltage and frequency controller for a self excited induction generator employing water pumping," in *2010 5th International Conference on Industrial and Information Systems*, pp. 580–585, 2010.

[15] A. A. Al-Manfi, W. A. Mohamed, and E. F. Elsalhin, "Voltage control of stand-alone single phase self excited induction generator for variable speed wind turbine using bang bang-pwm controller," in *2022 IEEE 2nd International Maghreb Meeting of the Conference on Sciences and Techniques of Automatic Control and Computer Engineering (MI-STA)*, pp. 749–754, 2022.

[16] L. Wang and C.-H. Lee, "A novel analysis on the performance of an isolated self-excited induction generator," *IEEE Transactions on Energy Conversion*, vol. 12, no. 2, pp. 109–117, 1997.

[17] E. Marra and J. Pomilio, "Self-excited induction generator controlled by a vs-pwm bidirectional converter for rural applications," *IEEE Transactions on Industry Applications*, vol. 35, no. 4, pp. 877–883, 1999.

[18] S. Sombir and M. Singh, "Voltage and frequency control of self excited induction generator integrated with pv system," in *IECON 2020 The 46th Annual Conference of the IEEE Industrial Electronics Society*, pp. 4306–4311, 2020.

[19] A. B. Kasprowicz and K. Tomczuk, "Voltage and frequency stabilization system with self-excited induction generator," in *2015 9th International Conference on Compatibility and Power Electronics (CPE)*, pp. 467–472, 2015.

[20] T. Burton, D. Sharpe, N. Jenkins, and E. Bossanyi, *Wind Energy Handbook*. John Wiley & Sons, 2001.

[21] J. Fortmann, *Modeling of Wind Turbines with Doubly Fed Generator System*. 01 2015.

[22] S. K. Pillai and K. M. Desai, "A static scherbius drive with chopper," *IEEE Transactions on Industrial Electronics and Control Instrumentation*, vol. IECI-24, no. 1, pp. 24–29, 1977.

[23] Z. Zabar and A. Alexandrovitz, "Guidelines on adaptation of thyristorized switch for dc motor speed control," *IEEE Transactions on Industrial Electronics and Control Instrumentation*, vol. IECI-17, no. 1, pp. 10–13, 1970.

[24] G. A. Smith, "A current-source inverter in the secondary circuit of a wound rotor induction motor provides sub- and supersynchronous operation," *IEEE Transactions on Industry Applications*, vol. IA-17, no. 4, pp. 399–406, 1981.

[25] G. A. Smith and K. A. Nigim, "Wind-energy recovery by a static scherbius induction generator," *IEE Proceedings C (Generation, Transmission and Distribution)*, vol. 128, pp. 317–324(7), November 1981.

[26] C.-T. Ma and Z.-H. Shi, "A distributed control scheme using sic-based low voltage ride-through compensator for wind turbine generators," *Micromachines*, vol. 13, no. 1, 2022.

[27] H. A. Hussain, "Optimal gearbox ratio to minimize the power converter ratings in dfig-based type-3 wind turbines," *IEEE Access*, vol. 11, pp. 52158–52167, 2023.

[28] W. L. Erdman and J. Keller, "The doe next-generation drivetrain for wind turbine applications: Gearbox, generator, and advanced si/sic hybrid inverter system," in *2016 IEEE Energy Conversion Congress and Exposition (ECCE)*, pp. 1–8, 2016.

[29] H. Zhang and L. M. Tolbert, "Efficiency impact of silicon carbide power electronics for modern wind turbine full scale frequency converter," *IEEE Transactions on Industrial Electronics*, vol. 58, no. 1, pp. 21–28, 2011.

[30] J. He, T. Zhao, X. Jing, and N. A. Demerdash, "Application of wide bandgap devices in renewable energy systems - benefits and challenges," in *2014 International Conference on Renewable Energy Research and Application (ICRERA)*, pp. 749–754, 2014.

[31] L. Garcia-Rodriguez, V. Jones, J. Balda, E. Lindstrom, A. Oliva, and J. Gonzalez-Llorente, "Design of a gan-based microinverter for photovoltaic systems," in *2014 IEEE 5th International Symposium on Power Electronics for Distributed Generation Systems (PEDG)*, pp. 1–6, 2014.

[32] V. Yaramasu, A. Dekka, M. J. Durán, S. Kouro, and B. Wu, "Pmsg-based wind energy conversion systems: survey on power converters and controls," *IET Electric Power Applications*, vol. 11, no. 6, pp. 956–968, 2017.

[33] C. Klumpner and F. Blaabjerg, "Using reverse-blocking igbts in power converters for adjustable-speed drives," *IEEE Transactions on Industry Applications*, vol. 42, no. 3, pp. 807–816, 2006.

[34] M. Takei, Y. Harada, and K. Ueno, "600 v-igbt with reverse blocking capability," in *Proceedings of the 13th International Symposium on Power Semiconductor Devices & ICs. IPSD '01 (IEEE Cat. No.01CH37216)*, pp. 413–416, 2001.

[35] Y. Xu, Z. Wang, P. Liu, Q. Song, C. Tang, and M. Cheng, "Zero-voltage-switching current-source-inverter motor drives based on silicon carbide devices," in *2019 22nd International Conference on Electrical Machines and Systems (ICEMS)*, pp. 1–5, 2019.

[36] H. Barth and W. Hofmann, "Potentials and boundaries of discrete sic-transistors in ac drives," in *2018 20th European Conference on Power Electronics and Applications (EPE'18 ECCE Europe)*, pp. P.1–P.8, 2018.

[37] L. J. Villagrán-Valencia, J. Ramírez-Hernández, N. Mondragón-Escamilla, and I. Araujo-Vargas, "Analysis of bidirectional switching of sic transistors in a matrix converter leg," in *2018 IEEE International Conference on Electrical Systems for Aircraft, Railway, Ship Propulsion and Road Vehicles & International Transportation Electrification Conference (ESARS-ITEC)*, pp. 1–5, 2018.

[38] B. Sahan, S. V. Araújo, C. Nöding, and P. Zacharias, "Comparative evaluation of three-phase current source inverters for grid interfacing of distributed and renewable energy systems," *IEEE Transactions on Power Electronics*, vol. 26, no. 8, pp. 2304–2318, 2011.

[39] R. Ryndzionek and Ł. Sienkiewicz, "Evolution of the hvdc link connecting offshore wind farms to onshore power systems," *Energies*, vol. 13, p. 1914, 04 2020.

[40] R. M. Prasad and M. A. Mulla, "A novel position-sensorless algorithm for field-oriented control of dfig with reduced current sensors," *IEEE Transactions on Sustainable Energy*, vol. 10, no. 3, pp. 1098–1108, 2019.

[41] F. Fuchs and A. Kloenne, "Dc link and dynamic performance features of pwm igbt current source converter induction machine drives with respect to industrial requirements," in *The 4th International Power Electronics and Motion Control Conference, 2004. IPEMC 2004.*, vol. 3, pp. 1393–1398 Vol.3, 2004.

[42] P. E. Kakosimos, A. G. Sarigiannidis, M. E. Beniakar, A. G. Kladas, and C. Gerada, "Induction motors versus permanent-magnet actuators for aerospace applications," *IEEE Transactions on Industrial Electronics*, vol. 61, no. 8, pp. 4315–4325, 2014.

[43] E. Aydin, A. Polat, and L. T. Ergene, "Vector control of dfig in wind power applications," in *2016 IEEE International Conference on Renewable Energy Research and Applications (ICRERA)*, pp. 478–483, 2016.

[44] Y. Ihedrane, C. El Bekkali, and B. Bossoufi, "Direct and indirect field oriented control of dfig-generators for wind turbines variable-speed," in *2017 14th International Multi-Conference on Systems, Signals & Devices (SSD)*, pp. 27–32, 2017.

[45] I. Erazo-Damián, J. M. Apsley, R. Perini, M. F. Iacchetti, and G. D. Marques, "Stand-alone dfig foc sensitivity and stability under mismatched inductances," *IEEE Transactions on Energy Conversion*, vol. 34, no. 2, pp. 860–869, 2019.

[46] W. Koczara, J. Przybylski, and H. Drechsler, "Oriented control in the drive system double-fed machine (dfm)," *IFAC Proceedings Volumes*, vol. 20, no. 5, Part 3, pp. 381–385, 1987. 10th Triennial IFAC Congress on Automatic Control - 1987 Volume III, Munich, Germany, 27-31 July.

[47] N. Miller, J. Sanchez-Gasca, W. Price, and R. Delmerico, "Dynamic modeling of ge 1.5 and 3.6 mw wind turbine-generators for stability simulations," in *2003 IEEE Power Engineering Society General Meeting (IEEE Cat. No.03CH37491)*, vol. 3, pp. 1977–1983 Vol. 3, 2003.

[48] H. Benbouhenni and Z. Boudjema, "Two-level dtc based on ann controller of dfig using 7-level hysteresis command to reduce flux ripple comparing with traditional command," in *2018 International Conference on Applied Smart Systems (ICASS)*, pp. 1–8, 2018.

[49] Y. Bakou, M. Abid, A. Harrouz, I. Yaichi, I. Colak, K. Kayisli, and A. Aissaoui, "Dtc control of the dfig, application to the production of electrical energy," in *2019 8th International Conference on Renewable Energy Research and Applications (ICRERA)*, pp. 910–915, 2019.

[50] Y. Li, L. Hang, G. Li, Y. Guo, Y. Zou, J. Chen, J. Li, J. Zhuang, and S. Li, "An improved dtc controller for dfig-based wind generation system," in *2016 IEEE 8th International Power Electronics and Motion Control Conference (IPEMC-ECCE Asia)*, pp. 1423–1426, 2016.

[51] K. Ouezgan, B. Bossoufi, and M. N. Bargach, "Dtc control of dfig-generators for wind turbines: Fpga implementation based," in *2017 International Renewable and Sustainable Energy Conference (IRSEC)*, pp. 1–6, 2017.

[52] P. Singh and A. Kaur, "Power control of doubly fed induction generator (dfig) using back to back converters (pwm technique)," in *2014 IEEE International Conference on Advanced Communications, Control and Computing Technologies*, pp. 73–77, 2014.

[53] S. Demirbas and S. Bayhan, "Active and reactive power control of doubly fed induction generator using direct power control technique," in *4th International Conference on Power Engineering, Energy and Electrical Drives*, pp. 41–45, 2013.

[54] B. S. Soares Pereira and T. Luis Maia Santos, "Speed and reactive power regulation of doubly-fed induction generator using model predictive control," in *2018 Workshop on Communication Networks and Power Systems (WCNPS)*, pp. 1–4, 2018.

[55] J. B. Alaya, A. Khedher, and M. F. Mimouni, "Nonlinear vector control strategy applied to a variable speed dfig generation system," in *Eighth International Multi-Conference on Systems, Signals & Devices*, pp. 1–8, 2011.

[56] M. N. Mestri and B. S. Kumar, "Design of 9-switch converter for dfig system for active and reactive power control by pid and fuzzy logic controller," in *2019 3rd International conference on Electronics, Communication and Aerospace Technology (ICECA)*, pp. 763–767, 2019.

[57] A. Ramadan, S. Kamel, A. Rashad, and J. Yu, "Design of fuzzy logic control for direct and quadratic components of dfig's rotor and grid side control system based wind turbines," in *2018 Twentieth International Middle East Power Systems Conference (MEPCON)*, pp. 655–659, 2018.

[58] A. Geniusz and Z. Krzemiński, "Control system based on the modified multiscalar model for the double fed machine," 2005.

[59] E. Bogalecka, "Power control of a double fed induction generator without speed or position sensor," in *1993 Fifth European Conference on Power Electronics and Applications*, pp. 224–228 vol.8, 1993.

[60] Z. Krzeminski, "Sensorless multiscalar control of double fed machine for wind power generators," in *Proceedings of the Power Conversion Conference-Osaka 2002 (Cat. No.02TH8579)*, vol. 1, pp. 334–339 vol.1, 2002.

[61] E. Bogalecka and Z. Krzeminski, "Control systems of doubly-fed induction machine supplied by current controlled voltage source inverter," in *1993 Sixth International Conference on Electrical Machines and Drives (Conf. Publ. No. 376)*, pp. 168–172, 1993.

[62] G. Iwanski and W. Koczara, "Sensorless direct voltage control method for stand-alone slip-ring induction generator," in *2005 European Conference on Power Electronics and Applications*, pp. 10 pp.–P.10, 2005.

[63] G. Iwanski and W. Koczara, "Positive and negative sequence based sensorless control for stand-alone slip-ring generator," in *2006 12th International Power Electronics and Motion Control Conference*, pp. 555–560, 2006.

[64] G. Iwanski and W. Koczara, "Dfig-based power generation system with ups function for variable-speed applications," *IEEE Transactions on Industrial Electronics*, vol. 55, no. 8, pp. 3047–3054, 2008.

[65] A. Popenda, "The dfm control system based on pll," *Communications - Scientific Letters of the University of Zilina*, vol. 11, no. 1, pp. 55–59, 2009.

[66] A. Popenda, "Analysis of influence of input quantities and disturbances on generator operation of doubly fed machine," *Prace Instytutu Elektrotechniki*, 2011.

[67] E. Bogalecka, "Stability analysis of a double fed induction generator with the pll controller," in *Proceedings of IECON'94 - 20th Annual Conference of IEEE Industrial Electronics*, vol. 1, pp. 67–72 vol.1, 1994.

[68] Z. M. Hailemariam, R. Leidhold, and G. T. Tesfamariam, "Real-time speed control of a pmsm for wind turbine application," in *2019 IEEE PES/IAS PowerAfrica*, pp. 396–401, 2019.

[69] Y. Gang, G. Yichang, Z. Lidan, L. Dongdong, and L. Xing, "Multi-phase permanent magnet synchronous generator variable speed constant frequency offshore wind system based on modular multilevel converter," in *2019 IEEE Innovative Smart Grid Technologies - Asia (ISGT Asia)*, pp. 2127–2132, 2019.

[70] N. Djagarov, Z. Grozdev, G. Enchev, and J. Djagarova, "Study of low-voltage ride through of wind permanent magnet synchronous generator by means of statcom," in *2019 20th International Scientific Conference on Electric Power Engineering (EPE)*, pp. 1–6, 2019.

[71] O. Solomon, "The design, control and dynamic performance of an interior permanent magnet synchronous generator for wind power system," in *IECON 2018 - 44th Annual Conference of the IEEE Industrial Electronics Society*, pp. 714–718, 2018.

[72] J. Ma, D. Zhao, L. Yao, M. Qian, K. Yamashita, and L. Zhu, "Analysis on application of a current-source based dfig wind generator model," *CSEE Journal of Power and Energy Systems*, vol. 4, no. 3, pp. 352–361, 2018.

[73] K. Blecharz and M. Morawiec, "Nonlinear control of a doubly fed generator supplied by a current source inverter," *Energies*, vol. 12, no. 12, 2019.

[74] P. Kroplewski, M. Morawiec, A. Jąderko, and C. Odeh, "Simulation studies of control systems for doubly fed induction generator supplied by the current source converter," *Energies*, vol. 14, no. 5, 2021.

[75] M. Morawiec, P. Kroplewski, and F. Wilczyński, "Feedback control of doubly-fed generator connected to current source converter," *IEEE TRANSACTIONS ON INDUSTRIAL ELECTRONICS*, pp. 1–12, 2023.

[76] R. Krishan and J. Choudhary, "Current source converter-based optimal power extraction and power control of a doubly fed induction generator (dfig) using backstepping control.," *Engineering Research Express*, vol. 6, 12 2023.

[77] Z. Krzemiński, "Control systems of doubly fed induction machine based on multiscalar model," *IFAC Proceedings Volumes*, vol. 23, no. 8, Part 4, pp. 521–526, 1990. 11th IFAC World Congress on Automatic Control, Tallinn, 1990 - Volume 4, Tallinn, Finland.

[78] M. Morawiec, "The control system of double fed machine supplied by current source converter," *Przeglad Elektrotechniczny*, vol. 85, pp. 61–65, 01 2009.

[79] Y.-M. Saint-Drenan, R. Besseau, M. Jansen, I. Staffell, A. Troccoli, L. Dubus, J. Schmidt, K. Gruber, S. G. Simões, and S. Heier, "A parametric model for wind turbine power curves incorporating environmental conditions," *Renewable Energy*, vol. 157, pp. 754–768, 2020.

[80] L. Hansen, L. Helle, F. Blaabjerg, E. Ritchie, S. Munk-Nielsen, H. Bindner, P. Sorensen, and B. Bak-Jensen, "Conceptual survey of generators and power electronics for wind turbines," 01 2001.

[81] Z. Krzemiński, *Cyfrowe sterowanie maszynami asynchronicznymi*. Postępy Napędu Elektrycznego i Energoelektroniki, Wydaw. Politechniki Gdańskiej, 2001.

[82] P. Kovács, *Transient Phenomena in Electrical Machines*. Developments in Food Science, Elsevier, 1984.

[83] K. Ogata, *Modern Control Engineering*. Arco Military Book, Prentice-Hall, 1970.

[84] G. F. Franklin, J. D. Powell, and A. Emami-Naeini, *Feedback Control of Dynamic Systems*. USA: Prentice Hall Press, 7th ed., 2014.

[85] N. S. Nise, *Control Systems Engineering*. USA: John Wiley & Sons, Inc., 3rd ed., 2000.

[86] F. Golnaraghi and B. Kuo, *Automatic Control Systems*. Wiley, 2009.

[87] K. J. Astrom and R. M. Murray, *Feedback Systems: An Introduction for Scientists and Engineers*. USA: Princeton University Press, 2008.

[88] C. L. Phillips and H. T. Nagle, *Digital control system analysis and design (3rd ed.)*. USA: Prentice-Hall, Inc., 1995.

[89] B. Friedland, *Control System Design: An Introduction to State-Space Methods*. Dover Books on Electrical Engineering, Dover Publications, 2012.

[90] H. Górecki, *Analiza i synteza układów regulacji z opóźnieniem*. Poland: Wydawnictwa Naukowo-Techniczne, 1971.

[91] K. Zhou, J. C. Doyle, and K. Glover, *Robust and optimal control*. USA: Prentice-Hall, Inc., 1996.

[92] A. H. Abobkr and M. E. El-Hawary, "Fault ride-through capability of doubly-fed induction generators based wind turbines," in *2015 IEEE Electrical Power and Energy Conference (EPEC)*, pp. 8–15, 2015.

[93] L. Zhang, X. Jin, and L. Zhan, "Reactive power control of doubly fed induction generator during grid voltage dips," in *2012 Asia-Pacific Power and Energy Engineering Conference*, pp. 1–5, 2012.

[94] A. Dittrich and A. Stoev, "Comparison of fault ride-through strategies for wind turbines with dfim generators," in *2005 European Conference on Power Electronics and Applications*, pp. 8 pp.–P.8, 2005.

[95] "Ieee recommended practice for monitoring electric power quality," *IEEE Std 1159-2019 (Revision of IEEE Std 1159-2009)*, pp. 1–98, 2019.

List of figures

List of tables

Appendix A

Machine and converter parameters

Table A.1: DFIG with Current Source Converter System parameters and reference unit.

Symbol	**Name**	**Values**
R_s	stator resistance	2.741 Ω/0.0649 p.u.
R_r	rotor resistance	3.212 Ω/0.0762 p.u.
L_m	magnetizing inductance	0.17 H/1.2733 p.u.
L_s, L_r	stator and rotor inductance	0.195 H/1.3378 p.u.
P_n	nominal power	2 kW
I_{ns}	nominal stator current	5.5 A
I_{nr}	nominal rotor current	3.4 A
U_n	nominal stator voltage	400 V
n	nominal rotor speed	910 rpm
f	nominal frequency	50 Hz
r	turn ratio N_s/N_r	1
L_d	DC choke inductance	12.4 mH/0.1 p.u.
C_m	output filter capacitance	100 µF/0.125 p.u.
U_b	reference voltage	400 V
$I_b = \sqrt{3}I_{ns}$	reference current	9.52 A
S_b	reference power	3.81 kVA
T_{imp}	converters PWM period	150 ms

Table A.2: Values of inner and outer control loops gains for tested control methods used in simulation tests

Name	**Symbol**	**Value**
Field Oriented Control		
proportional gain of i_{rd}^*	k_{p1}	0.4
integral gain of i_{rd}^*	k_{i1}	0.25
proportional gain of i_{rq}^*	k_{p2}	0.4
integral gain of i_{rq}^*	k_{i2}	0.25
Multiscalar structure 1		
proportional gain of s_P	k_{pP}	1.05
integral gain of s_P	k_{iP}	0.05
proportional gain of s_Q	k_{pQ}	1.5
integral gain of s_Q	k_{iQ}	0.07
Multiscalar structure 2		
proportional gain of s_P	k_{pP}	1.75
integral gain of s_P	k_{iP}	0.02
proportional gain of s_Q	k_{pQ}	1.75
integral gain of s_Q	k_{iQ}	0.015
Multiscalar structure 3		
proportional gain of s_P	k_{pP}	2
integral gain of s_P	k_{iP}	0.1
proportional gain of s_Q	k_{pQ}	4
integral gain of s_Q	k_{iQ}	0.2
proportional gain of z_{12}	k_{p12}	3
integral gain of z_{12}	k_{i12}	0.5
proportional gain of z_{22}	k_{p22}	3
integral gain of z_{12}	k_{i22}	0.1
Multiscalar structure 4		
proportional gain of s_P	k_{pP}	2
integral gain of s_P	k_{iP}	0.1
proportional gain of s_Q	k_{pQ}	4
integral gain of s_Q	k_{iQ}	0.2
proportional gain of z_{12}	k_{p12}	3
integral gain of z_{12}	k_{i12}	0.5
proportional gain of z_{22}	k_{p22}	3
integral gain of z_{12}	k_{i22}	0.1

Table A.3: Values of inner and outer control loops gains for tested control methods used in experimental tests

Name	Symbol	Value
Field Oriented Control		
proportional gain of i^*_{rd}	k_{p1}	0.35
integral gain of i^*_{rd}	k_{i1}	0.0045
proportional gain of i^*_{rq}	k_{p2}	0.3
integral gain of i^*_{rq}	k_{i2}	0.008
Multiscalar structure 1		
proportional gain of s_P	k_{pP}	1.75
integral gain of s_P	k_{iP}	0.025
proportional gain of s_Q	k_{pQ}	1.0
integral gain of s_Q	k_{iQ}	0.00975
Multiscalar structure 3		
proportional gain of s_P	k_{pP}	1.0
integral gain of s_P	k_{iP}	0.0175
proportional gain of s_Q	k_{pQ}	1.25
integral gain of s_Q	k_{iQ}	0.0075
proportional gain of z_{12}	k_{p12}	1
integral gain of z_{12}	k_{i12}	0.0125
proportional gain of z_{22}	k_{p22}	0.9
integral gain of z_{12}	k_{i22}	0.0125
Multiscalar structure 4		
proportional gain of s_P	k_{pP}	1.0
integral gain of s_P	k_{iP}	0.0175
proportional gain of s_Q	k_{pQ}	1.25
integral gain of s_Q	k_{iQ}	0.0075
proportional gain of z_{12}	k_{p12}	1
integral gain of z_{12}	k_{i12}	0.0125
proportional gain of z_{22}	k_{p22}	0.9
integral gain of z_{12}	k_{i22}	0.0125
DC current PI		
proportional gain of s_P	k_{pP}	0.3
integral gain of s_P	k_{iP}	0.055

Appendix B

Experimental stand

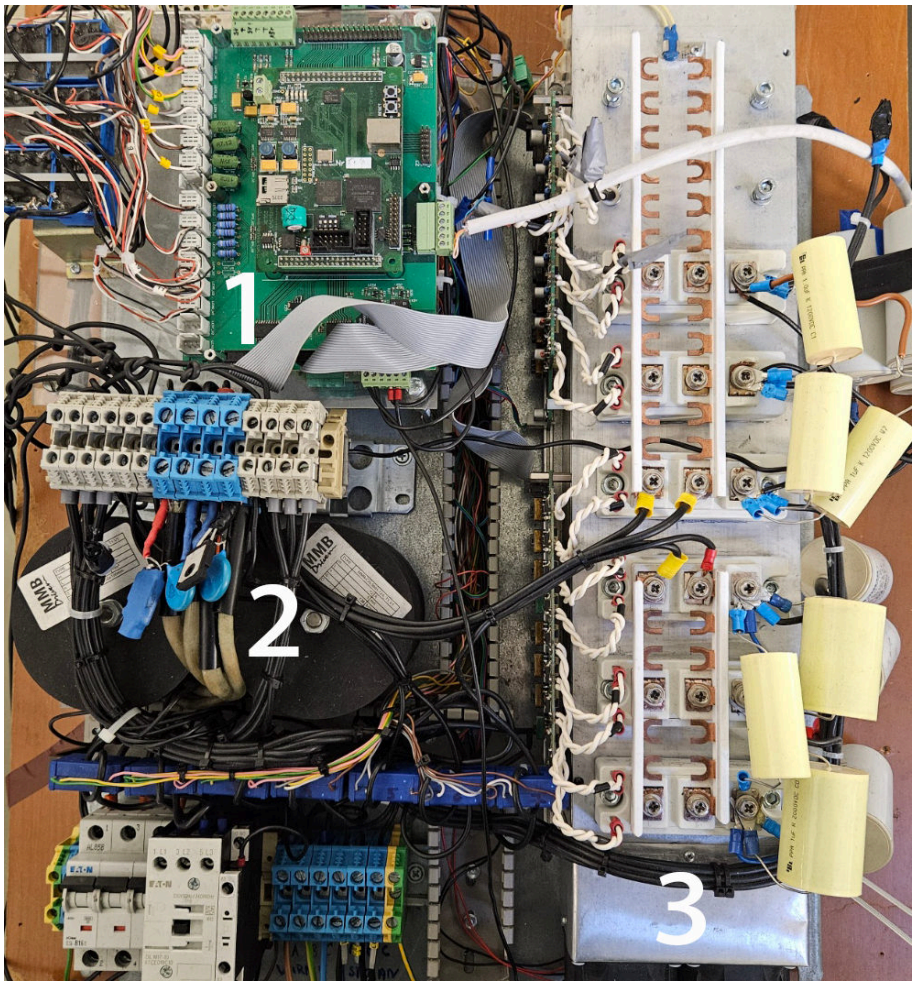

Figure B.1: Illustration of the Current Source Converter including signal processing unit (1), DC-link (2) and transistor array (3)

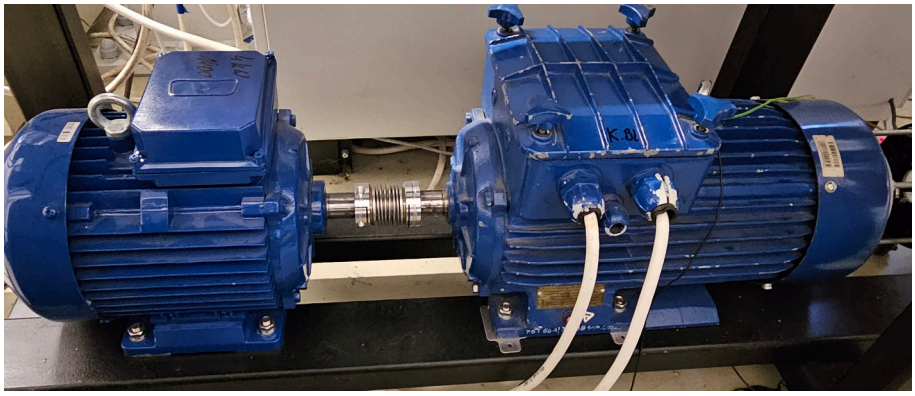

Figure B.2: Illustration of the generator system – three-phase induction motor working as a load on the left and Doubly-Fed Induction Machine on the right